May 2018

Design of a High Frequency Four Port Transformer for DC/DC Converters

Md Abdul Gaffar
University of Wisconsin-Milwaukee

DESIGN OF A HIGH FREQUENCY FOUR PORT TRANSFORMER FOR DC/DC CONVERTERS

by

Md Abdul Gaffar

A Thesis Submitted in

Partial Fulfillment of the

Requirements for the Degree of

Master of Science

in Engineering

at

The University of Wisconsin-Milwaukee
May 2018

ABSTRACT

DESIGN OF A HIGH FREQUENCY FOUR PORT TRANSFORMER FOR DC/DC CONVERTERS

by

Md Abdul Gaffar

The University of Wisconsin-Milwaukee, 2018
Under the Supervision of Professor Adel Nasiri

Large scale integration of renewable energy systems (RES) and energy storage systems (ESS) demands a better connectivity between distributed sources and loads. Multi-port solid state transformer (MPSST) plays a critical role as a joint node to integrate RESs, ESSs, utility grid, and loads. MPSST offers several advantages including independent power flow control on each port, voltage or current regulations, compactness and portability, and galvanic isolation.

This thesis seeks to address some of the remaining challenges of using MPSST. Operation of the converter in closed-loop with phase shift modulation is analyzed for a dual active bridge as the control building block and a four-port DC/DC converter as the MPSST in Ansys Simplorer. The high frequency transformer part was designed and modeled in Ansys Maxwell. The model is validated with FEA simulation and various metrics like flux density (B), current density (J), magnetic field intensity (H), core loss, winding loss were investigated for different operating conditions to evaluate the transformer performance.

A co-simulation between the magnetic environment in Ansys Maxwell, and power electronics and control part in Ansys Simplorer, has been carried out to benefit from the utilization of the developed realistic high frequency transformer for the operation of the MPSST.

TABLE OF CONTENTS

LIST OF FIGURES

ACKNOWLEDGEMENTS

I would like to express my sincere gratitude to my advisor Professor Adel Nasiri for his valuable guidance, motivation, support and advice. I would like to extend my thanks to Professor Hossein Hosseini and Professor David Yu for their suggestion to my work. I would like to thank Dr. Mehdy Khayamy for sharing his valuable insights and suggestions throughout the work. I would also like to thank all the team members from my lab for sharing their in-depth knowledge with me. Last but not the least, I would like to thank my family members for their continuous support and encouragement.

Chapter 1: Introduction

1.1 Background and prior works

Energy security is one of the burning global issue for any country nowadays. Fossil fuel like coal, gas and petroleum are fulfilling major portion of energy demand. Growing demand for fossil fuel is polluting environment which is responsible for climate change. It is important to look for alternative energy resources to reduce dependence on fossil fuel. To mitigate environmental pollution and reduce dependency on fossil fuel, penetration of renewable energy as an energy source is increased to generate electricity.

Renewable energy supply electricity to the power grid during peak demand. Households and small business also install renewable energy like wind and solar to meet electricity demand, excess electricity is supplied to the grid after meeting their demand. As the availability of solar and wind is uncertain, integration of energy storages like battery is also included in a grid with renewable energy resources. Moreover, renewable energy should be supplied to the electric grid instantaneously that is why energy storage batteries are included in grid to capture excess electricity generated by renewables. Energy storage is supplying power to grid when energy is in great demand.

Electric vehicles are also a good option as environmental friendly vehicle than its mechanical counterpart. Electric vehicles can play a vital role to serve the energy demand while discharging batteries. Batteries are also used to store energy in different types of appliances, airplanes, ships, medical devices.

Renewable energy should be regulated before supplying to the grid because of their slow response time and uncertainty of constant power supply. Renewable energy is connected to the grid with DC bus and power transfer can be controlled with DC-DC converter. Wind power can be converted in DC, then after conditioning it can be send to AC electrical grid.

When we integrate renewables, there will be more conversion steps which will increase the number of converter in the system. The efficiency of the system will be reduced as well as cost will increase. This issue could be resolved by introducing multiport DC-DC converter. Renewable energy sources and energy storage could be connected to multiport converter. DC-DC converter might be bi-directional in nature that is why energy storage and electric vehicles are very easy to implement in grid.

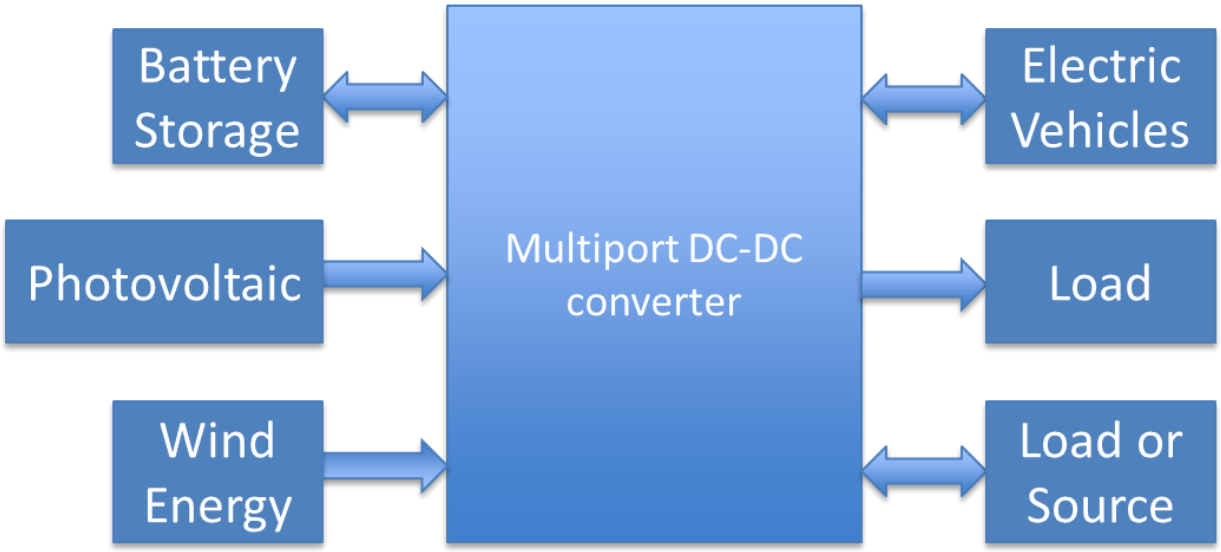

Figure 1.1 . Different type of sources integrated in DC-DC converter.

Dual active bridge and four port DC-DC converter are very useful for integrating renewable energy as they have higher efficiency, easy control and galvanic isolation with high frequency transformer. The power can be transferred using simple phase shift control.

Isolation transformer takes large volume in a converter. Because of high frequency, the transformer size could be reduced in considerable amount. Power density also increases because of size reduction that is achieved because of high frequency. Galvanic isolation is used to protect the circuit from different fault condition. Losses increase in high frequency transformer, specially winding loss due to skin effect and proximity effect.

Optimized high power and high density transformer was built in [1]. Core loss, winding loss, current density and thermal modelling was optimized to get parameters for building high frequency transformer. Various core was investigated and optimized flux density was calculated to have suitable VA rating for each core

Several materials like Vitroperm500F and 3C85 performances was investigated for offshore wind farm application which are suitable for high frequency application [2]. It was found Vitroperm500F shows high power density than 3C85. Also, greater efficiency in higher frequency could be achieved after optimizing transformer parameters. Transformer parameter was optimized for different materials and frequency in DC-DC application and was found that efficiency could reach up to 99.7% [3].

Most of the grid tie DC-DC application require galvanic isolation. Isolation transformer was built in [4]. Pareto front was used to have optimized design of transformer evaluating power density and efficiency.

Though ferrite core is suitable for high frequency application, silicon steel could be utilized in medium frequency application [5]. While developing core loss model using square wave, ripple was also considered.

1.2 Objective

To investigate close loop performance of dual active bridge converter and four port DC-DC converter by using phase shift modulation for power transfer between different converter ports.

To build a high frequency four port isolation transformer for DC-DC converter and study efficient operation in different operating condition.

1.3 Thesis outline

This thesis is organized according to the chapters as follows:

Chapter 2 discussed dual active bridge converter, analyzed its operation. Phase shift modulation and power transfer between two ports was also presented. Close loop control using phase shift modulation and controller performance was also analyzed.

Chapter 3 presented four port DC-DC converter operation and close loop control performance. Also, derived flux, voltage and leakage inductances for four port transformer used as isolation transformer in four port DC-DC converter.

Chapter 4 analyzed design of four port high frequency transformer by using FEA simulation. In this chapter, loss performance of core and winding was also discussed. Flux density, current density was also presented for different operating condition.

Chapter five concludes the thesis.

Chapter 2: Dual active bridge converter modelling and control of power flow

2.1 Dual active bridge converter operation

Dual active bridge converter (DABC) have two full bridge converters across a high frequency transformer. For accurate power transfer, AC voltage should be provided by the converter in both ends of the high frequency transformer. To analyze DABC all losses will be neglected. Magnetizing inductance of the high frequency transformer will also be neglected.

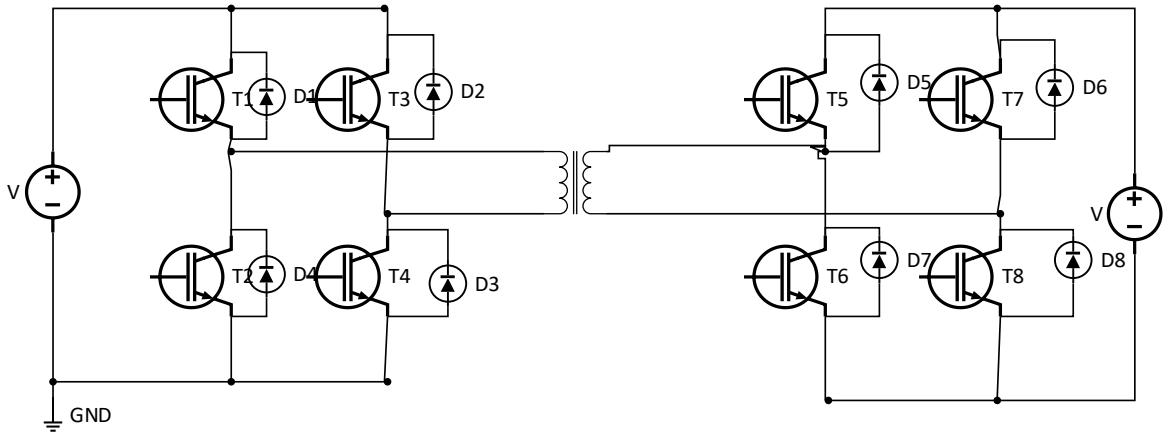

Figure 2.1. Dual active bridge converter

Switching sequence of left side is T1T4, T2T3 and right side is T5T8, T6T7. Different methods can be used to generate gate pulses to operate switches of converter.

2.1.1 DABC analysis of inductor current and power for same voltage during phase shift modulation

DABC can be expressed as below equivalent circuit

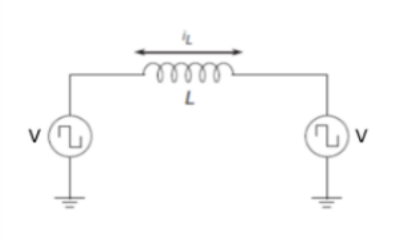

Figure 2.2. Equivalent circuit of DABC for same voltage [6].

We know the expression for inductor current is

$$i_L(t) = \int_0^t \frac{V}{L} dt$$

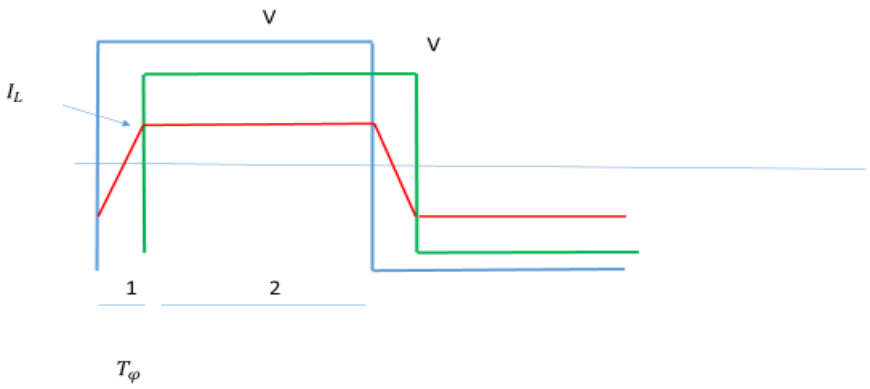

Figure 2.3. Transformer voltage and inductor current waveform for same voltage.

Inductor current in different regions from figure.2 for same voltage of DABC,

Current, $I_1 = \frac{V}{L}\left(2t - \frac{\varphi T}{2\pi}\right)$

Current, $I_2 = \frac{V}{L}\frac{\varphi T}{2\pi}$

Current, $I_3 = \ -I_1$

Current, $I_4 = \ -I_2$

Power equation for same voltage across high frequency transformer we can get,

Region 1: $P_1 = \frac{1}{T}\int_0^{\frac{\varphi T}{2\pi}}\{V \times \frac{V}{L}(2t - \frac{\varphi T}{2\pi})\}dt$ = 0

Region 2:$P_2 = \frac{1}{T}\int_0^{\frac{T}{2}-\frac{\varphi T}{2\pi}} V \times \frac{V}{L}\frac{\varphi T}{2\pi}dt$ = $\frac{V^2}{L}\frac{\varphi T}{4\pi}(1 - \frac{\varphi}{\pi})$

Region 3: $P_3 = 0$

Region 4:$P_4 = \frac{1}{T}\int_0^{\frac{T}{2}-\frac{\varphi T}{2\pi}} V \times \frac{V}{L}\frac{\varphi T}{2\pi}dt$ = $\frac{V^2}{L}\frac{\varphi T}{4\pi}(1 - \frac{\varphi}{\pi})$

Total Power = $P_1 + P_2 + P_3 + P_4 = \boldsymbol{\frac{V^2}{L}\frac{\varphi T}{2\pi}(1 - \frac{\varphi}{\pi})}$

2.1.2 DABC analysis of inductor current and power for different voltage during phase shift modulation

DABC can be expressed as below equivalent circuit [7]

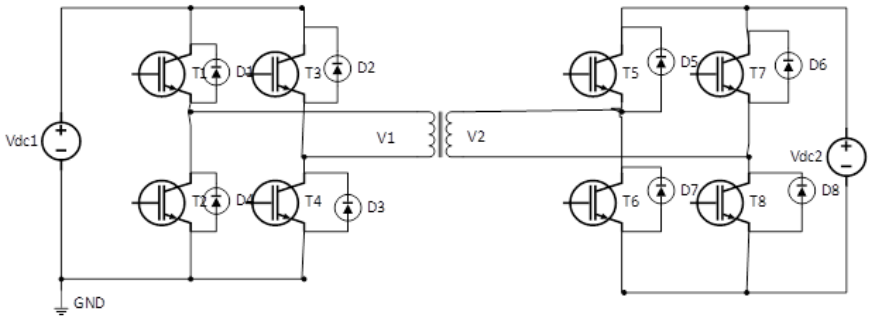

Figure 2.4. Dual active bridge converter (different voltage).

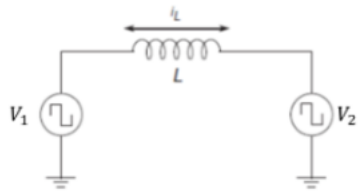

Figure 2.5. Equivalent circuit of DABC for different voltage [6].

We know the expression for inductor current is

$$i_L(t) = \int_0^t \frac{V}{L} dt$$

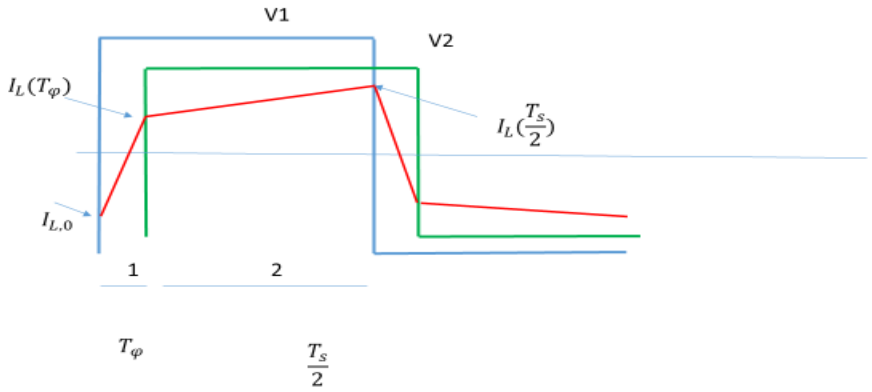

Figure 2.6. Transformer voltage and inductor current waveform for different voltage.

During steady-state operation, the voltages V1 and V2 and the inductor current repeat every half-cycle with reversed signs—

$$V_1(t+\frac{T_s}{2}) = -V_1(t)$$

$$V_2(t+\frac{T_s}{2}) = -V_2(t)$$

$$i_L(t+\tfrac{T_s}{2}) = -i_L(t)\text{-------(2.1)}$$

Here $T_\varphi = \frac{\varphi}{2\pi f_s}$

For positive phase shift,

Time interval 1: $i_L(t) = i_{L,0} + \frac{V_1+V_2}{L}t$ (from 0 to $\frac{\varphi}{2\pi f_s}$) -------(2.2)

Time interval 2: $i_L(t) = i_L(T_\varphi) + \frac{V_1-V_2}{L}(t-t_1$ (from $\frac{\varphi}{2\pi f_s}$ to $\frac{T_s}{2}$) -------(2.3)

Derivation of initial current---

From (2) ---- $i_L(t) = i_{L,0} + \frac{V_1+V_2}{L}t$

$$i_L(T_\varphi) = i_{L,0} + \frac{V_1+V_2}{L}T_\varphi$$

$$i_{L,0} = i_L(T_\varphi) - \frac{V_1+V_2}{L}T_\varphi$$

From (3) we can now write

$$i_L(t) = i_L(T_\varphi) + \frac{V_1-V_2}{L}(\frac{T_s}{2} - T_\varphi)$$

$$i_L\left(\frac{T_s}{2}\right) = i_L(T_\varphi) + \frac{V_1-V_2}{L}(\frac{T_s}{2} - T_\varphi)$$

From (1) we get when t=0, $i_L\left(\frac{T_s}{2}\right) = -i_{L,0}$,

$$-i_{L,0} = i_{L,0} + \frac{V_1+V_2}{L}T_\varphi + \frac{V_1-V_2}{L}(\frac{T_s}{2} - T_\varphi)$$

$$i_{L,0} = \frac{\pi(V_2-V_1)-2\varphi V_2}{4\pi f_s L} \quad \text{------- (2.4)}$$

First interval current and power

From (2) we know that-

$$i_L(t) = i_{L,0} + \frac{V_1+V_2}{L}t \ \text{ (from 0 to } \frac{\varphi}{2\pi f_s})$$

$$i_L(t) = \frac{\pi(V_2-V_1)-2\varphi V_2}{4\pi f_s L} + \frac{V_1+V_2}{L}t \ \text{ (from 0 to } \frac{\varphi}{2\pi f_s}) \ \text{------(2.5)}$$

For power, we know that-

$$P_{11} = \frac{1}{T}\int_0^{\frac{\varphi}{2\pi f_s}} V_1 \times i_L(t)\, dt$$

$$P_{11} = \frac{1}{T}\int_0^{\frac{\varphi}{2\pi f_s}} V_1 \times [\frac{\pi(V_2 - V_1) - 2\varphi V_2}{4\pi f_s L} + \frac{V_1 + V_2}{L} t\ ]\, dt$$

$$P_{11} = V_1[\frac{\pi(V_2 - V_1)\varphi + (V_1 - V_2)\varphi^2}{8\pi^2 f_s L}]$$---------(2.6)

Second interval current and power

From (3) we know that-----

$i_L(t) = i_L(T_\varphi) + \frac{V_1 - V_2}{L}(t - t_1)$ (from $\frac{\varphi}{2\pi f_s}$ to $\frac{T_s}{2}$)

$$i_L(t) = \frac{\pi(V_2 - V_1) - 2\varphi V_2}{4\pi f_s L} + \frac{V_1 + V_2}{L}\frac{\varphi}{2\pi f_s} + \frac{V_1 - V_2}{L}(t - \frac{\varphi}{2\pi f_s})$$ ----------(2.7)

For power, we know that

$$P_{12} = \frac{1}{T}\int_{\frac{\varphi}{2\pi f_s}}^{\frac{T_s}{2}} V_1 \times i_L(t)\, dP_{12}$$

$$= \frac{1}{T}\int_{\frac{\varphi}{2\pi f_s}}^{\frac{T_s}{2}} V_1 \times \frac{\pi(V_2 - V_1) - 2\varphi V_2}{4\pi f_s L} + \frac{V_1 + V_2}{L}\frac{\varphi}{2\pi f_s} + \frac{V_1 - V_2}{L}(t - \frac{\varphi}{2\pi f_s})\ dt$$

$$P_{12} = V_1[\frac{\varphi V_2}{8\pi f_s L} + \frac{\varphi V_1}{8\pi f_s L} - \frac{\varphi^2 V_2}{8\pi^2 f_s L} - \frac{\varphi^2 V_1}{8\pi^2 f_s L}]$$----------(2.8)

From (2.6) and (2.8) of 1 and 2 regions, we get that

P=$P_{11} + P_{12}$

$$P=\frac{V_1 V_2 \varphi(\pi-\varphi)}{4\pi^2 f_s L}$$

So total power for 1,2 3 4 regions is

$$P=\frac{V_1 V_2 \varphi(\pi-\varphi)}{2\pi^2 f_s L}$$

Positive signed power is transferred from left to right side of the transformer and negative signed power is transferred from right to left side of the transformer.

Maximum power is transferred when $\varphi = \pm\frac{\pi}{2}$ and can be expressed as-

$$P_{max}=\frac{V_1 V_2}{8 f_s L}$$

2.2 Phase shift control of DABC

To control the power flow between both side of DABC, phase shift control method was implemented. It will also ensure overcurrent issue for better heat distribution of isolation transformer. In this control, DABC will be operated on constant switching frequency and duty cycle will be 50%. By varying, phase shift it will ensure the flow of power in both end. Logical state machine can also be implemented to control bi-directional flow of power.

Power of primary side of the transformer is measured. Then average power P_{avg} for every switching period is calculated. Power regulator compares P_{avg} and P_{ref}

to generate phase shift angle φ [8]. A limiter can be used to maintain the phase shift angle within range.

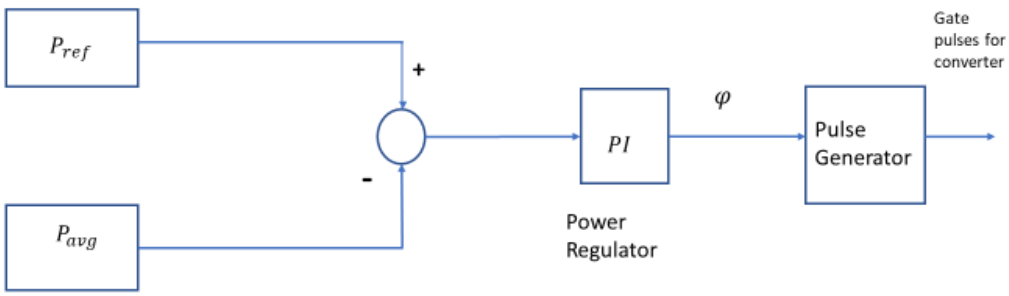

Figure 2.7. Control blocks for phase shift control of DABC.

The measured phase shift after power regulator generates gate pulses of the secondary side of DABC. Shifted gate pulses help to transfer power in both sides of the transformer. The output voltage of primary and secondary side has a shape of a square wave with 50% duty cycle that will be phase shifted in response to gate pulses.

2.2.1 Controller performance analysis:

Step response from 80 to 20 percent of average power was simulated to test the controller performance on both sides of the transformer Figure 2.8 . To observe the tracking of P_{avg} with P_{ref}, we transferred data to Matlab from Simplorer. We can observe that P_{avg} is tracking P_{ref} Figure 2.9. A ramp from 0-100 percent of rated average power was generated for P_{ref} to test the

functionality of the controller. Data was collected for full range of power which corresponds to 0—90-degree phase shift and was plotted against average power in close loop Figure 2.10. Parameters of this high frequency transformer are suitable for up to 50000 Hz. The DABC was rated for up to 8000-Watt Power transfer.

Step response to test power regulator when voltages are different at both ends of the transformer was also verified to observe the controller. It was tested from 70 to -70 percent to observe capability to transfer power bi-directional Figure 2.11, Figure 2.12.

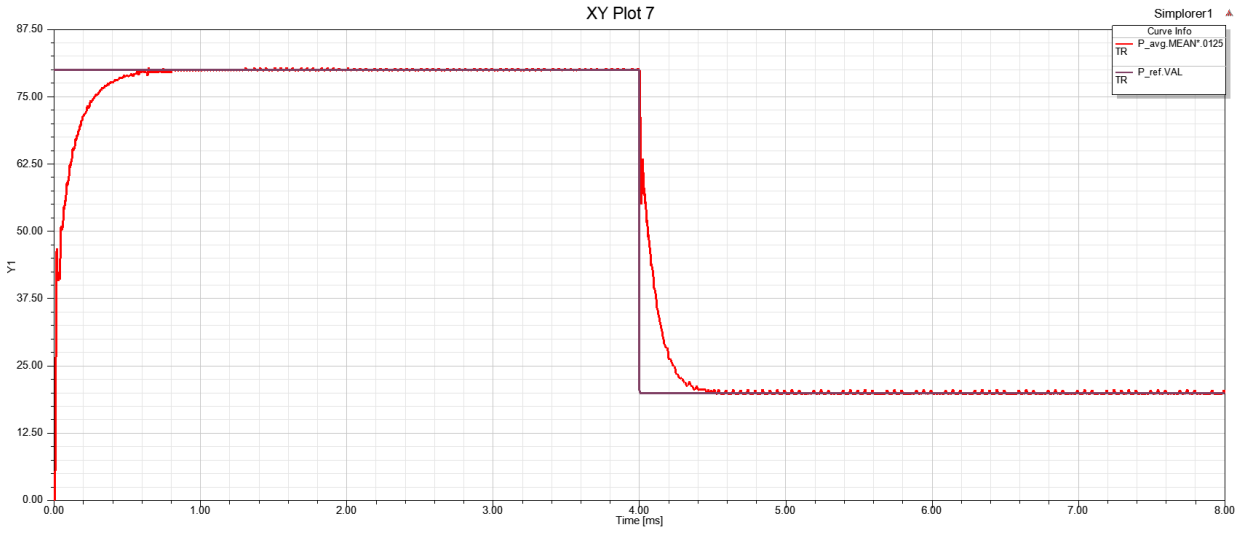

Figure 2.8. Step response from 80 to 20 percent of average power (100 V both ends of transformer).

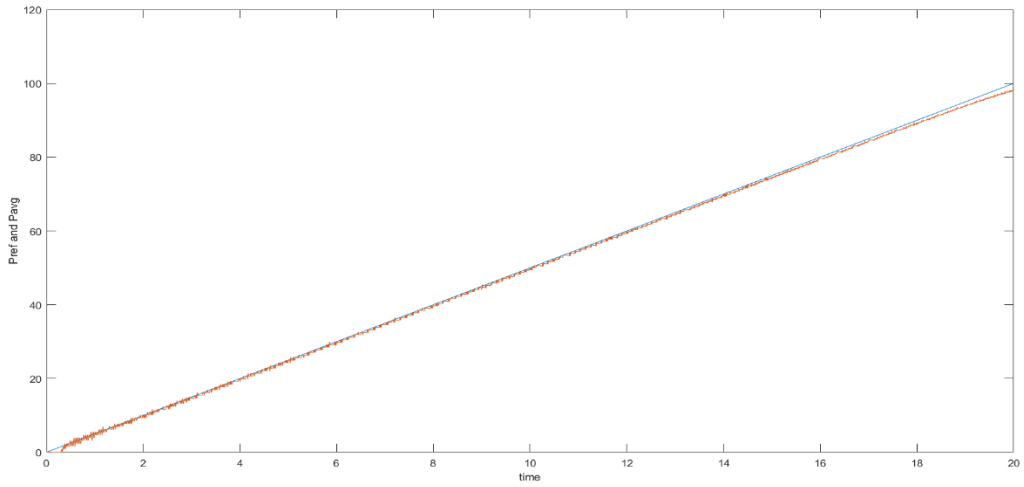

Figure 2.9. Tracking of Pavg and Pref in Matlab.

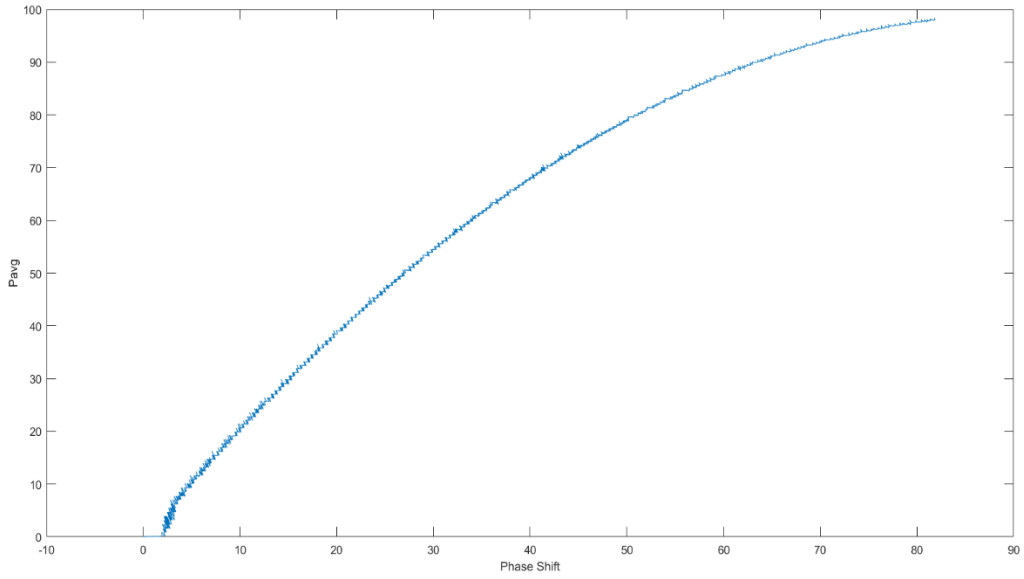

Figure 2.10. Phase shift Vs Pavg waveform.

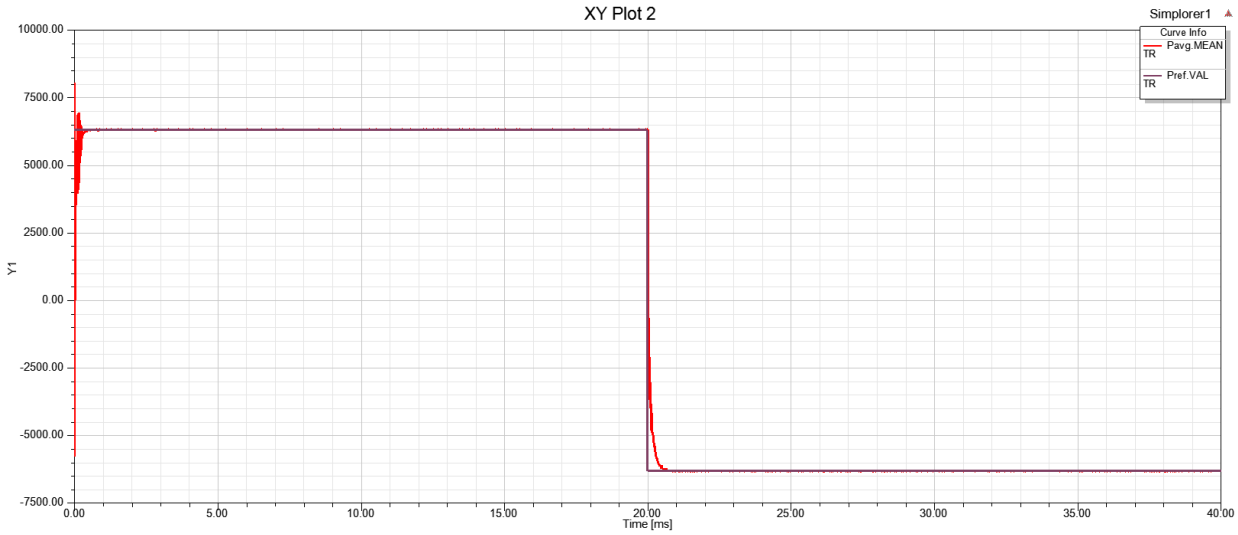

Figure 2.11. Step response from 70 to -70 percent of average power (Different voltage, V1=100V and V2=150V).

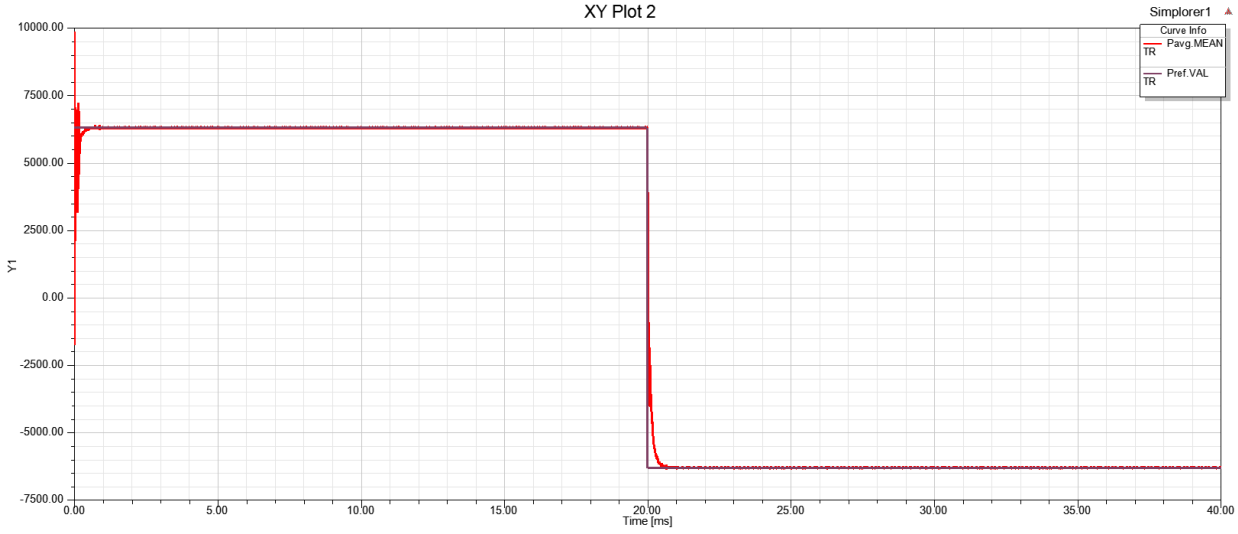

Figure 2.12. Step response from 70 to -70 percent of average power (Different voltage, V1=150V and V2=100V)

2.3 Waveforms (primary side of transformer)

2.3.1 100 V applied both sides of the transformer

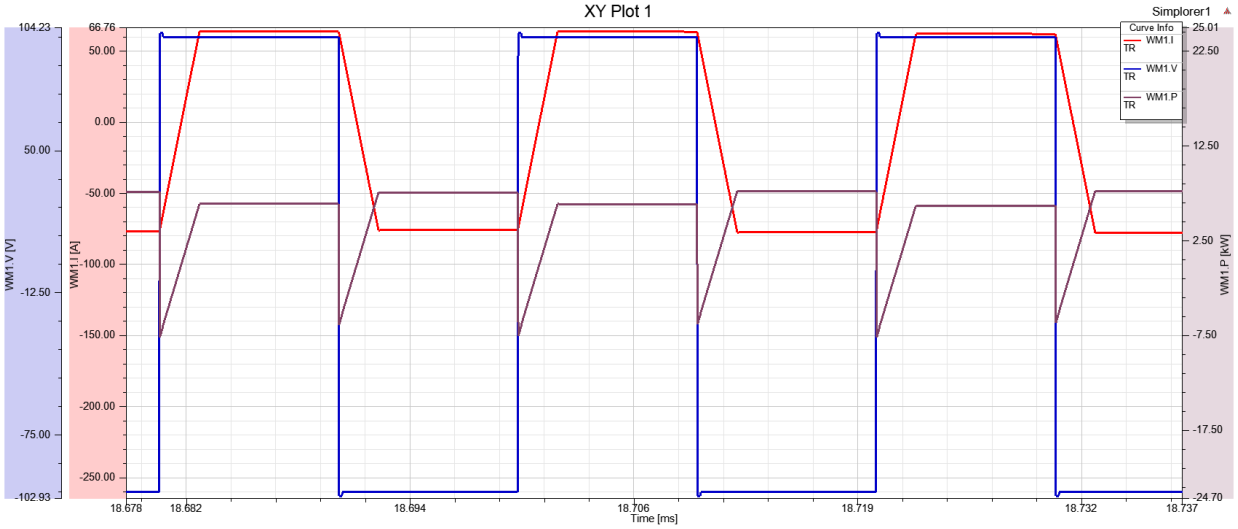

Voltage (primary side of transformer):

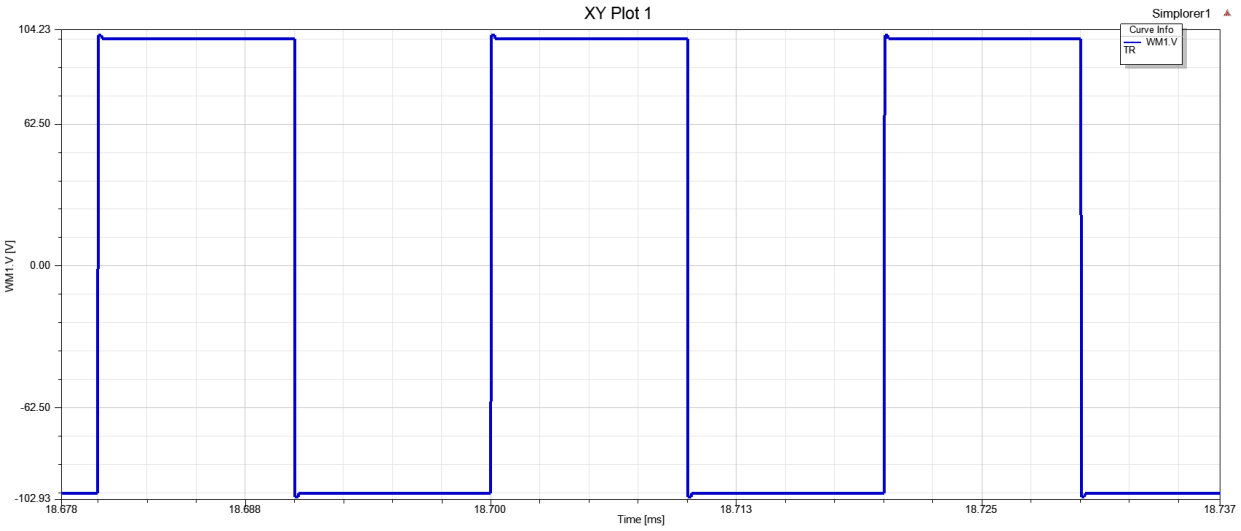

Current (primary side of transformer):

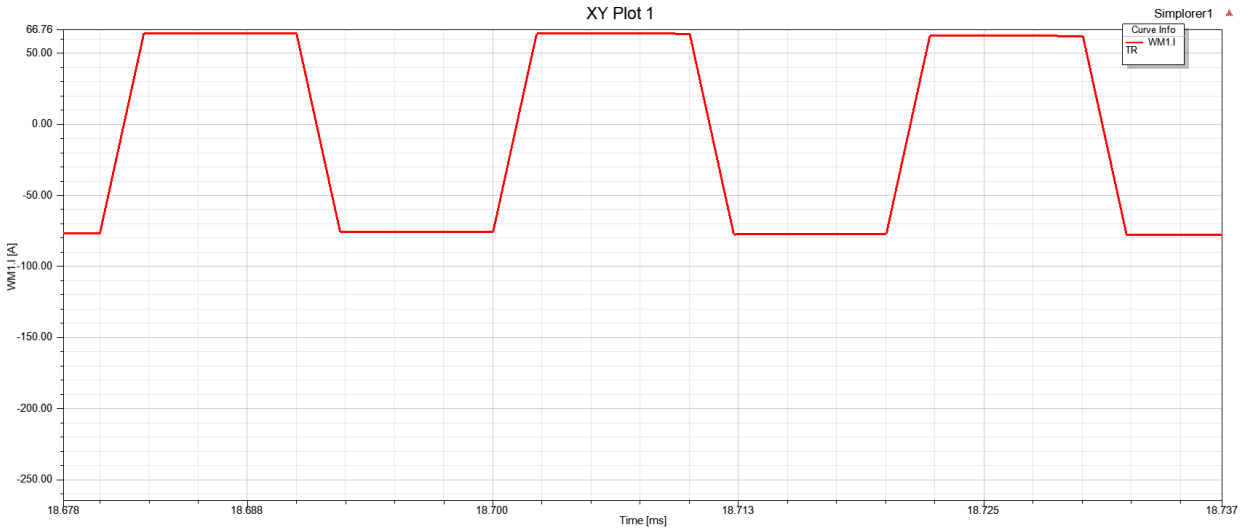

Power (primary side of transformer):

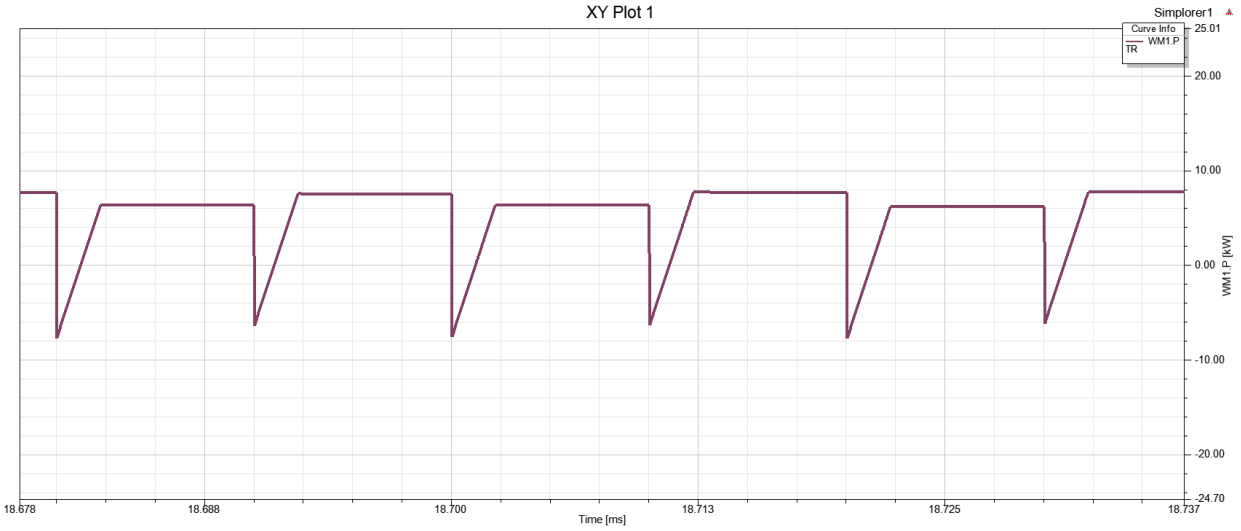

2.3.2 V1=100V and V2=150V (Positive Phase shift)

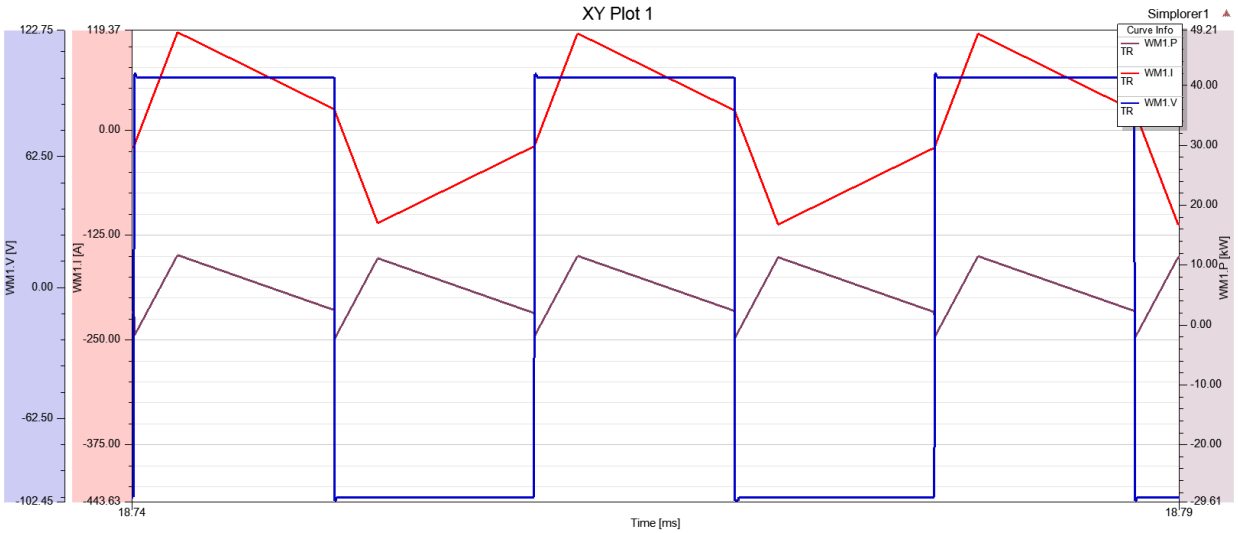

Current (primary side of transformer):

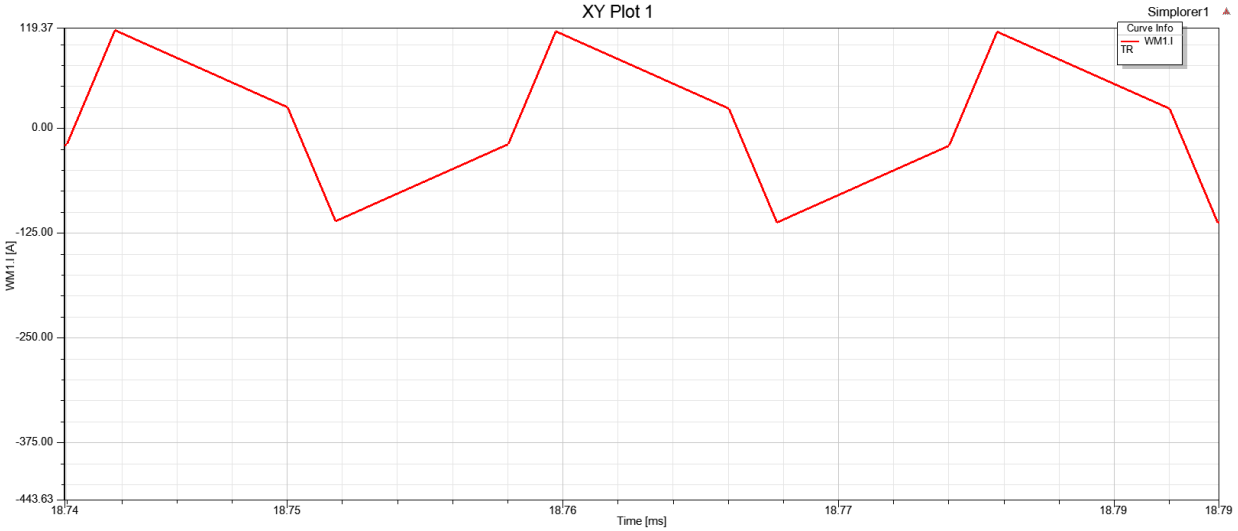

Power (primary side of transformer):

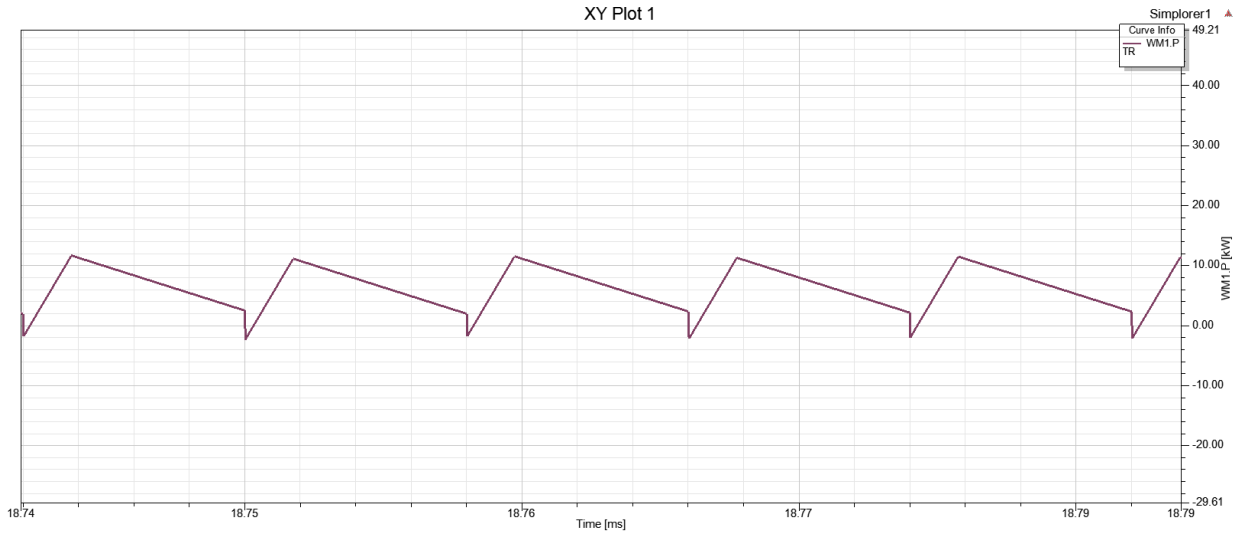

2.3.3 V1=100V and V2=150V (Negative Phase shift)

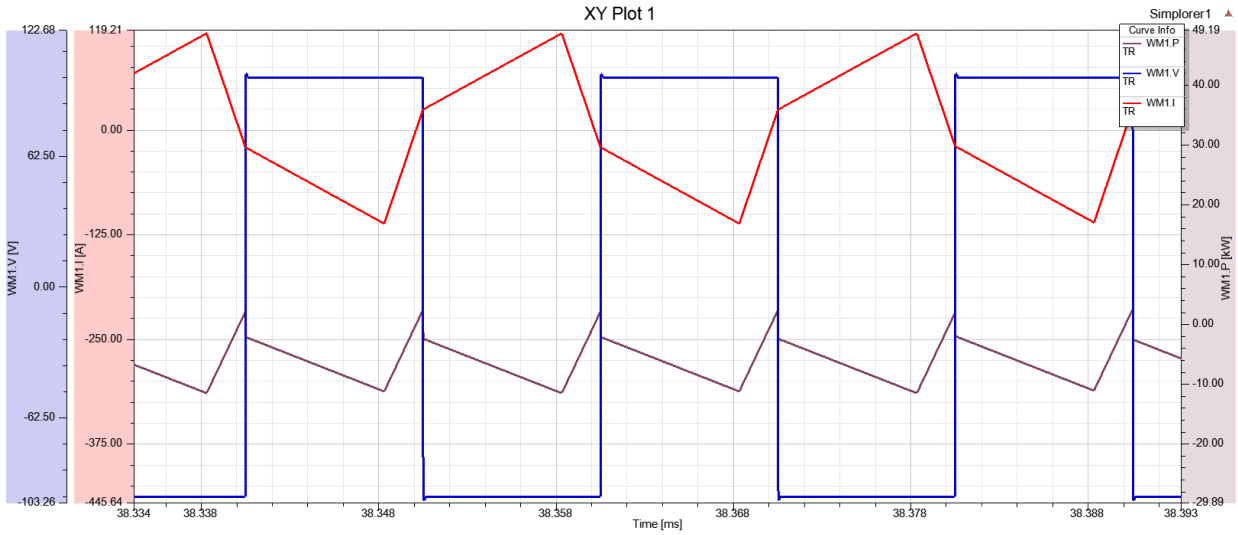

Current (primary side of transformer):

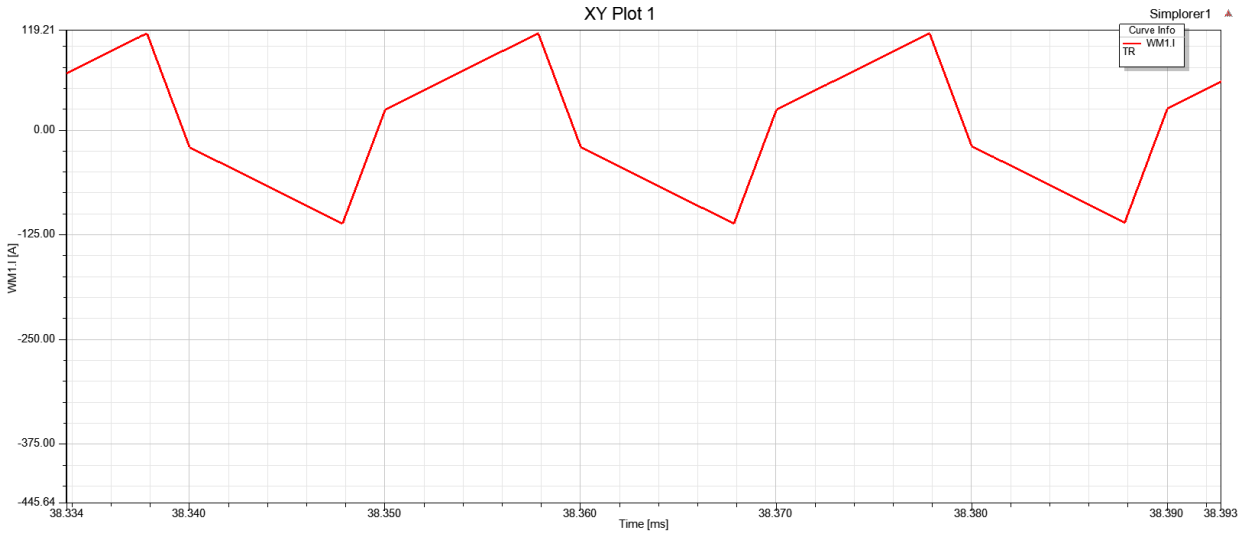

Power (primary side of transformer):

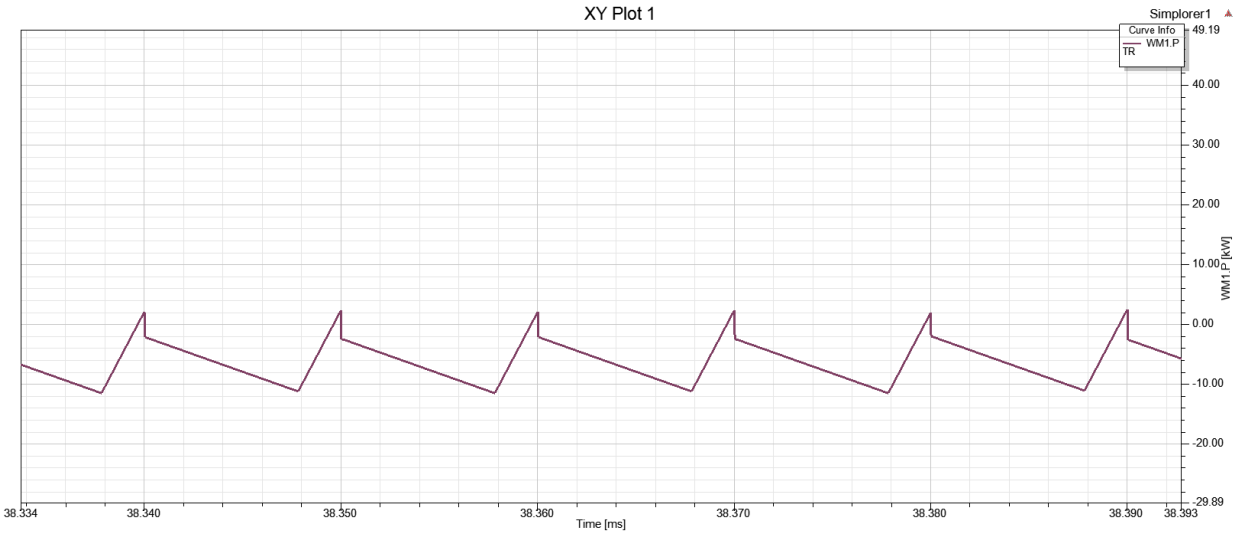

2.3.4 V1=150V and V2=100V (Positive Phase shift)

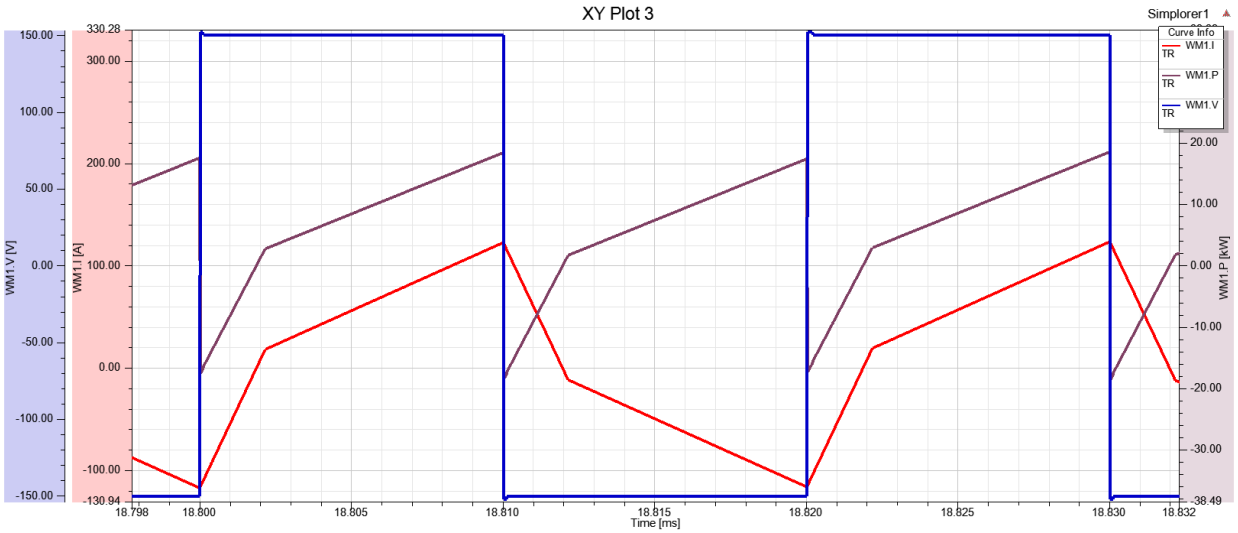

Current (primary side of transformer):

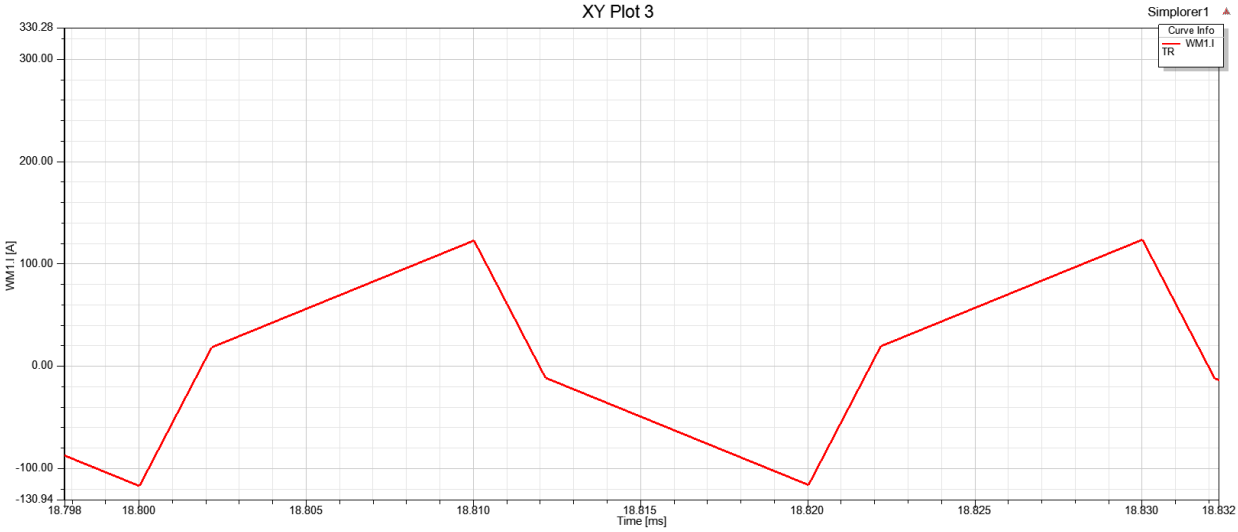

Power (primary side of transformer):

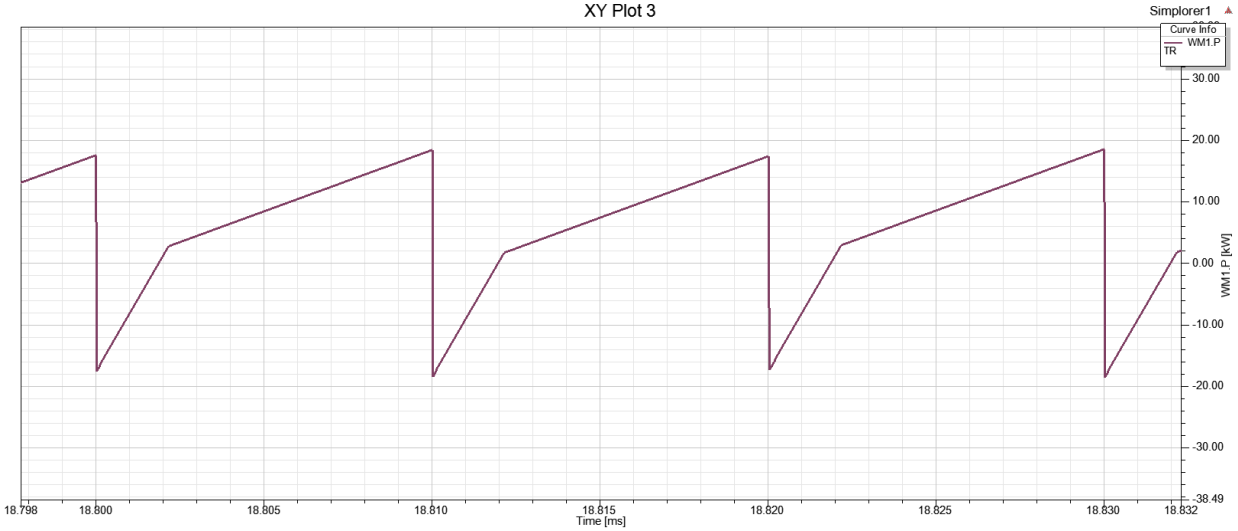

2.3.5 V1=150V and V2=100V (Negative Phase shift)

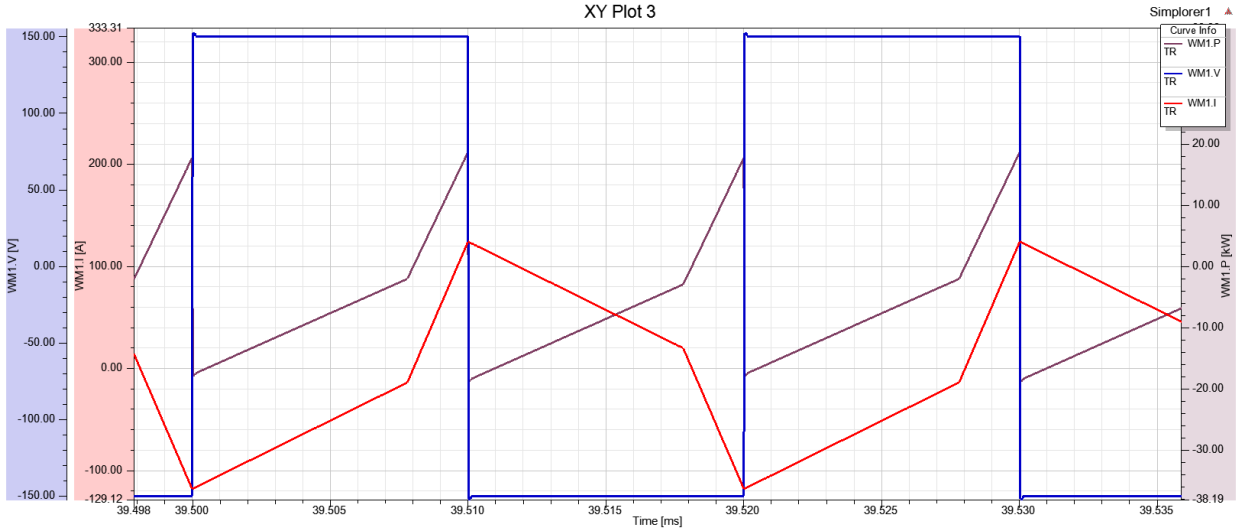

Current (primary side of transformer):

Power (primary side of transformer):

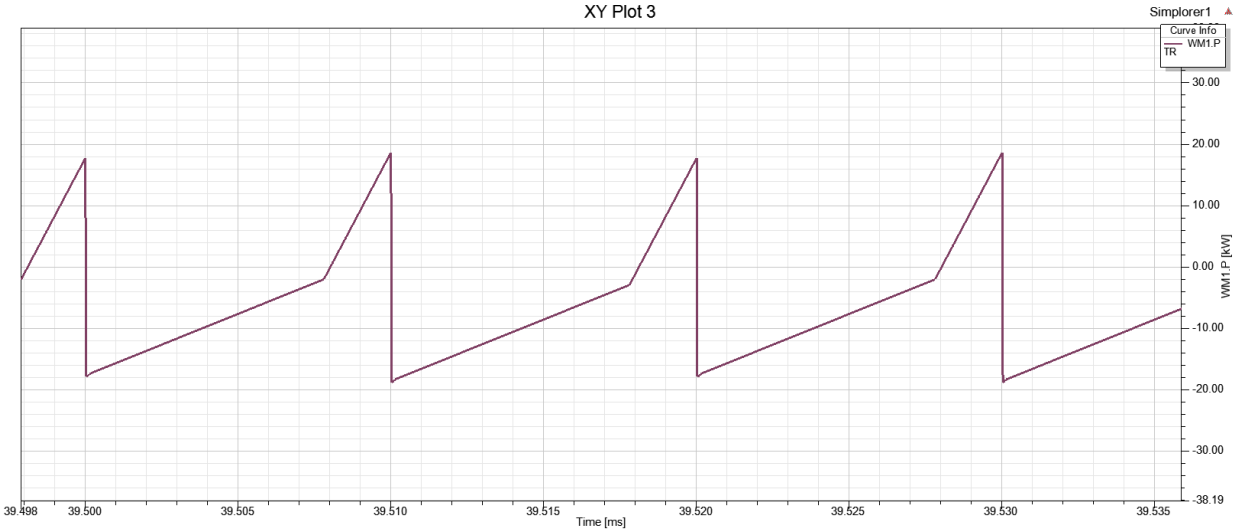

Chapter 3: Four-port DC-DC converter modelling and control of power flow

3.1 Four-port DC-DC converter

In four-port DC-DC converter, different kind of sources like renewable energy, conventional power sources can be connected and supply to the load can be ensured. High frequency four-port transformer can be used for galvanic isolation and different control method can be implemented to control power transfer between the four ports.

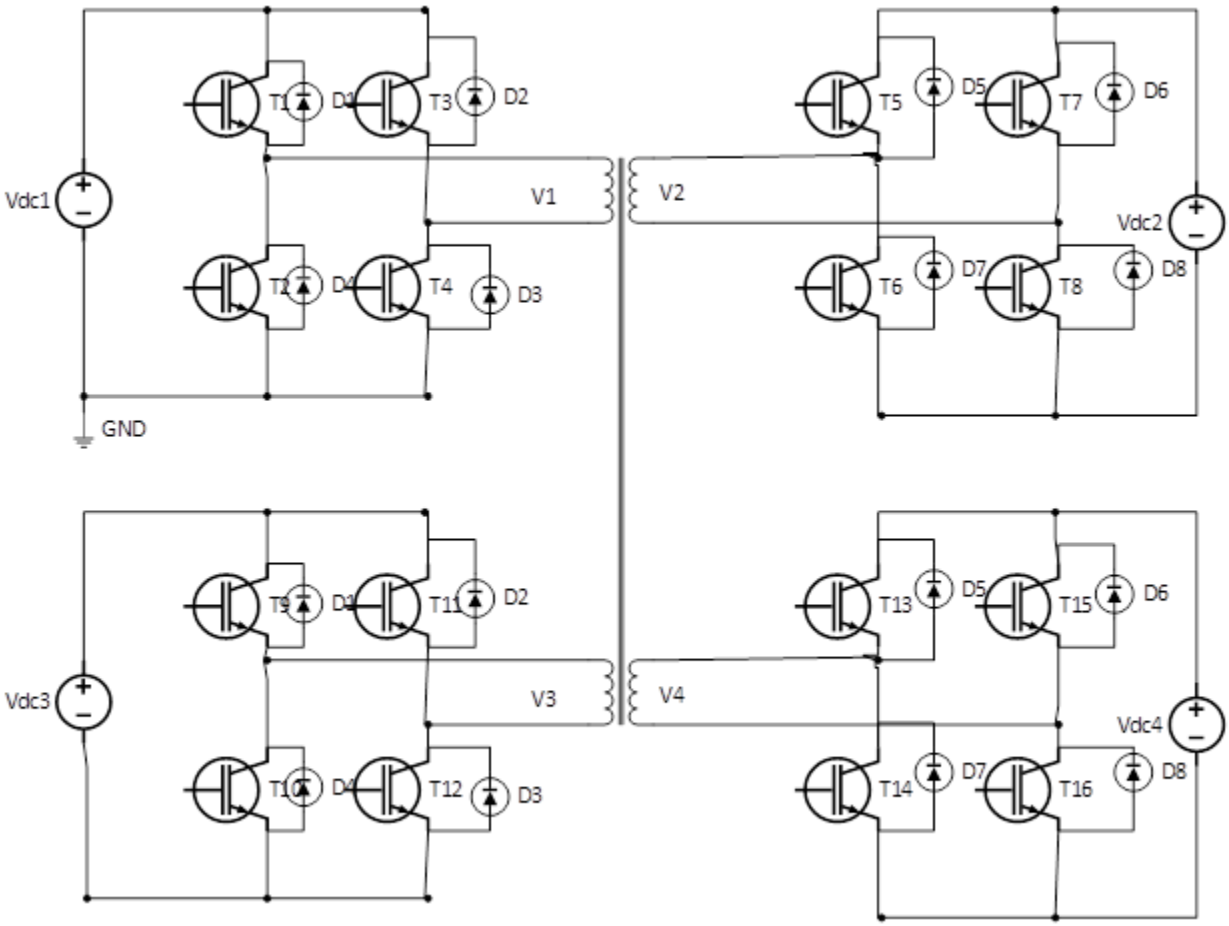

Figure 2.13. Four-port DC-DC converter circuit.

3.2 Parameter derivation for four-port transformer of DC-DC converter

Current flowing through the winding and voltage across each port generates magnetic flux which have two components. Magnetic and leakage component are those two components [9], [10].

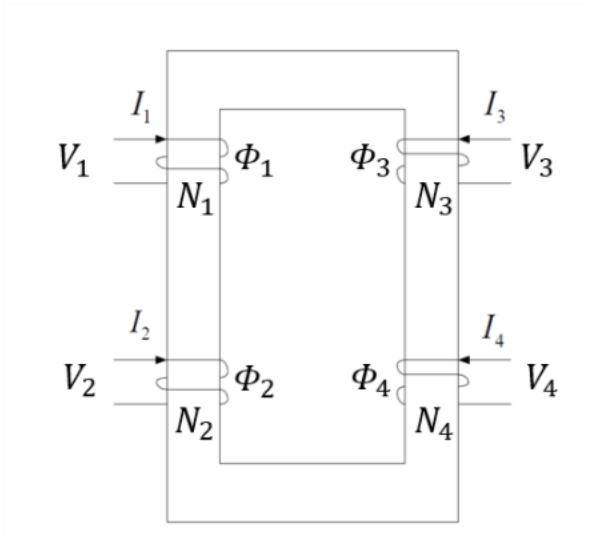

Figure 2.14. Magnetic representation of four port transformer [10].

Flux linkage in the windings produced by current are

$$\Phi_1 = \Phi_{l1} + \Phi_{m1} + \Phi_{m2} + \Phi_{m3} + \Phi_{m4} \quad (3.1)$$

$$\Phi_2 = \Phi_{l2} + \Phi_{m2} + \Phi_{m1} + \Phi_{m3} + \Phi_{m4} \quad (3.2)$$

$$\Phi_3 = \Phi_{l3} + \Phi_{m3} + \Phi_{m1} + \Phi_{m2} + \Phi_{m4} \quad (3.3)$$

$$\Phi_4 = \Phi_{l4} + \Phi_{m4} + \Phi_{m1} + \Phi_{m2} + \Phi_{m3} \quad (3.4)$$

Voltage equation in matrix form,

$$V = rI + \frac{d\lambda}{dt} \quad (3.5)$$

Self-inductances can be expressed as,

$$L_{11} = \frac{N_1^2}{\Re_{l1}} + \frac{N_1^2}{\Re_m} = L_{l1} + L_{m1} \quad (3.6)$$

$$L_{22} = \frac{N_2^2}{\Re_{l2}} + \frac{N_2^2}{\Re_m} = L_{l2} + L_{m2} \quad (3.7)$$

$$L_{33} = \frac{N_3^2}{\Re_{l3}} + \frac{N_3^2}{\Re_m} = L_{l3} + L_{m3} \quad (3.8)$$

$$L_{44} = \frac{N_4^2}{\Re_{l4}} + \frac{N_4^2}{\Re_m} = L_{l4} + L_{m4} \quad (3.9)$$

Magnetizing inductances can be expressed as

$$\frac{L_{m1}}{N_1^2} = \frac{L_{m2}}{N_2^2} = \frac{L_{m3}}{N_3^2} = \frac{L_{m4}}{N_4^2} \quad (3.10)$$

Mutual inductances are

$$L_{12} = L_{21} = \frac{N_1 N_2}{\Re_m},$$

$$L_{13} = L_{31} = \frac{N_1 N_3}{\Re_m}$$

$$L_{14} = L_{41} = \frac{N_1 N_4}{\Re_m},$$

$$L_{23} = L_{32} = \frac{N_2 N_3}{\Re_m}$$

$$L_{34} = L_{43} = \frac{N_3 N_4}{\Re_m} \quad (3.11)$$

The flux linkages can be expressed in matrix:

$$\begin{bmatrix}\lambda_1\\ \lambda_2\\ \lambda_3\\ \lambda_4\end{bmatrix} = \begin{bmatrix}L_{11} & L_{12} & L_{13} & L_{14}\\ L_{21} & L_{22} & L_{23} & L_{24}\\ L_{31} & L_{32} & L_{33} & L_{34}\\ L_{41} & L_{42} & L_{43} & L_{44}\end{bmatrix}\begin{bmatrix}I_1\\ I_2\\ I_3\\ I_4\end{bmatrix} \tag{3.12}$$

3.3 Inductor current and power flow analysis for four-port DC-DC converter

Four-port DC-DC converter is shown in Figure 2.13. Four port transformer model will be modeled in next chapter which will be used as isolation transformer. Y and Δ equivalent circuit are shown in Figure 2.15, Figure 2.16 [11].

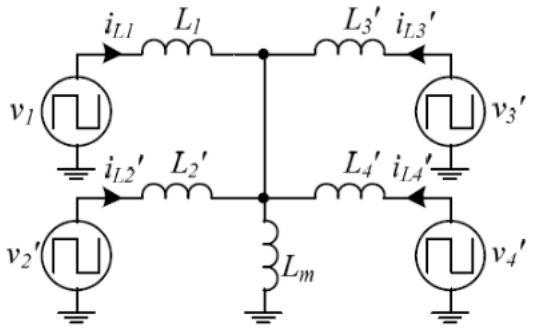

Figure 2.15. Four-port Y equivalent circuit referred to port 1 [11].

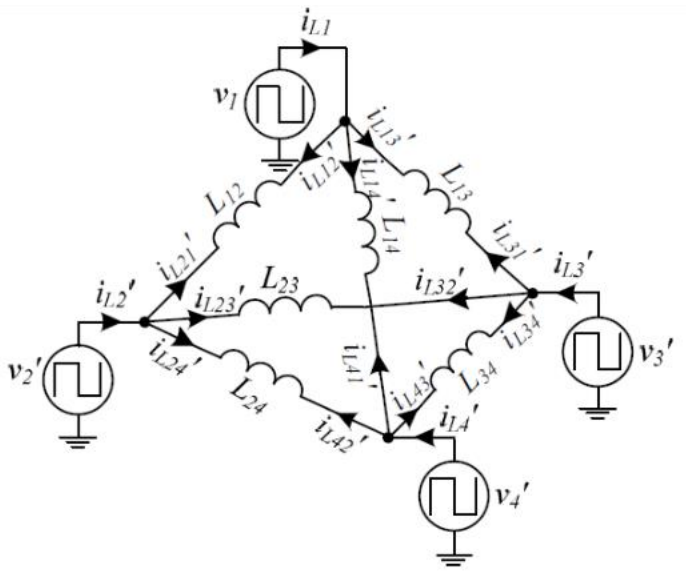

Figure 2.16. Four-port Δ equivalent circuit referred to port [11].

Power flow from one port to another port can be expressed as

$$P_{jk} = \frac{V_j' V_k'}{2\pi f_s L_{jk}} \varphi_{jk} \left(1 - \frac{|\varphi_{jk}|}{\pi}\right)$$

$$\varphi_{jk} = \varphi_j - \varphi_k$$

Here power is transferring from j port to k port and φ_j, φ_k are phase shift angles. V_j', V_k' are AC voltages referred to port 1 and L_{jk} is equivalent leakage inductance between port j and k.

3.4 Phase shift control of four-port DC-DC converter

Phase shift control method was implemented to control power flow between the four ports of this converter. Four-port DC-DC converter will be operated on constant high switching frequency

with a constant duty cycle will be 50%. Power transfer in all four ports will be possible by varying phase shift in close loop control.

All calculation can be referred to any single port. Power of the 2nd, 3rd and 4th port of the transformer is measured. Then average power P_{avg} of 2nd, 3rd and 4th port for every switching period is calculated. Phase shift φ_1 is set to zero of the referred port. Power regulator compares P_{avg} and P_{ref} to generate phase shift angle $\varphi_2, \varphi_3, \varphi_4$. A limiter can be used to maintain the phase shift angle within range [8].

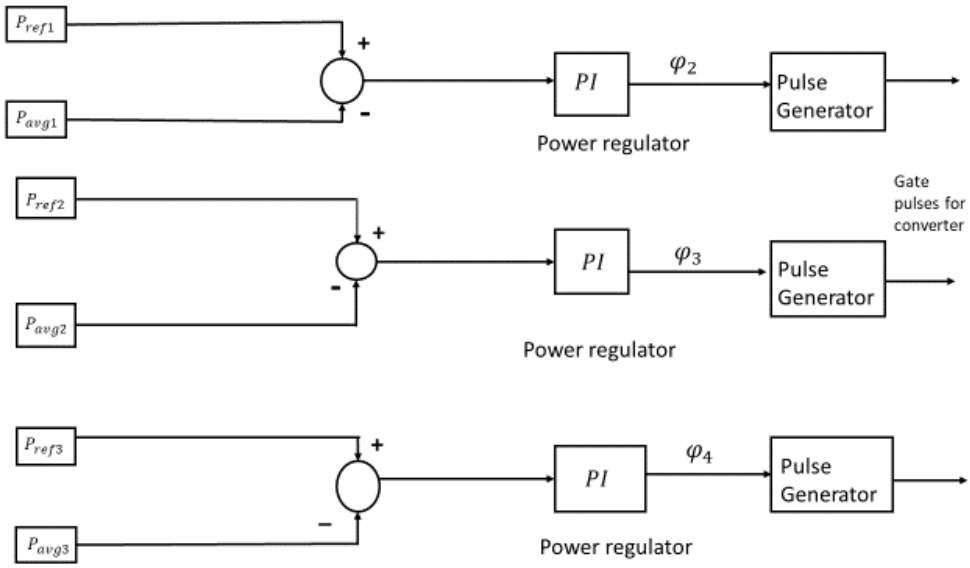

Figure 2.17. Control blocks for phase shift control of four-port DC-DC converter.

Because of the phase shift $\varphi_2, \varphi_3, \varphi_4$ generated by power regulator, we can get gate pulses for 2nd, 3rd and 4th port of the DC-DC converter. This controlled phase shift helps the converter to transfer power in any of the four ports.

3.4.1 Controller performance analysis

The four port converter was rated for 8000 watt. One end of the converter was set (P_{ref1}) to deliver 80 percent of the rated average power and controller was compared with P_{avg1} . Other two ports were set (P_{ref2}, P_{ref3}) to receive 30 and 50 percent of the rated average power and was compared with P_{avg2}, P_{avg3} . From Figure 2.18 the tracking of average power can be observed. One port was set not to either receive or deliver any power.

Phase shift angles can be observed in Figure 2.19 in close loop control. Positive phase angle can be found in the converter port that is delivering power. On the other hand, two ports which are receiving power have negative phase shift. Switching gate pulse of the delivering end of the converter will lag from receiving end of the converter, it was shown in Figure 2.20.

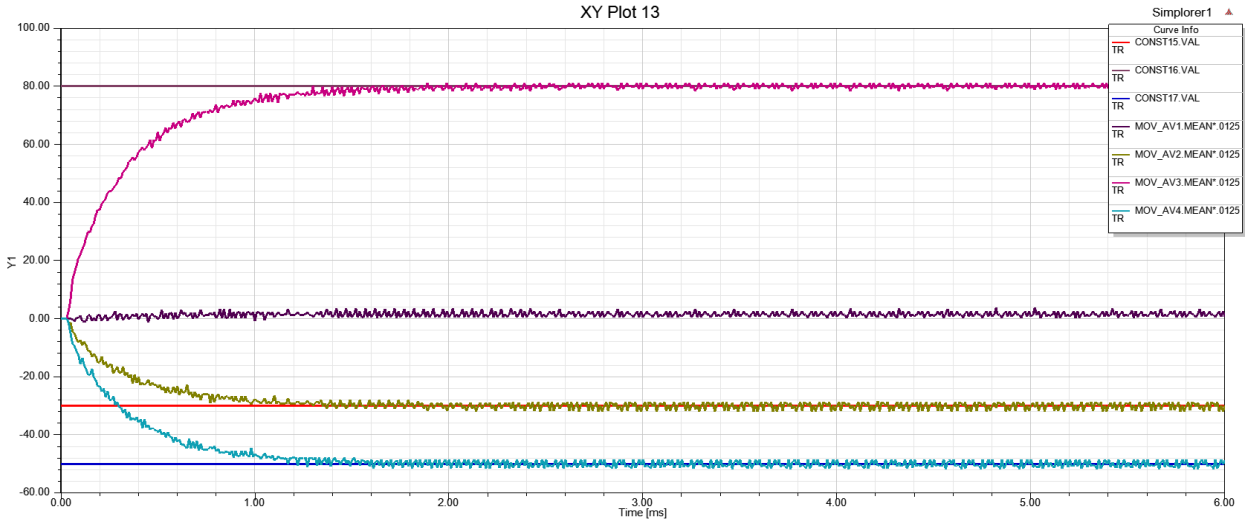

Figure 2.18. Power tracking response for different set point in four ports.

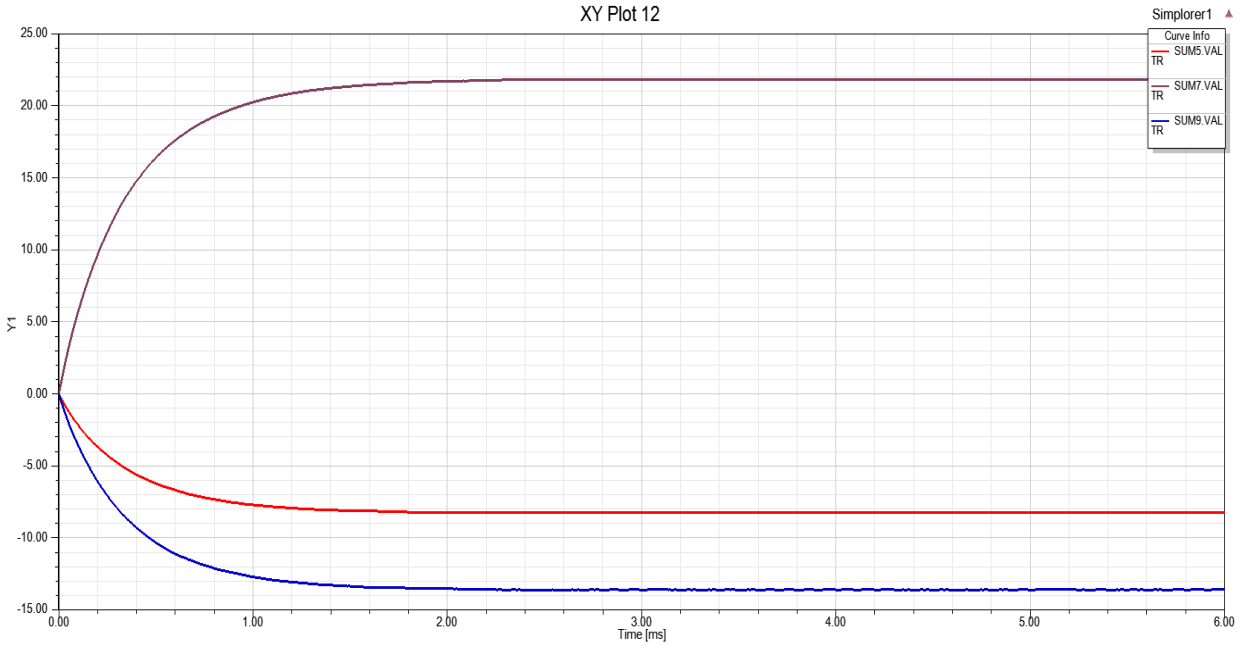

Figure 2.19. Phase shift angles of different ports.

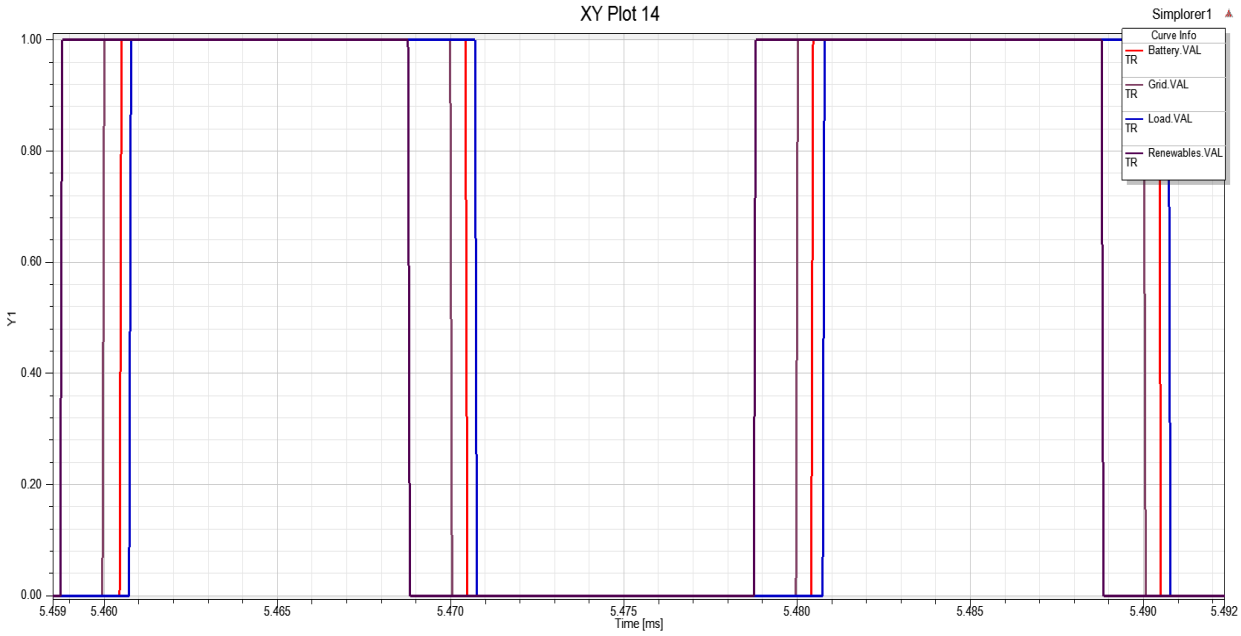

Figure 2.20. Switching gate pulses for four ports in close loop control.

3.5 Waveforms (primary side of transformer)

Current (open loop, $\varphi_1 = 0, \varphi_2 = 35, \varphi_3 = 40, \varphi_4 = 45$, 100V in four port) :

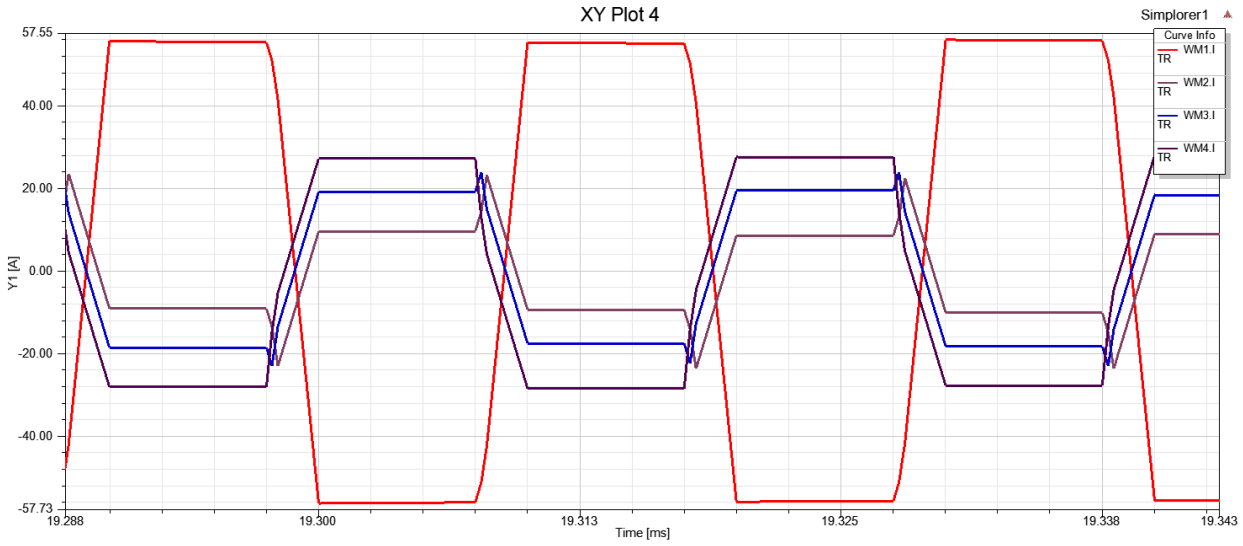

Power (open loop, $\varphi_1 = 0, \varphi_2 = 35, \varphi_3 = 40, \varphi_4 = 45$, 100V in four port):

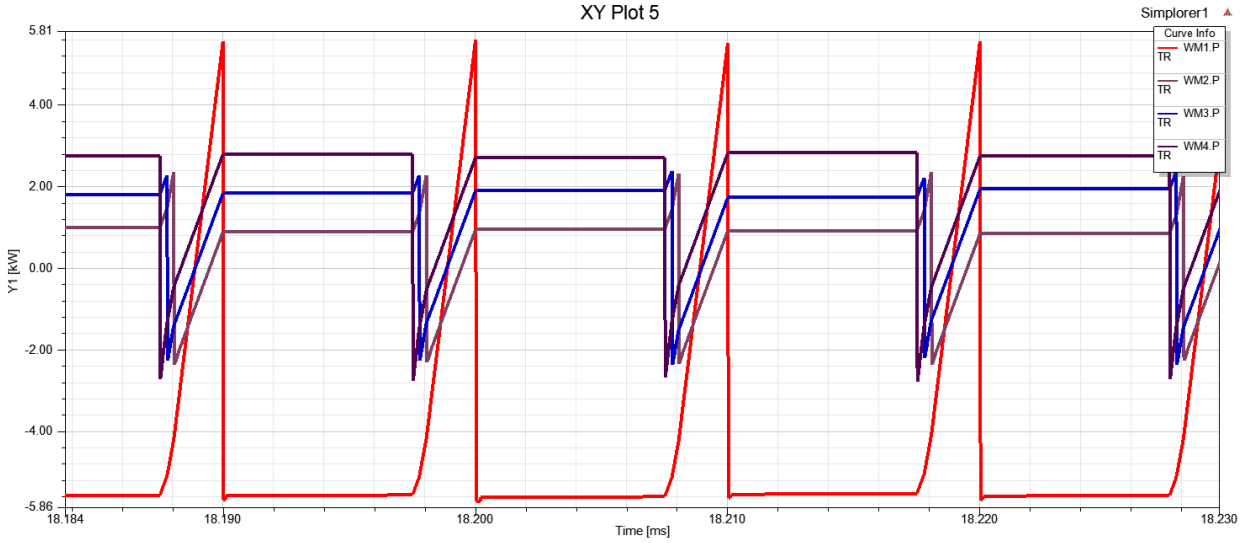

Current (close loop, 3rd port):

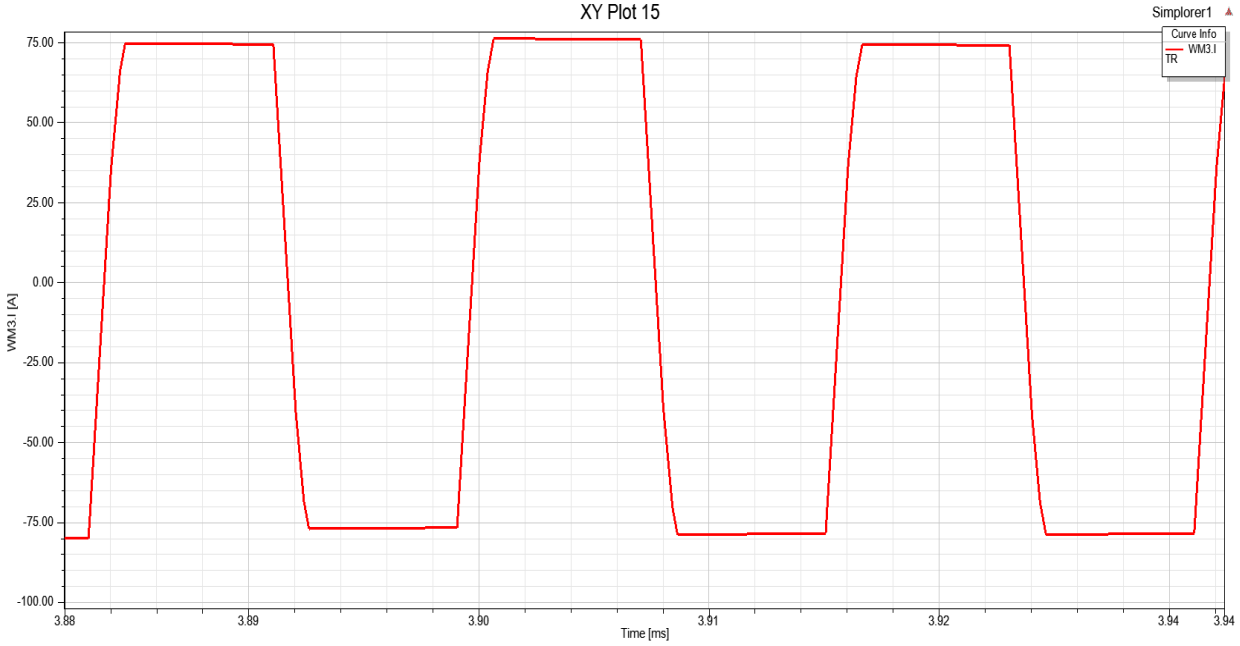

Power (close loop, 3rd port, delivering power):

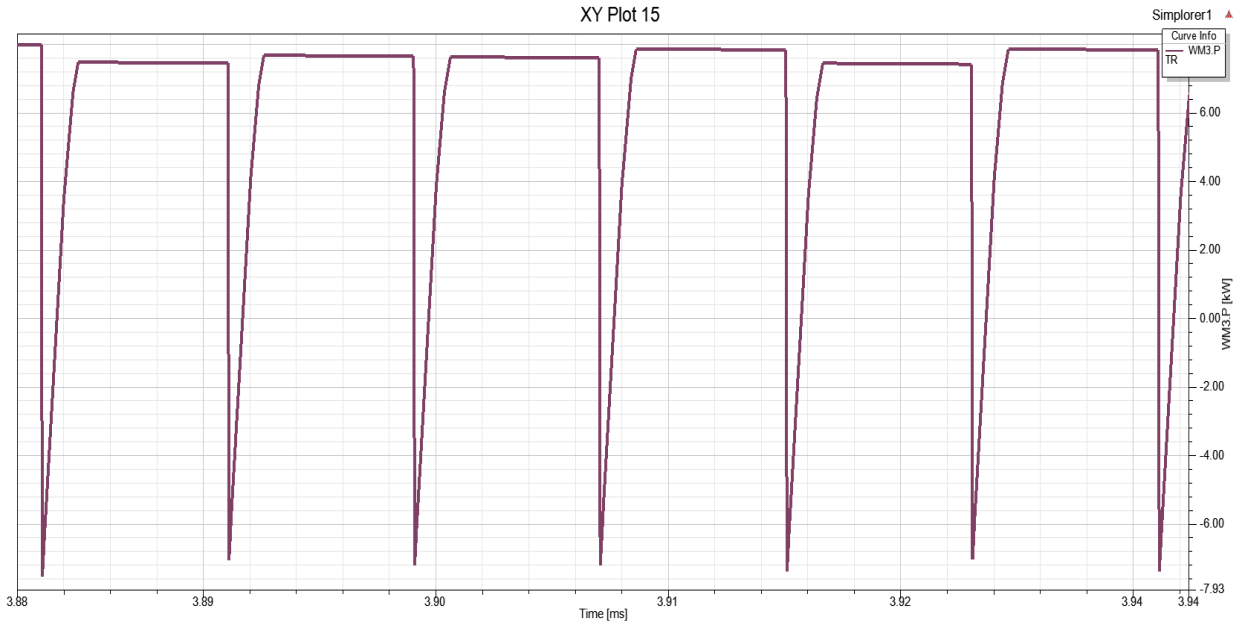

Chapter 4: Four-port transformer design for DC-DC converter

4.1 Material Selection

To construct high frequency transformer, materials selection for core plays very important role. Judicious selection of core materials helps reducing core loss for high frequency application. For high frequency application normally ferrites, amorphous metals and nanocrystalline are considered.

Ferrite cores are ceramic materials that have lower flux density [12], [13], [14], [15] . It has saturation flux density around 0.3-0.5 Tesla that can get lower if the core temperature is increased. For high frequency application, it has high electrical resistivity which will ensure low eddy current loss. In ferrite materials, because of high frequency application core loss density can increase and permeability can reduce which can fail the core. As an example, Ferroxcube 3C94 ferrite material's initial permeability, saturation of flux density and core loss density as a function of temperature are given below.

From figures below, it could be realized that loss variation along temperature is a matter of concern for selection of ferrite materials. The limit of saturation of flux density will reduce because of temperature rise of the core. Permeability variation due to temperature will change the inductance which will be very difficult for circuit operation [15].

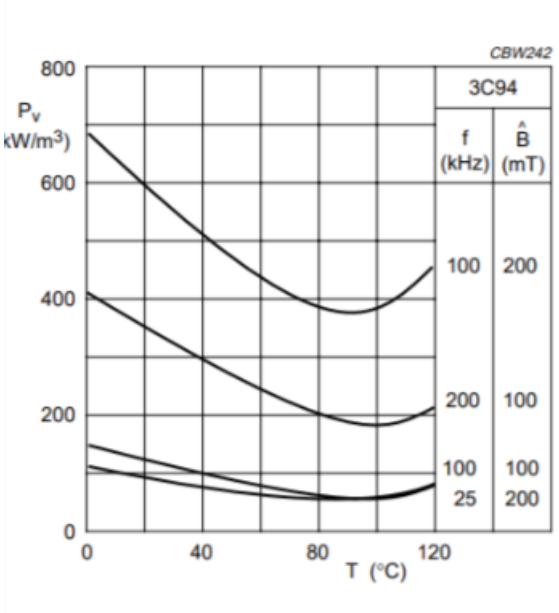

Figure 2.21. Specific power loss for several frequency/flux density as function of temperature.

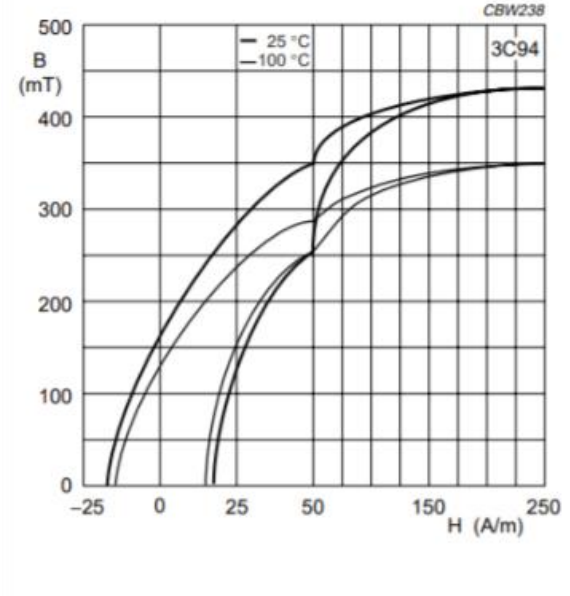

Figure 2.22. B-H curve and temperature dependence.

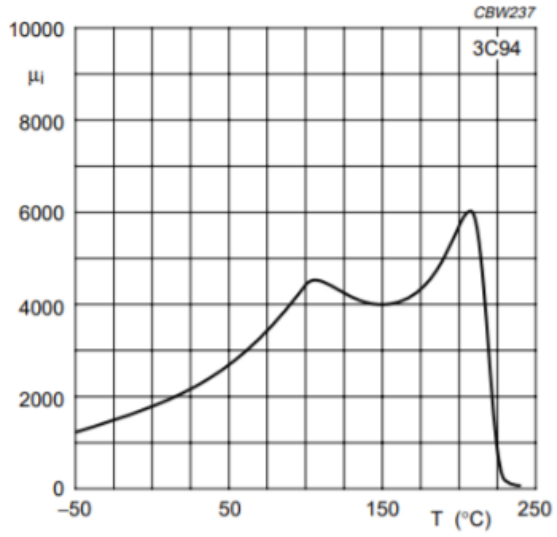

Figure 2.23. Initial permeability as a function of temperature.

Amorphous metals show high saturation flux density near 1.56 Tesla [14] because of higher concentration of magnetic species [15]. It has higher loss density like ferrite materials and with increasing frequency permeability will reduce. The loss density is higher than ferrite and nanocrystalline materials but lower than silicon steel.

Nanocrystalline materials can also be considered for high frequency application. It has high saturation flux density of 1.2 Tesla. Relatively low loss density and high Curie temperature is also useful for high frequency power application. It preserves magnetic characteristics for high temperature range because of high curie temperature.

From [13] we can observe that lower core loss was shown by ferrite and nanocrystalline materials compared to amorphous metals. Core area product for nanocrystalline is much less than ferrite core because of high saturation flux density. But as nanocrystalline is very costly

compared to ferrite, it can only be used in applications where cost is not that much in concern. Otherwise, ferrite is a good option for high frequency application.

4.2 Core loss analysis

Core loss can generally be divided into three categories:

a) Hysteresis models

b) Loss separation approach

c) Empirical methods

4.2.1 Hysteresis models

Hysteresis Model can be explained based on [16], [17], [18] .Jiles-Atherton model explained statistical approach to describe time and space distribution of domain wall motion.

$$\frac{dM_{irr}}{dH} = \frac{M_{an} - M_{irr}}{k\delta - \alpha(M_{an} - M_{irr})}$$

$$M_{rev} = c(M_{an} - M_{irr})$$

$$M_{an}(H) = M_s \left[coth\left(\frac{H + \alpha M}{\alpha}\right) - \frac{\alpha}{H + \alpha M} \right]$$

M_{rev} is reversible component of Magnetization M that describes domain wall bending during the magnetization process. M_{irr} is irreversible component of Magnetization M that describes domain wall displacement against the pinning effect. a, c, k, α and saturation magnetization M_s can be found from measured hysteresis characteristics. δ here is a directional parameter.

In [18] Jiles-Atherton hysteresis model was applied for numerical modelling of measured magnetic hysteresis characteristics. Modifications of the original Jiles-Atherton hysteresis model was developed to get a new combined Jiles-Atherton and scaling model.

4.2.2 Loss separation approach

In loss separation method static hysteresis loss P_{hys}, eddy current loss P_c, and excess eddy-current loss P_{ex} are contributing to magnetization loss. Total core loss can be expressed as

$$P_{core\_total} = P_{hys} + P_c + P_{ex}$$

4.2.2.1 Eddy current loss

From [19] piecewise-linear voltage wave with time T for average core loss density can be written as

$$P_c = \frac{A}{8\pi\rho}\frac{1}{T}\sum_{i=1}^{n}\left[\int_{t_{i-1}}^{t_i}\left(\frac{dB_i(t)}{dt}\right)^2 dt\right]$$

A is the cross section of the core and ρ is the resistivity of the core material. For sinusoidal waveforms the average core loss density is

$P_c^{sin} = \frac{A}{16\pi\rho}(2\pi f B_o)^2 \;\; B_0 = \frac{V_o}{2\pi f NA}$

Here f is frequency, V_o is peak voltage, B_o is peak flux density.

For square waveforms the net core loss density is

$$P_c^{square} = \frac{A}{8\pi\rho}(4fB_0)^2\frac{1}{D}$$

Here $D = \frac{t_{on}}{T}$ is duty ratio.

4.2.2.2 Static hysteresis loss

Many methods are available to measure hysteresis loss among them Jiles-Atherton model [17] is commonly used. [19] followed [20] to calculate hysteresis loss where a practical model was used

to calculate hysteresis loops hysteresis loss. Reduced properties of soft materials were extracted to get nonlinear magnetization curves, and nonlinear permeability, dependence of hysteresis loss on the flux density. Either it is sinusoidal or square waveforms hysteresis loss is not dependent on frequency though they have same peak flux density.

4.2.2.3 Excess eddy-current loss

Magnetic domains inside magnetic materials are origin of excess eddy current loss. Magnetic domains are separated by domain walls and in normal condition they are uniform. Bertotti [21] proposed a statistical loss theory where a number of active correlation regions are considered randomly in materials.

The change of magnetization state of materials caused by applied field in domain walls is responsible for excess eddy current loss.

Based on [19], [21] instantaneous excess eddy current loss is-

$$P_{ex} = \sqrt{\frac{A\alpha n_o}{\rho}} \left(\frac{dB(t)}{dx}\right)^{\frac{3}{2}}$$

Where α is numerical constant and n_0 is statistical distribution of the local coercive fields.

For the piecewise linear waveforms, we can get the average excess loss density

$$P_{ex} = \sqrt{\frac{A\alpha n_o}{\rho}} \frac{1}{T} \sum_{i=1}^{n} \int_{t_{i-1}}^{t_i} dt \left\{ \left| \frac{dB_i(t)}{dt} \right|^{3/2} \right\}$$

For sinusoidal waveforms, average excess eddy current loss density as

$$P_{ex}^{sine} = 3.5\sqrt{\frac{2\pi A\alpha n_o}{\rho}}\ (fB_o)^{3/2}$$

Square-wave voltage waveform, can be obtained for the average excess eddy current loss density as

$$P_{ex}^{square} = 8\sqrt{\frac{\pi A\alpha n_o}{\rho}}(fB_o)^{3/2}\frac{1}{\sqrt{D}}$$

4.2.3 Empirical methods

We can get satisfactory loss analysis from static hysteresis loss model or loss separation model. But both method is dependent on large scale data, extensive computation and experimental results. Empirical approach uses manufacturer provided data to determine loss which is easier than two methods. There are several methods that can explain core loss are given below.

4.2.3.1 OSE Method

From [22], [23] we can get Steinmetz equation for only sinusoidal equation that explains transformer or inductor loss with the help of curve fitting expression of measured data.

$$P_v = Kf^{\alpha}B_m^{\beta}$$

B_m is the peak magnetic flux and K, α, β are determined by material characteristics. But this expression is not suitable for non-sinusoidal waveforms. If same peak flux density and frequency are applied for both non-sinusoidal and sinusoidal waveforms loss is more in former waveforms.

4.2.3.2 MSE Method

In [24] Steinmetz equation was modified for non-sinusoidal waveforms. It replaced f from OSE with equivalent frequency f_{eq}. It also relates magnetization loss with the rate of change of magnetic flux $\frac{dB(t)}{dt}$

$$f_{eq} = \frac{2}{\Delta B^2 \pi^2} \int_0^T \left(\frac{dB(t)}{dt} \right)^2 dt$$

Here ΔB is peak to peak flux amplitude.

Then the loss is determined by the Steinmetz equation replacing f_{eq},

$$P_v = \left(K f_{eq}^{\alpha-1} B_m^{\beta} \right) f_r$$

4.2.3.3 GSE

Generalized Steinmetz equation (GSE) considers the rate of change of magnetic induction with instantaneous value of flux density B(t) to correct OSE and MSE [25].

$$P_v = \frac{1}{T} \int_o^T k_1 \left| \frac{dB(t)}{dt} \right|^{\alpha} |B(t)|^{\beta-\alpha} \, dt$$

4.2.3.4 IGSE

From [26], we find that core loss not only depend on derivative and instantaneous value of flux density but also time history of flux waveform

$$P_v = \frac{1}{T} \int_o^T k_i \left| \frac{dB(t)}{dt} \right|^{\alpha} |\Delta B|^{\beta-\alpha} \, dt$$

$$k_i = \frac{K}{(2\pi)^{\alpha-1} \int_0^{2\pi} |cos\theta|^{\alpha} 2^{\beta-\alpha} \, d\theta}$$

Here in improved GSE (IGSE) instantaneous value of flux density was replaced with peak to peak value of flux density.

4.2.3.5 IIGSE

In [27], Improved IGSE relaxation process of materials was introduced to evaluate core loss. When flux is constant in previous works it was not addressed whether flux is constant or not. But different experiment showed because of relaxation process of material there will be loss when flux is constant. The new time average power loss density can be calculated with

$$P_v = \frac{1}{T}\int_o^T k_i \left|\frac{dB}{dt}\right|^{\alpha} |\Delta B|^{\beta-\alpha} dt + \sum_{l=1}^{n} Q_{rl} P_{rl}$$

P_{rl} and Q_{rl} are calculated while the voltage change

$$P_{rl} = \frac{1}{T} k_r \left|\frac{d}{dt} B(t_-)\right|^2 (\Delta B)^{\beta_r} (1 - e^{-\frac{t_1}{r}})$$

$$Q_{rl} = e^{-q_r} \left|\frac{dB(t_+)/dt}{dB(t_-)/dt}\right|$$

4.3 Core loss and flux density simulation

Some criteria to construct high frequency four port transformers are materials selection, evaluation of losses, core dimension, optimum flux density, winding characterization, leakage inductance calculation, etc. Here we will evaluate core loss and flux density for different voltage levels in Ansys Maxwell platform. The construction of the transformer in Ansys Maxwell was done following [28], [29] . Important factors to construct high frequency transformer are to minimize core loss, prevent saturation of the core, minimize skin effect and winding loss thorough selection of wire size.

4.3.1 Selection of core size and materials

While selecting core materials frequency range of the converter, flux density, core loss should be considered. For high frequency application nanocrystalline, silicone steel, ferrite, amorphous materials can be used. As ferrite materials core are available in different shape with low cost and power loss, we used Ferroxcube U93/76/30 materials 3C94 to build the transformer in Ansys Maxwell.

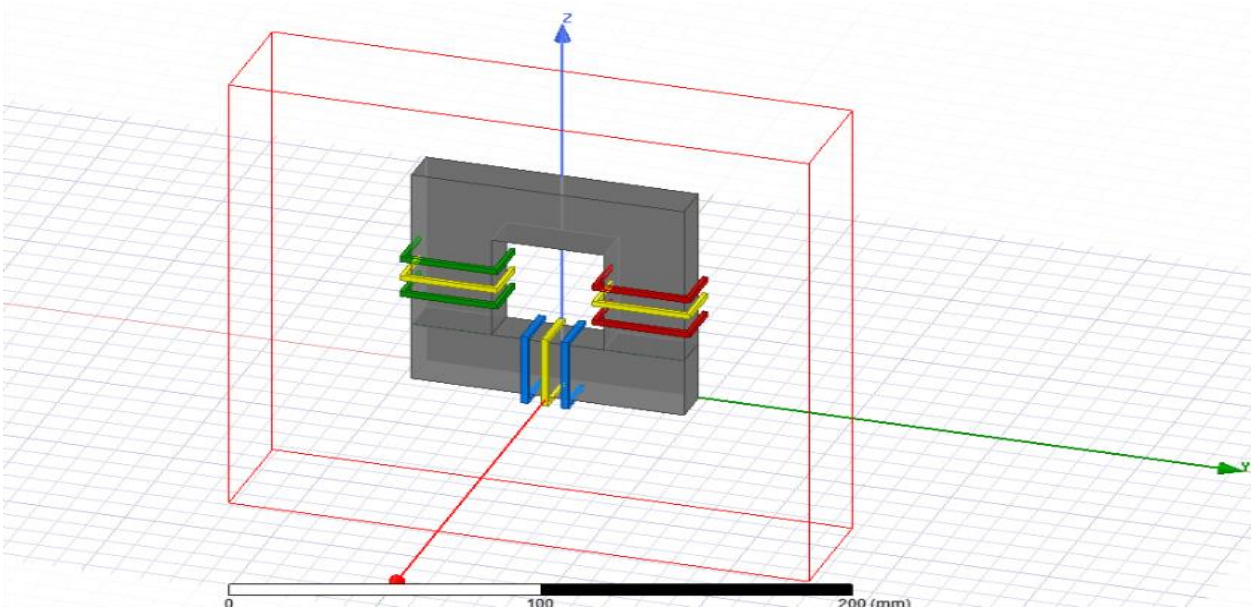

Figure 2.24. Four-port transformer design in Ansys Maxwell.

Dimension of the core size was followed according to ferroxcube data sheet for U93/76/30. We can find core dimensions in Figure 2.25.

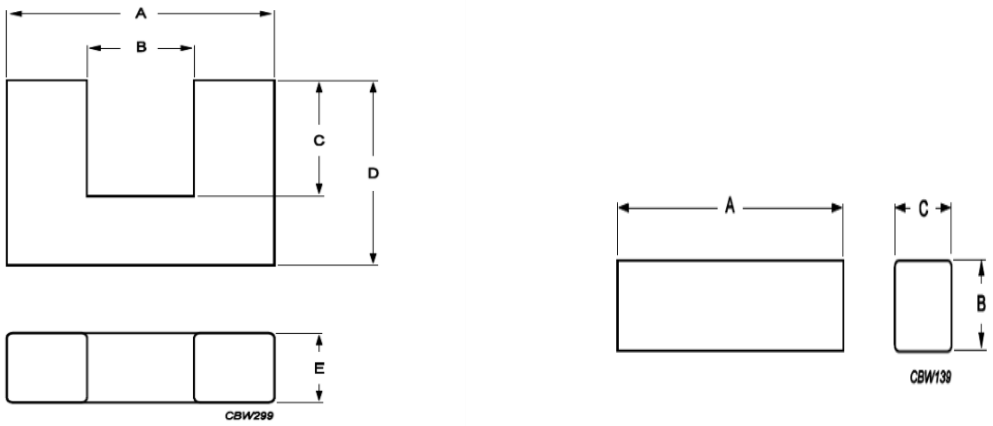

Dimensions for product: U93/76/30						
	Nom	Tol +	Tol -	Max	Min	Unit
A	93.00	1.80	1.80	94.80	91.20	mm
B	36.20	1.20	1.20	37.40	35.00	mm
C	48.00	0.90	0.90	48.90	47.10	mm
D	76.00	0.50	0.50	76.50	75.50	mm
E	30.00	0.60	0.60	30.60	29.40	mm

Figure 2.25. Dimension of core of transformer from Ferroxcube data sheet.

Winding were placed according to [29]. To maximize the coupling co-efficient case C was chosen as fourth winding configuration is shorter in length. Winding were built as per specification of Litz wire gauge 8.

Ferroxcube 3C94 materials data were updated from data sheet in Ansys Maxwell to get realistic simulation of the transformer Figure 2.26, Figure 2.27.

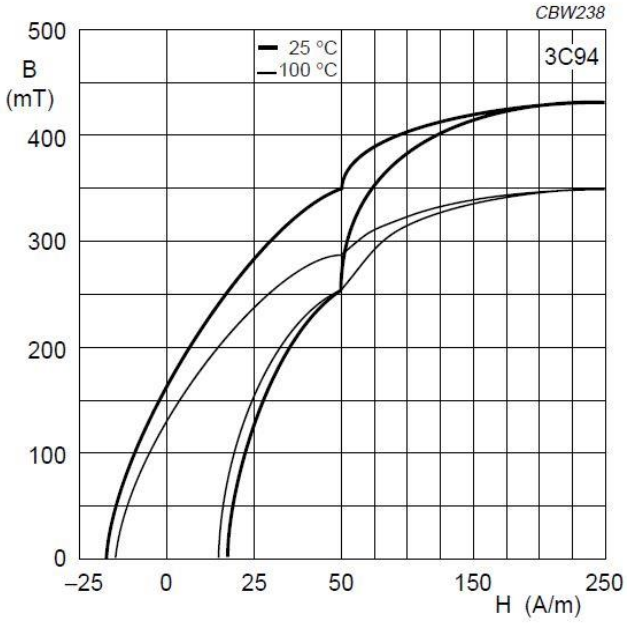

Figure 2.26. B-H loop from 3C94 Data Sheet.

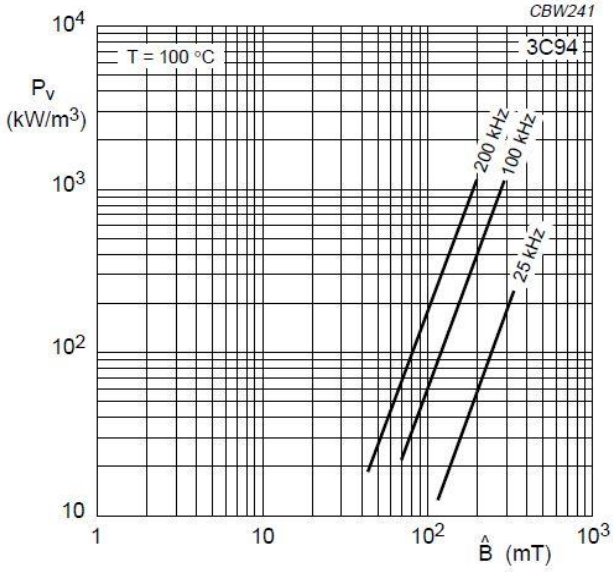

Figure 2.27. B-H loop from 3C94 Data Sheet.

All data were updated in Maxwell to get average value of the B-H curve with help of sheet scan feature in Maxwell. From the figure below, we can observe updated B-H curve and realize optimum B_{sat} in Maxwell.

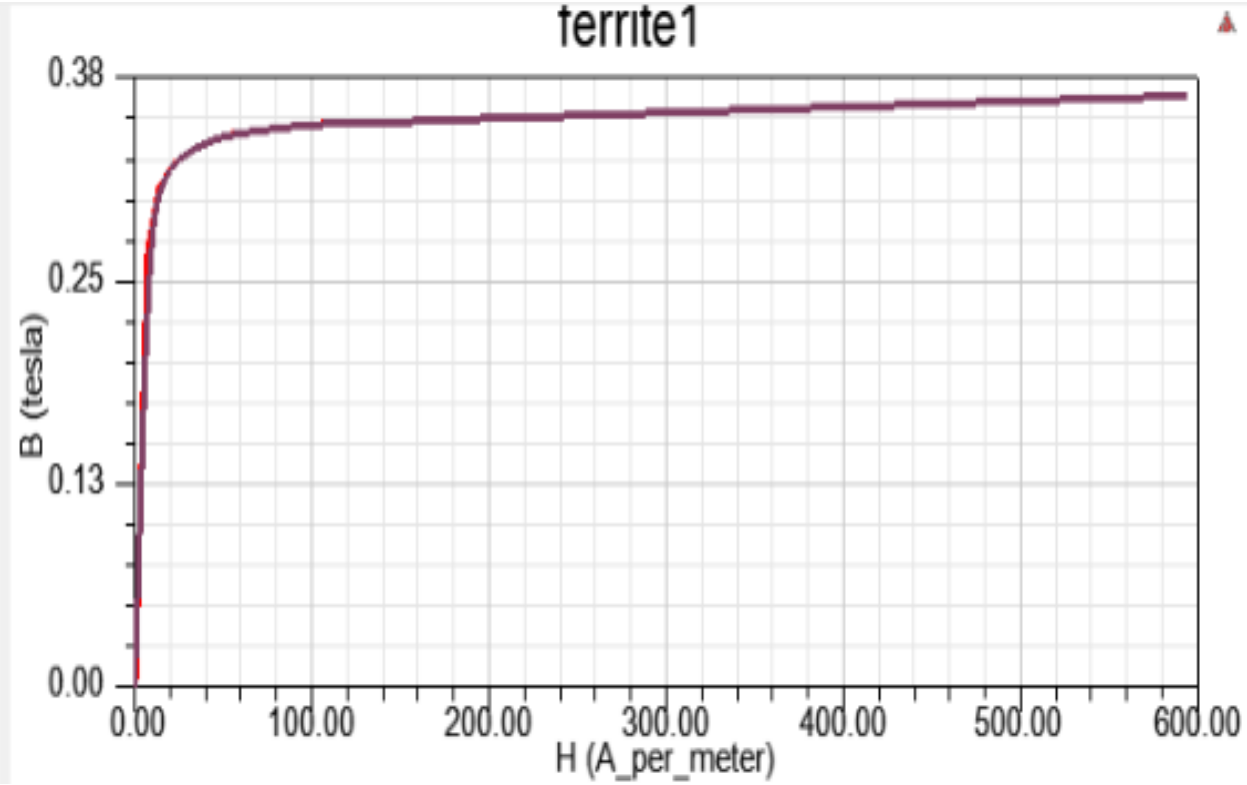

Figure 2.28. Updated B-H curve in Maxwell.

The transformer that was built in Ansys Maxwell according to specification, was transferred to Ansys Simplorer for Maxwell-Simplorer co-simulation. Then the current for different voltage level were extracted from Simplorer for winding excitation in Maxwell Transient Solver. The switching frequency of the convereter was 50000 Hz for all set of simulation.

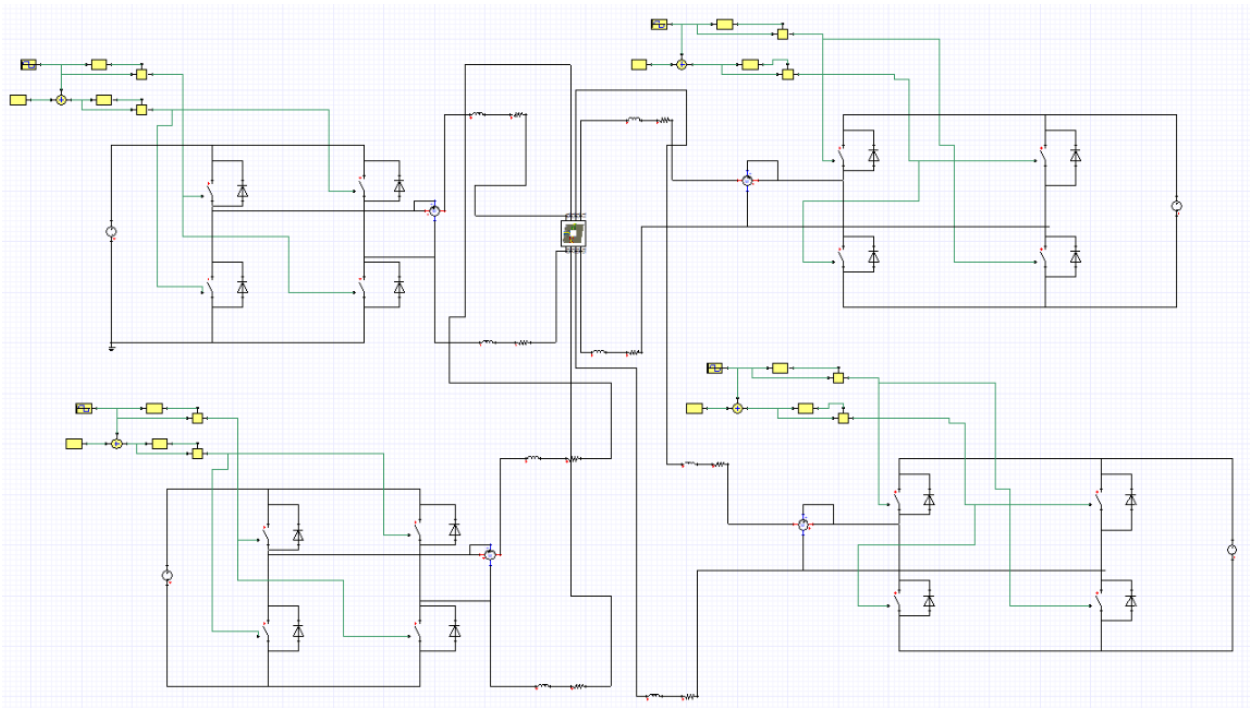

Figure 2.29. Maxwell-Simplorer co-simulation.

4.3.2 Case#1: 100 V applied to four ports

For this simulation 100 V was applied to four ports to extract excitation current for transformer in Maxwell. In open loop control, the phase shift for the converter were $\varphi_1 = 0°, \varphi_2 = 35°, \varphi_3 = 45°, \varphi_4 = 55°$, duty cycle of gate pulses was 50% and switching frequency 50000 Hz.

4.3.2.1 Excitation current for different windings (100V)

Excitation current of four windings were extracted from Ansys Simplorer that are given below.

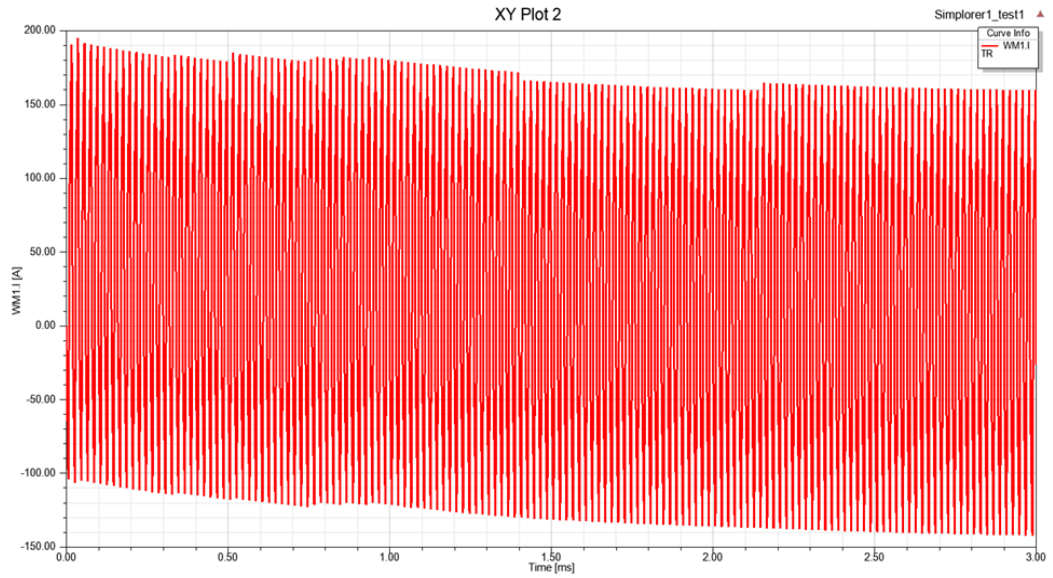

Figure 2.30. Excitation current extracted from winding 1 (100V).

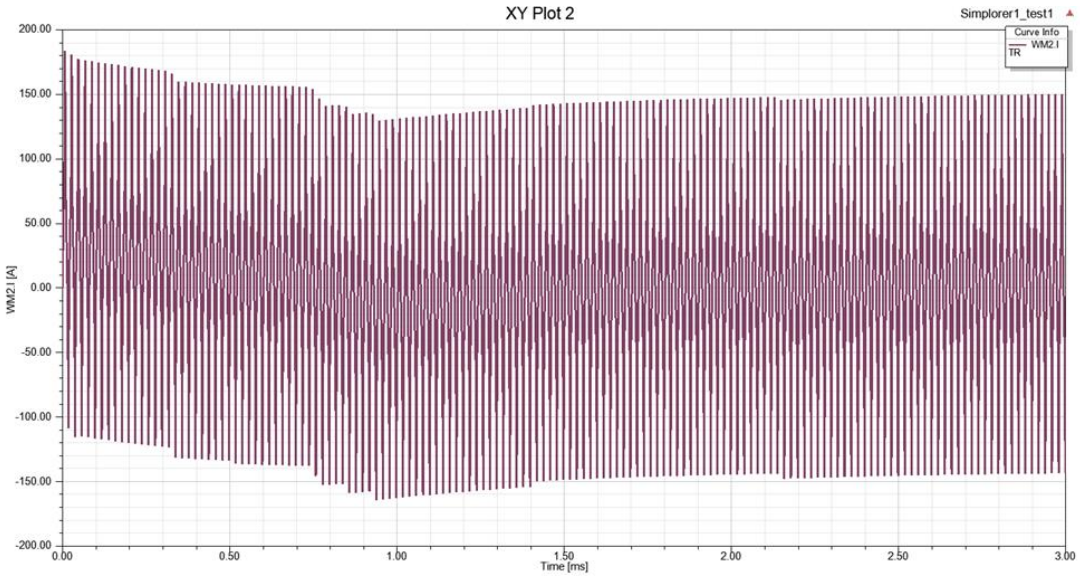

Figure 2.31. Excitation current extracted from winding 2 (100V).

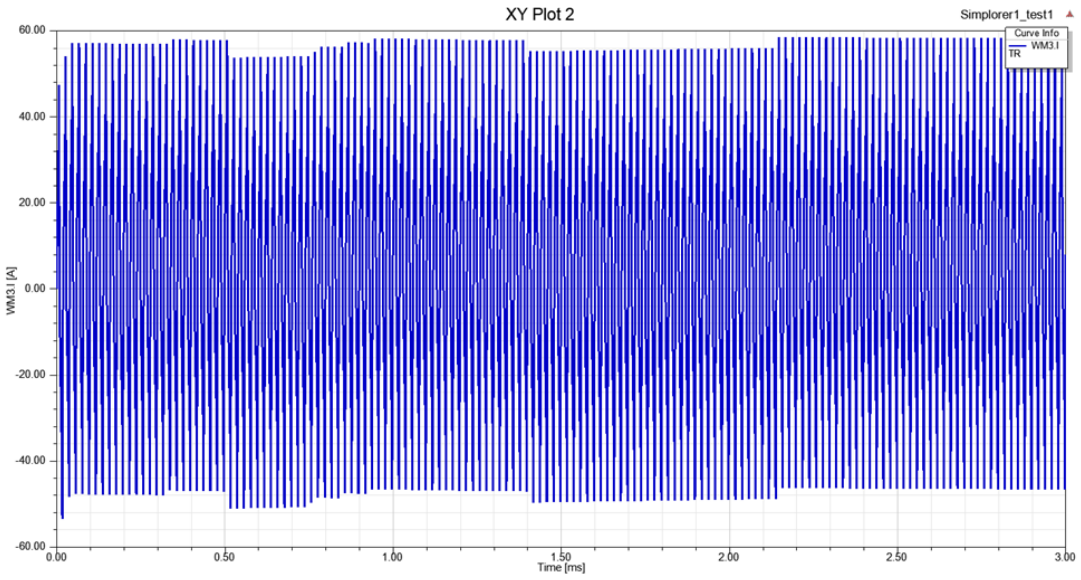

Figure 2.32. Excitation current extracted from winding 3 (100V).

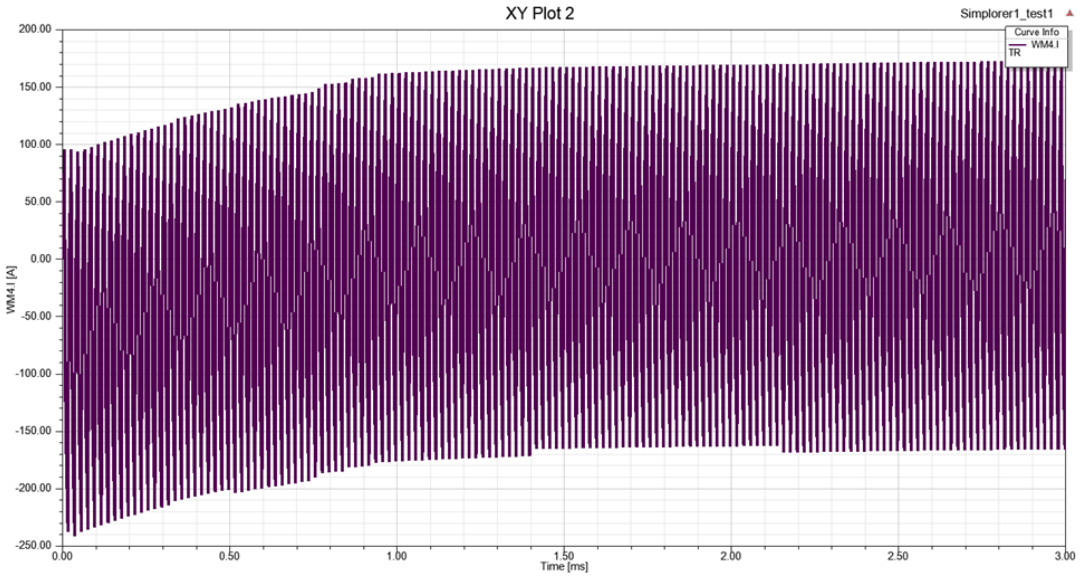

Figure 2.33. Excitation current extracted from winding 4 (100V).

Core loss was evaluated in Maxwell transient simulation which can be observed from Figure.14 below. Average core loss for whole operating period was 14.7641 mW.

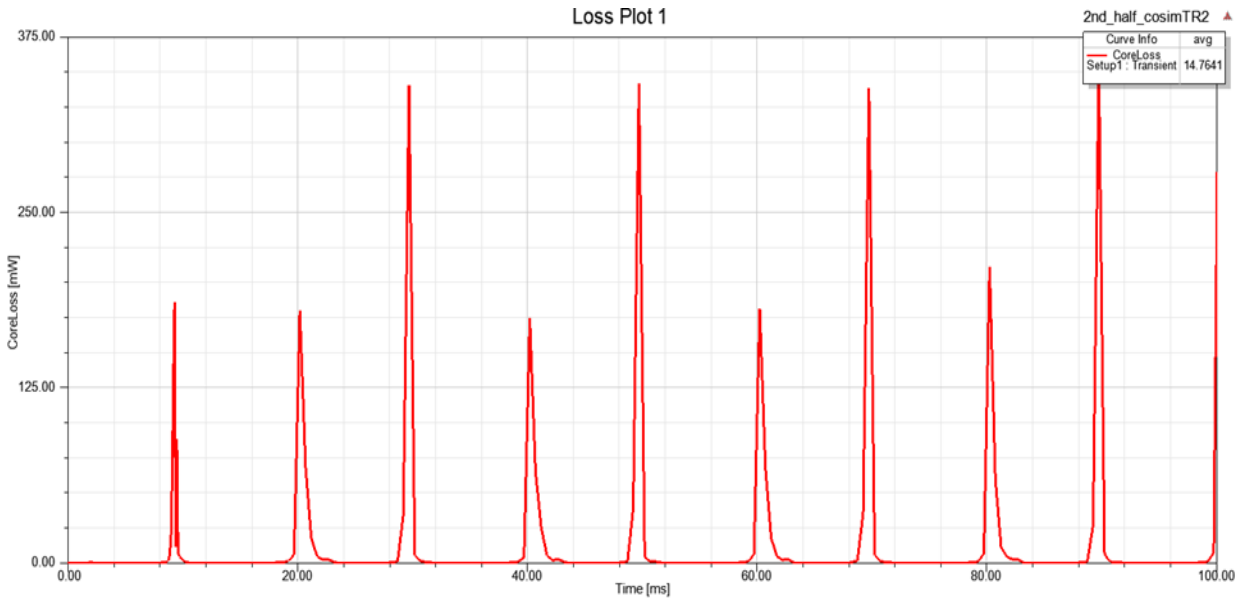

Figure 2.34. Core loss for applied 100 V in four ports.

We can also observe from below figures that flux linkage Vs input current (excitation current) is taking the shape of B-H curve as we know flux linkage is associated with flux density and excitation current is associated with magnetic field strength.

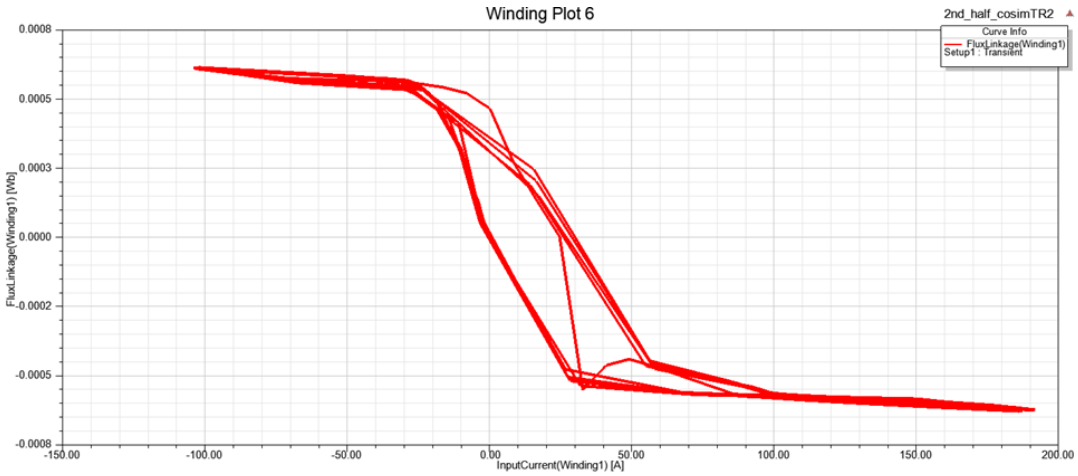

Figure 2.35. Flux linkage-input current for winding 1(100V).

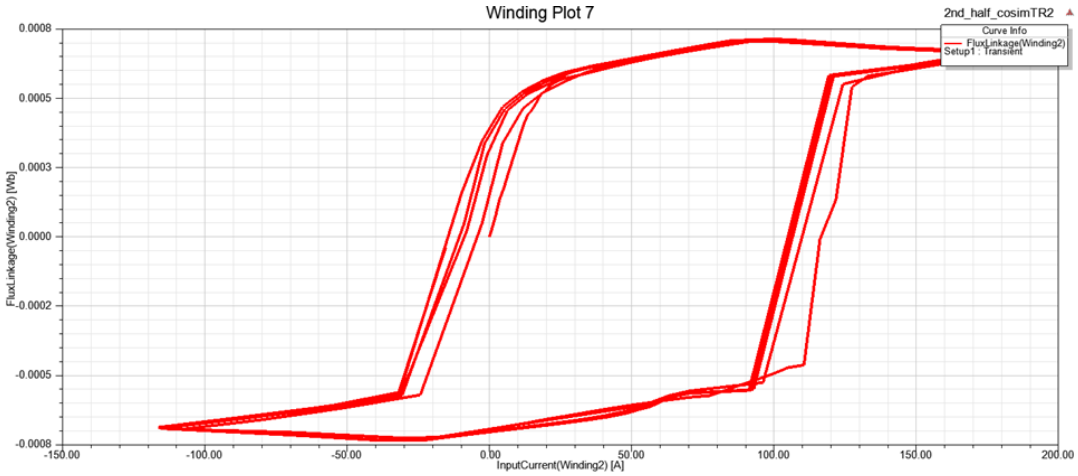

Figure 2.36. Flux linkage-input current for winding 2 (100V).

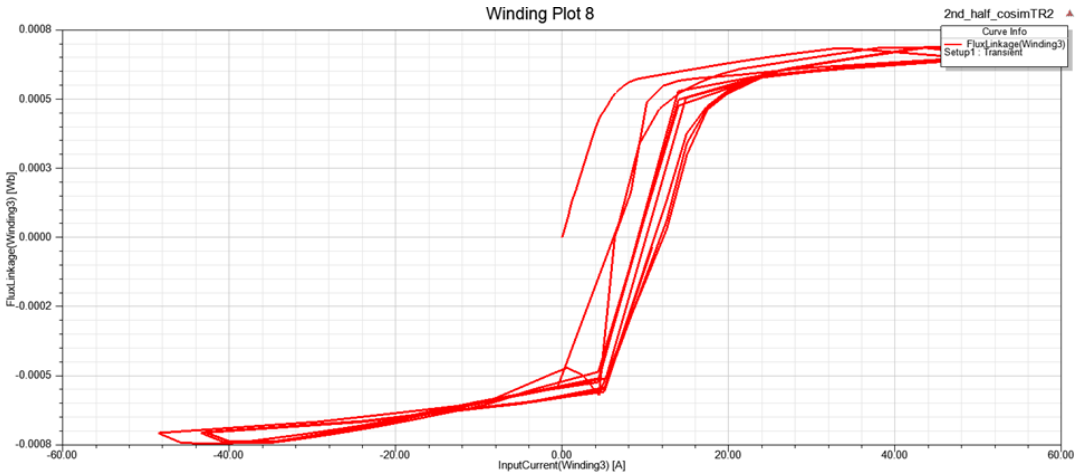

Figure 2.37. Flux linkage-input current for winding 3 (100V).

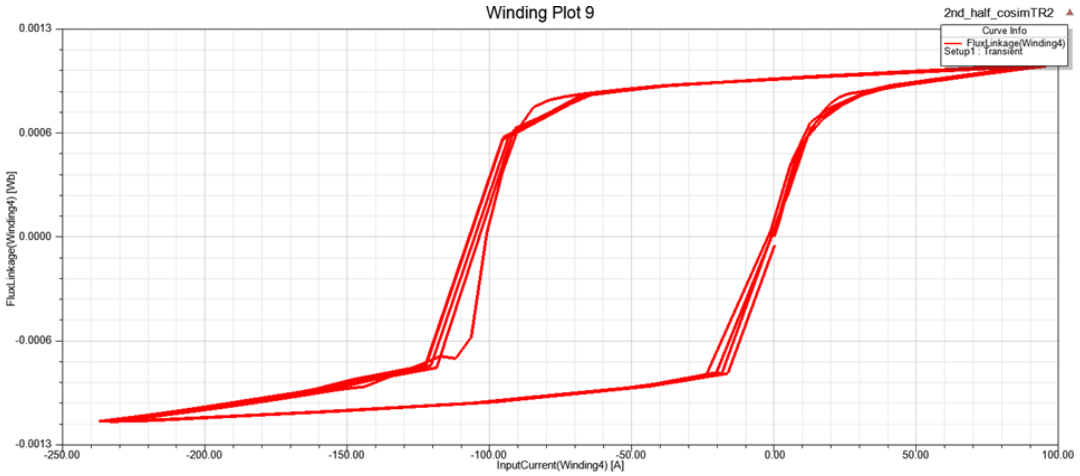

Figure 2.38. Flux linkage-input current for winding 4 (100V).

Then flux density for this core was evaluated. As Maxwell was updated with average B-H curve from data sheet, B_{sat} was 0.38 Tesla for this case.

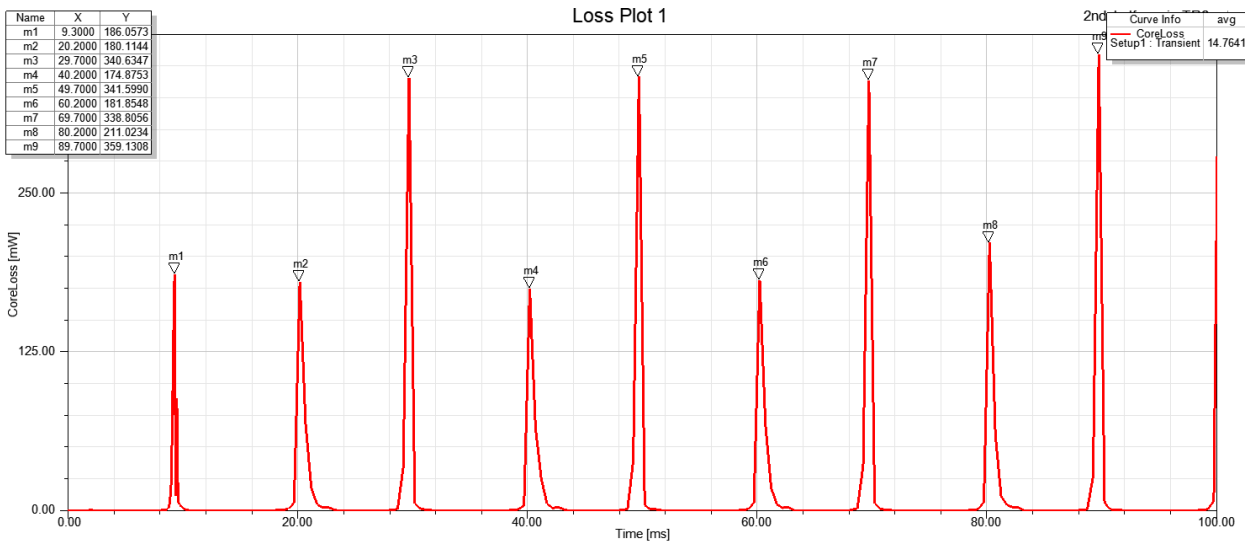

Figure 2.39. Core loss in different time frame (100V).

Flux density:

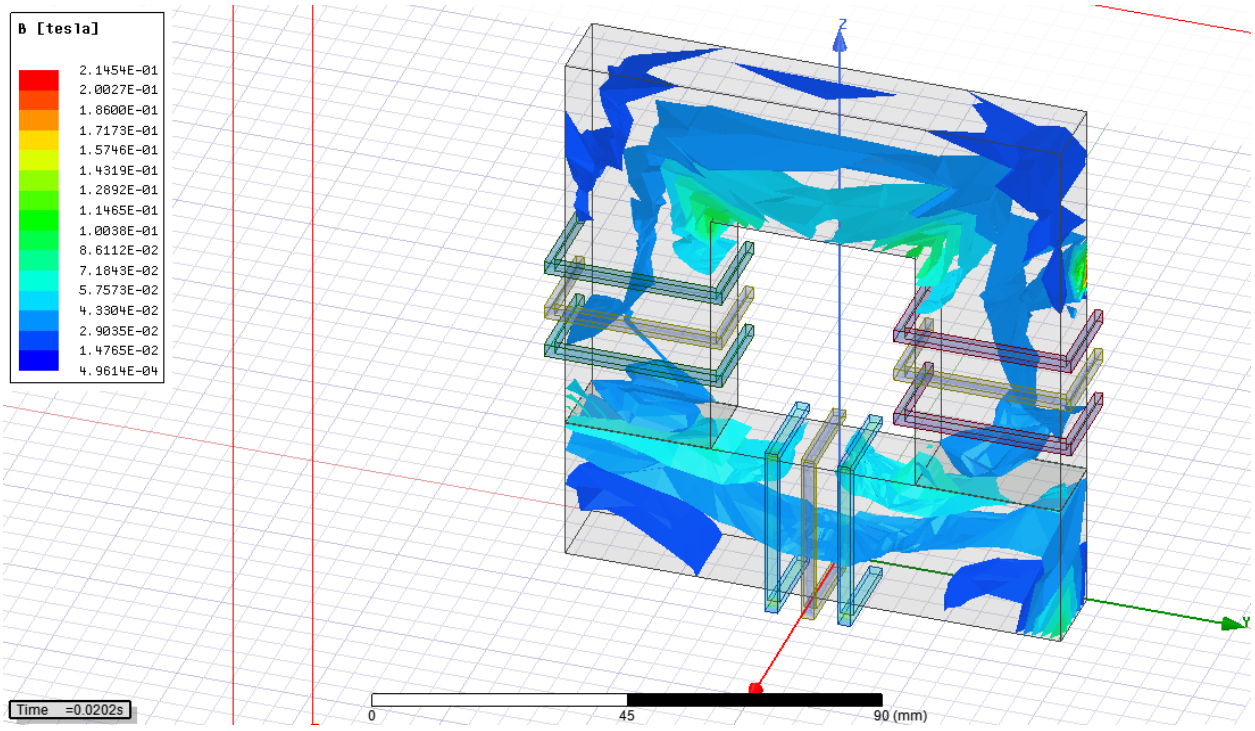

Figure 2.40. Flux density in 0.0202 sec (100V).

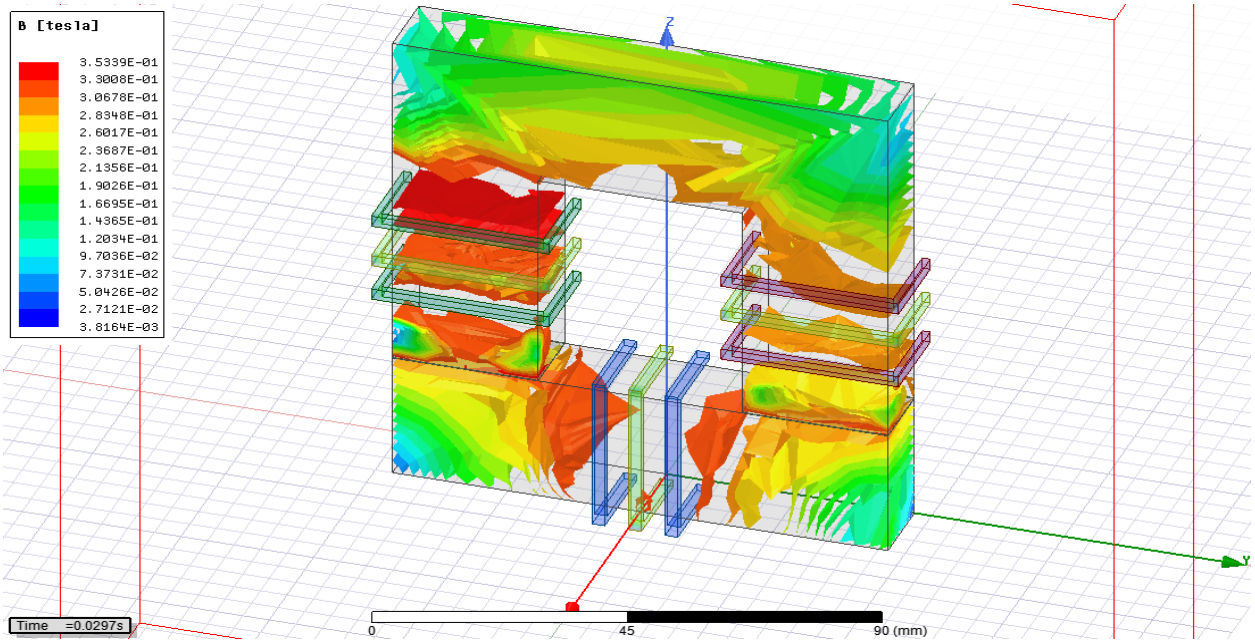

Figure 2.41. Flux density in 0.0297 sec (100V).

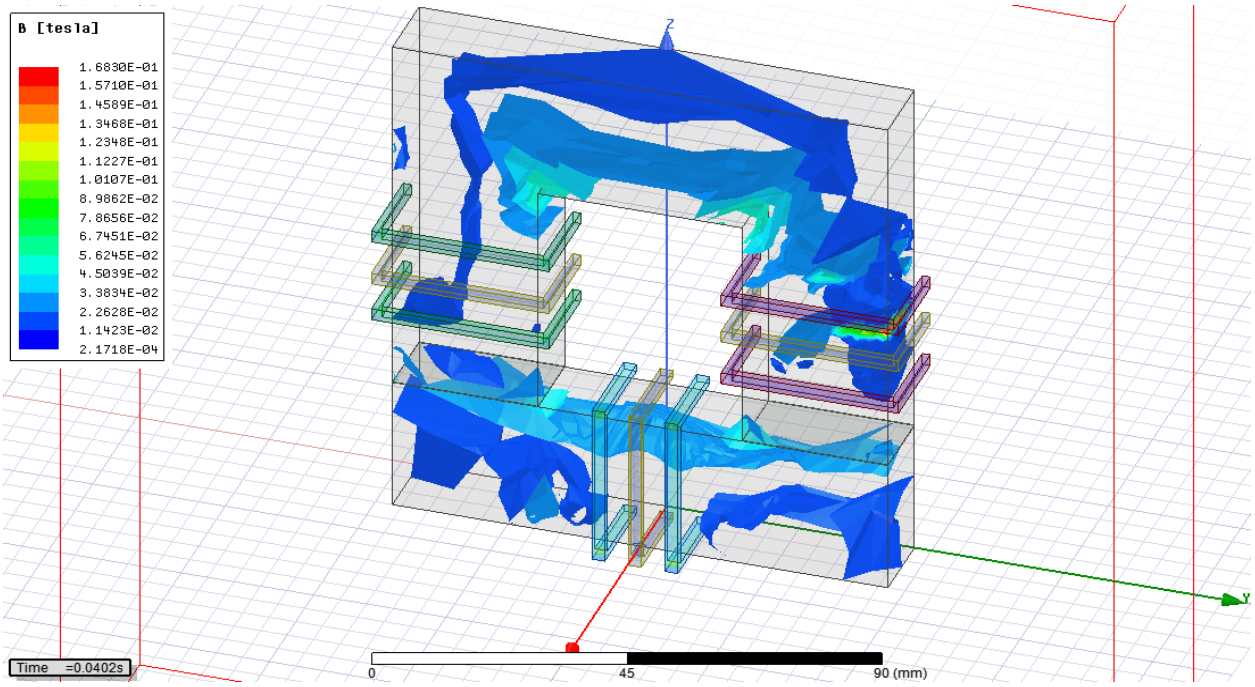

Figure 2.42. Flux density in 0.0402 sec (100V).

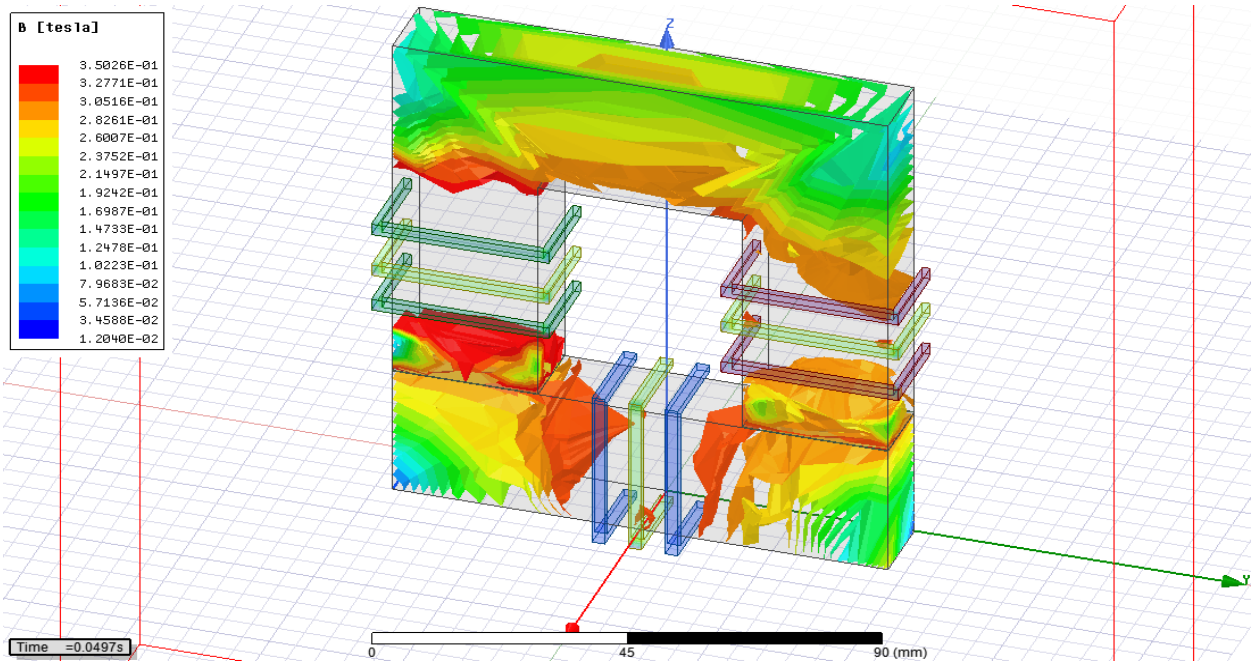

Figure 2.43. Flux density in 0.0497 sec (100V).

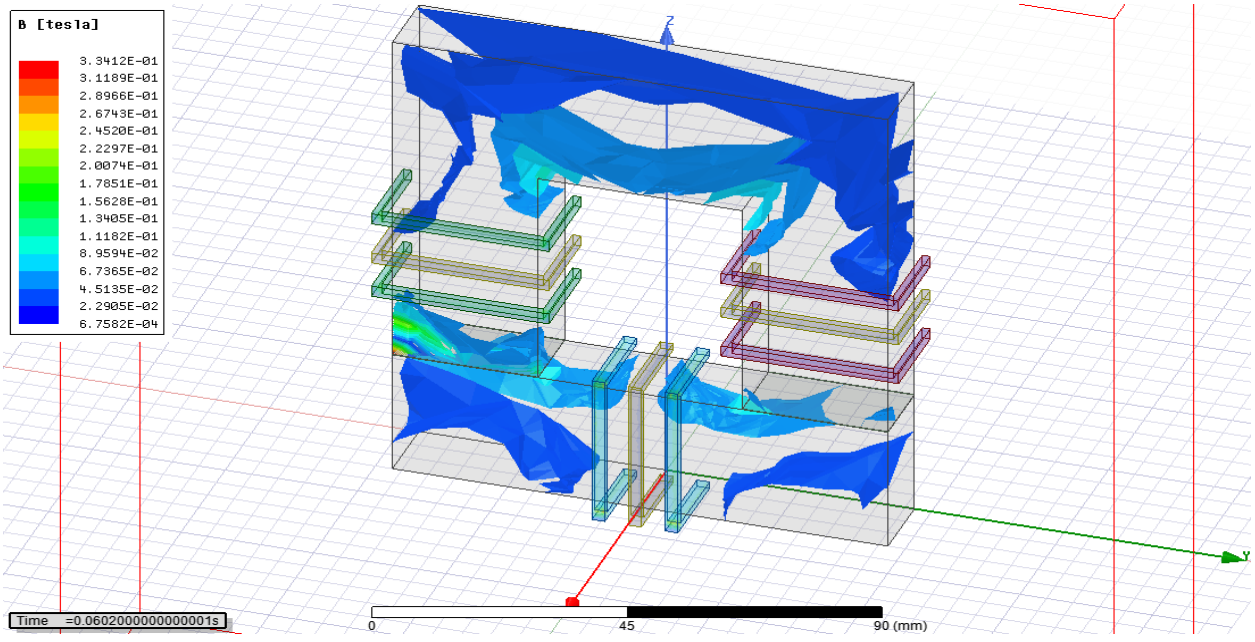

Figure 2.44. Flux density in 0.0602 sec (100V).

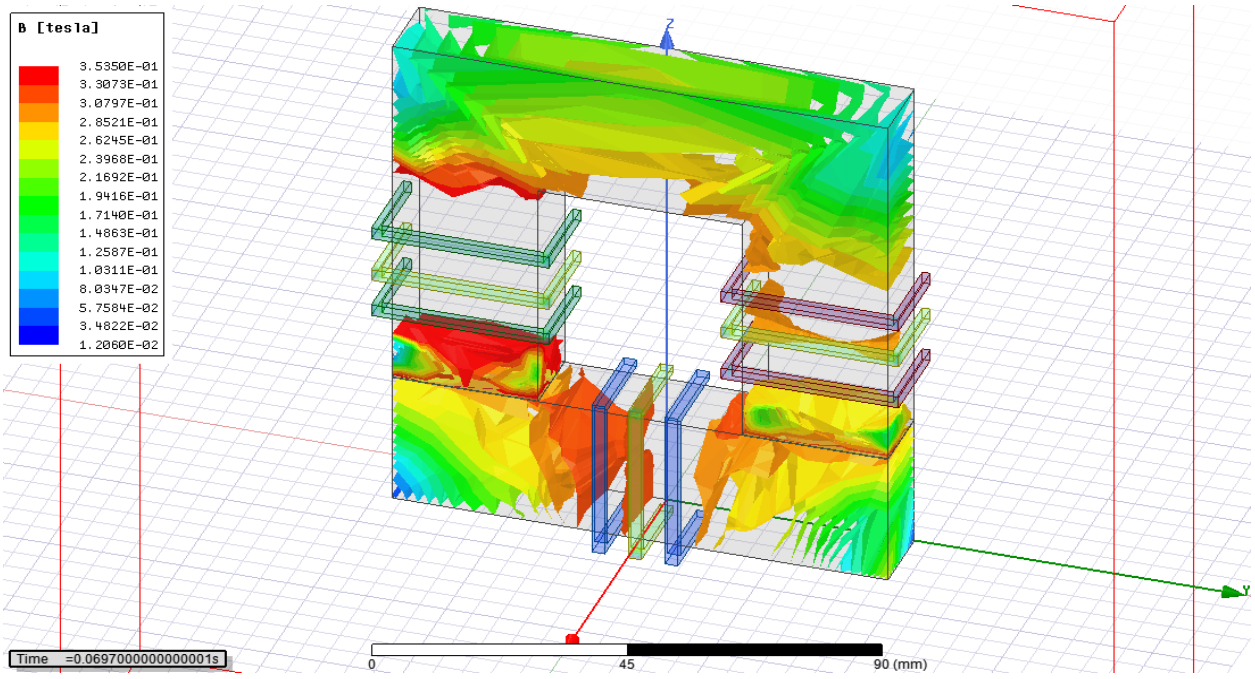

Figure 2.45. Flux density in 0.0697 sec (100V).

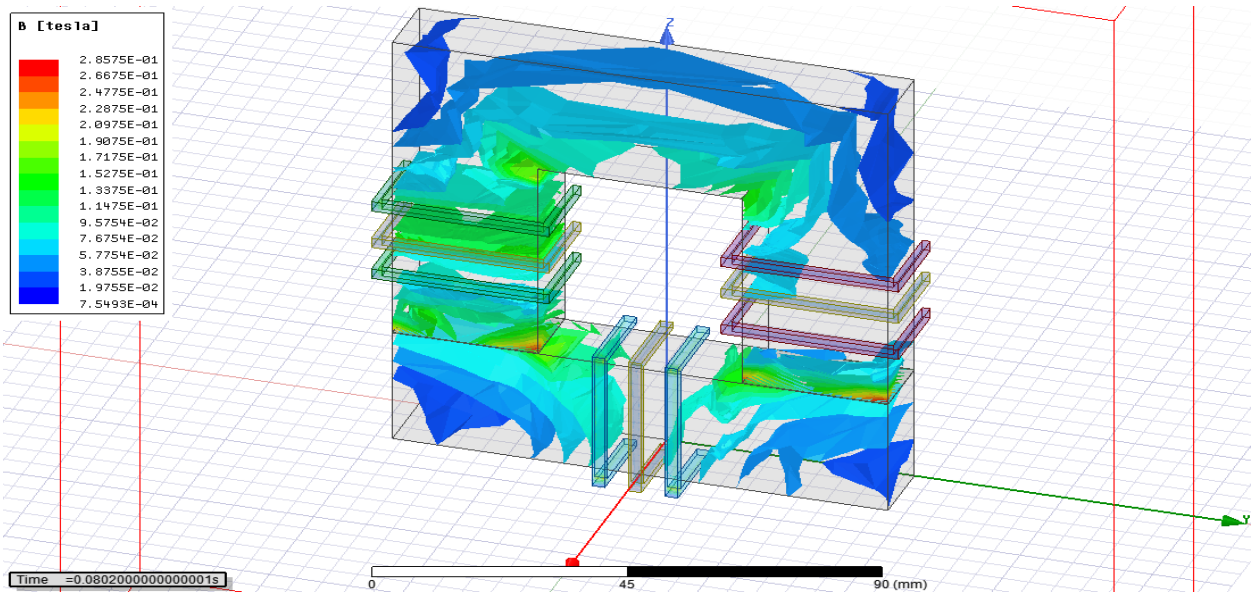

Figure 2.46. Flux density in 0.0802 sec (100V).

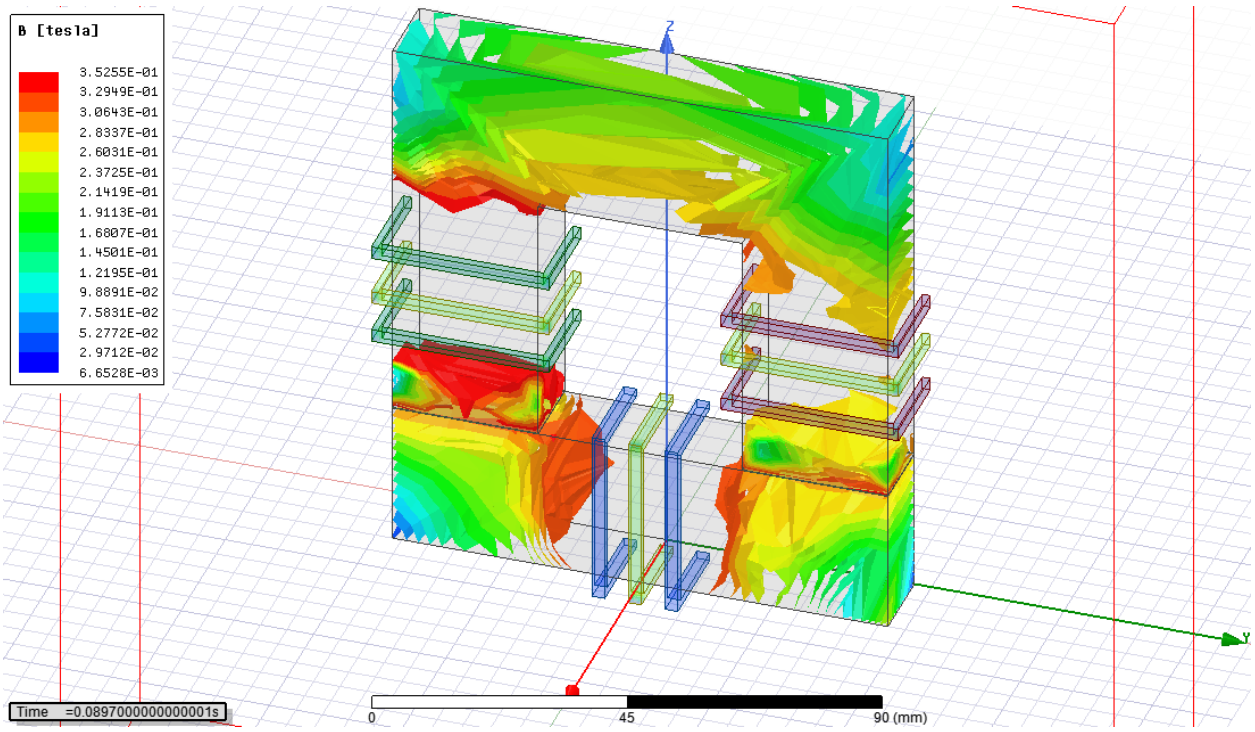

Figure 2.47. Flux density in 0.0897 sec (100V).

From above simulation for Case#1 it was observed that the flux density was below than B_{sat}. Average core loss was 14.7641 mW which is within expected level.

4.3.3 Case#2: 2400 V applied to four ports

Here in Case#2 2400 V was applied in four ports to extract excitation current from Simplorer for transformer in Ansys Maxwell. In open loop control, again the phase shift for the converter were $\varphi_1 = 0°, \varphi_2 = 35°, \varphi_3 = 45°, \varphi_4 = 55°$, duty cycle of gate pulses was 50% and switching frequency 50000 Hz.

4.3.3.1 Excitation current for different windings (2400V)

Excitation current of four windings were extracted from Ansys Simplorer that are given below.

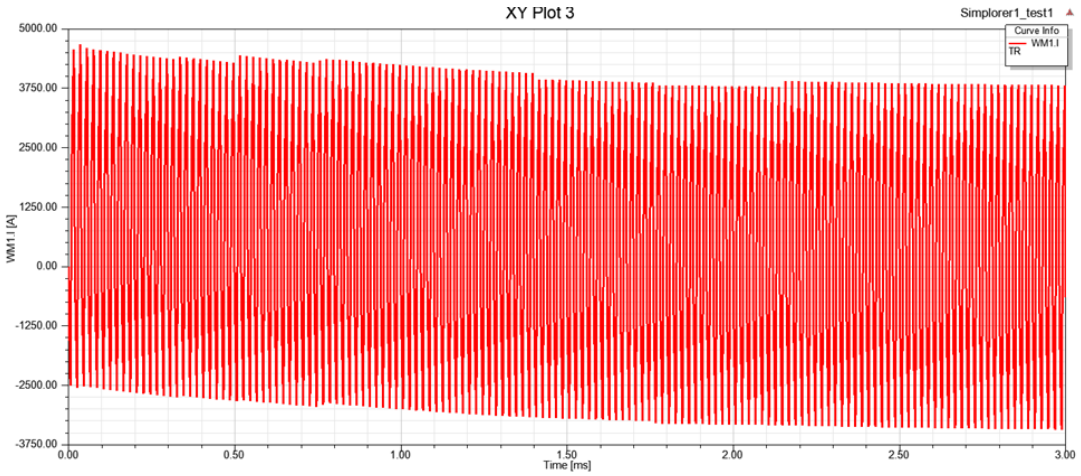

Figure 2.48. Excitation current extracted from winding 1 (2400V).

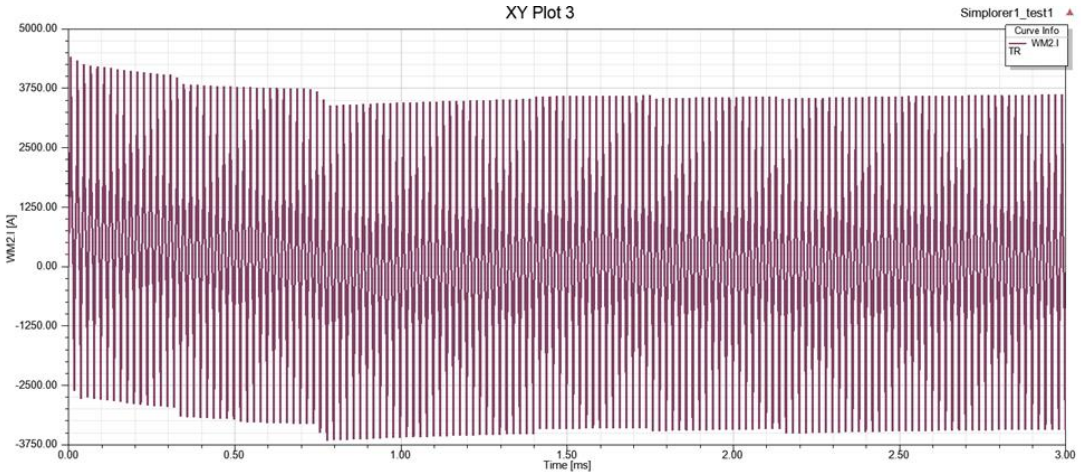

Figure 2.49. Excitation current extracted from winding 2 (2400V).

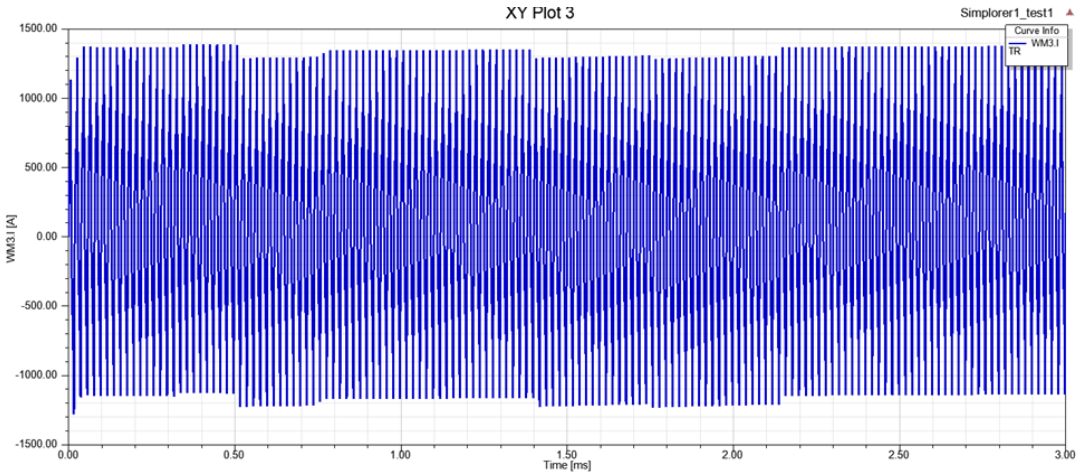

Figure 2.50. Excitation current extracted from winding 3 (2400V).

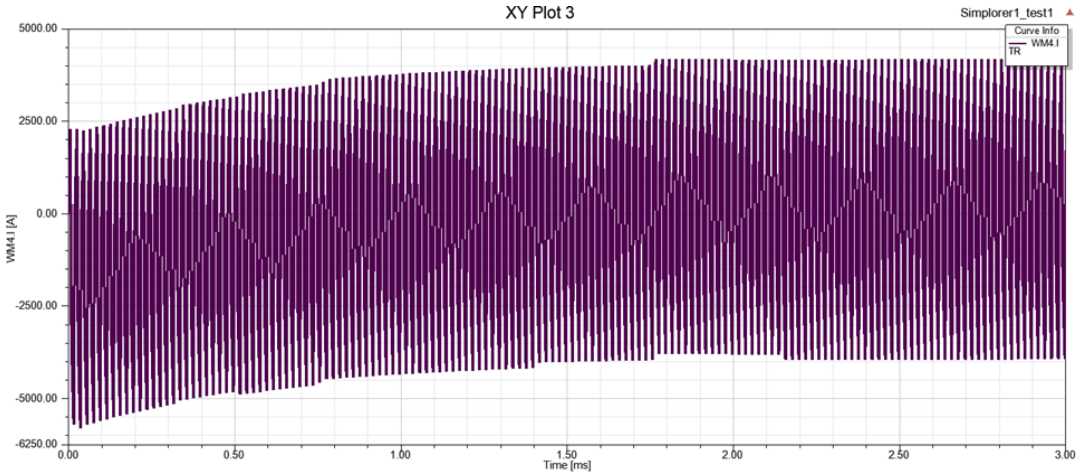

Figure 2.51. Excitation current extracted from winding 4 (2400V).

Core loss was evaluated for 2400V in Maxwell transient simulation which can be observed from figure below. Average core loss for whole operating period was 0.6725 W.

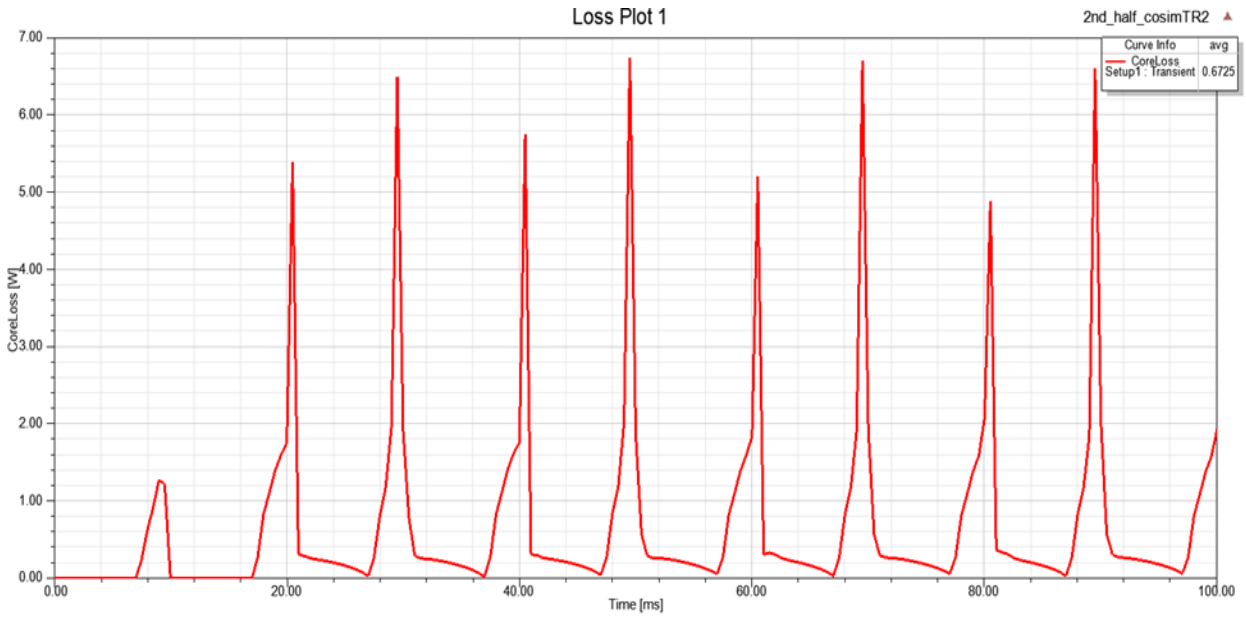

Figure 2.52. Core loss for applied 2400V in four ports.

Here for applied 2400V, it can be observed from below figure that flux linkage Vs input current (excitation current) is taking the shape of B-H curve as we know flux linkage is associated with flux density and excitation current is associated with magnetic field strength.

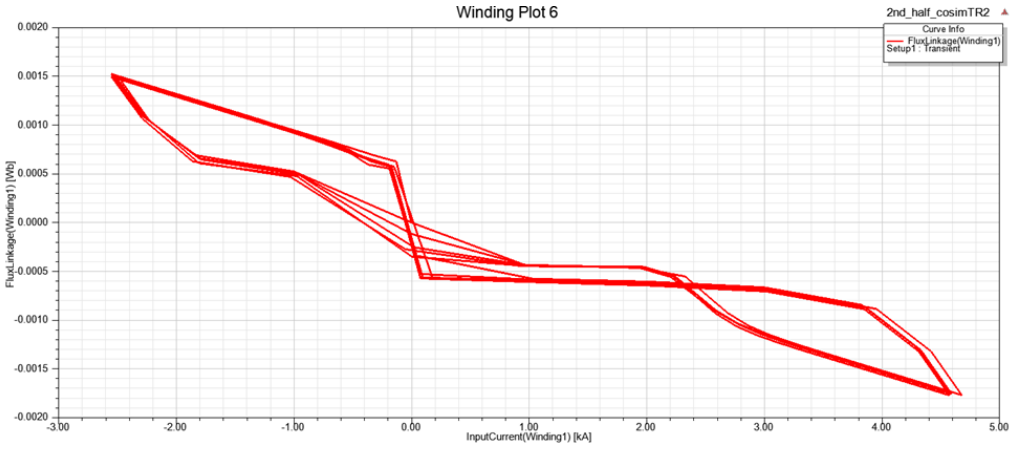

Figure 2.53. Flux linkage-input current for winding 1 (2400V).

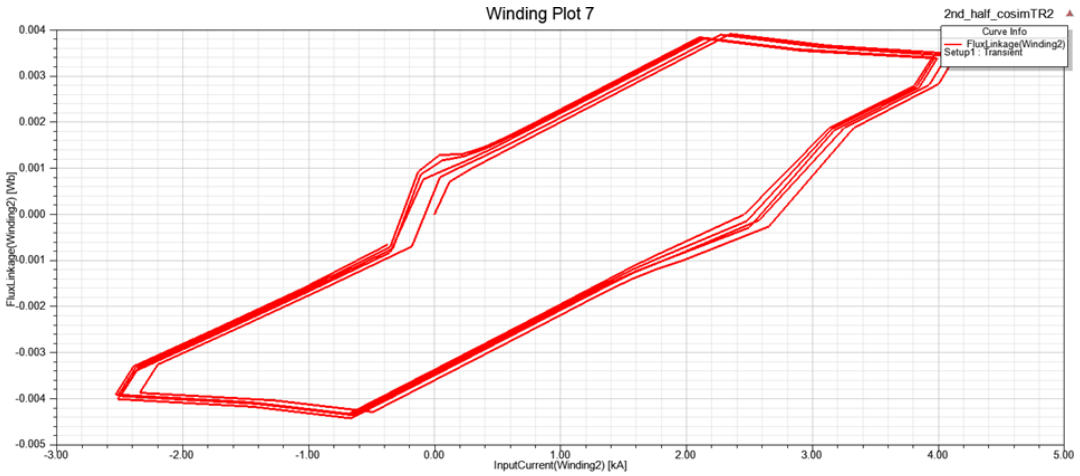

Figure 2.54. Flux linkage-input current for winding 2 (2400V).

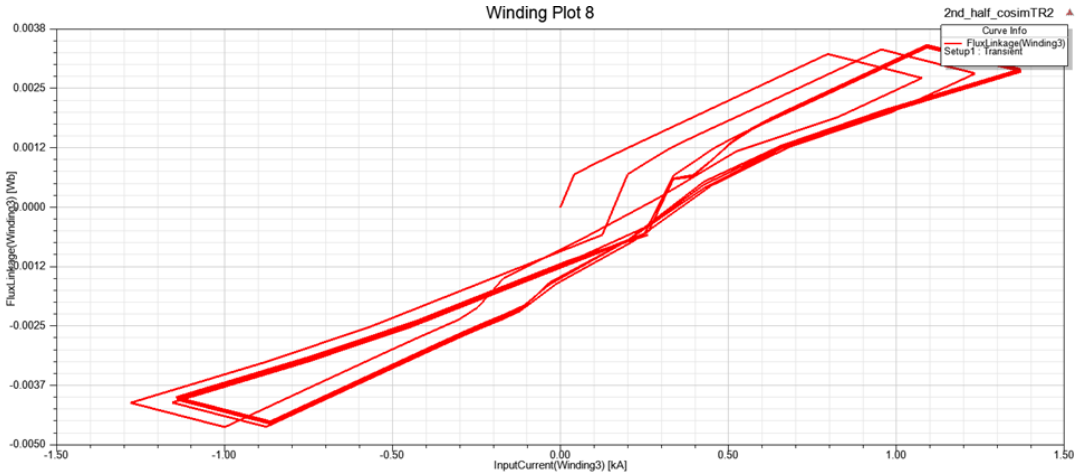

Figure 2.55. Flux linkage-input current for winding 3 (2400V).

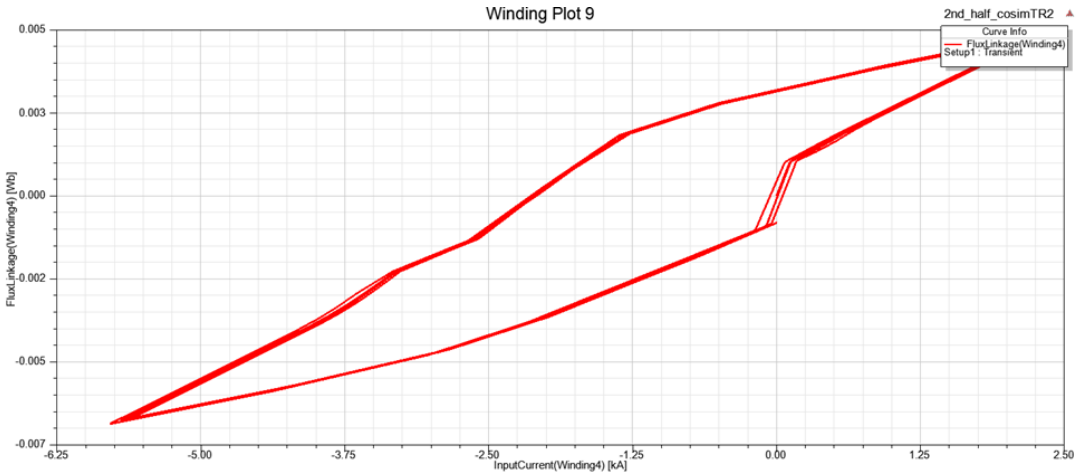

Figure 2.56. Flux linkage-input current for winding 4 (2400V).

Then flux density for this core was evaluated. As Maxwell was updated with average B-H curve from data sheet, B_{sat} was 0.38 Tesla for this case.

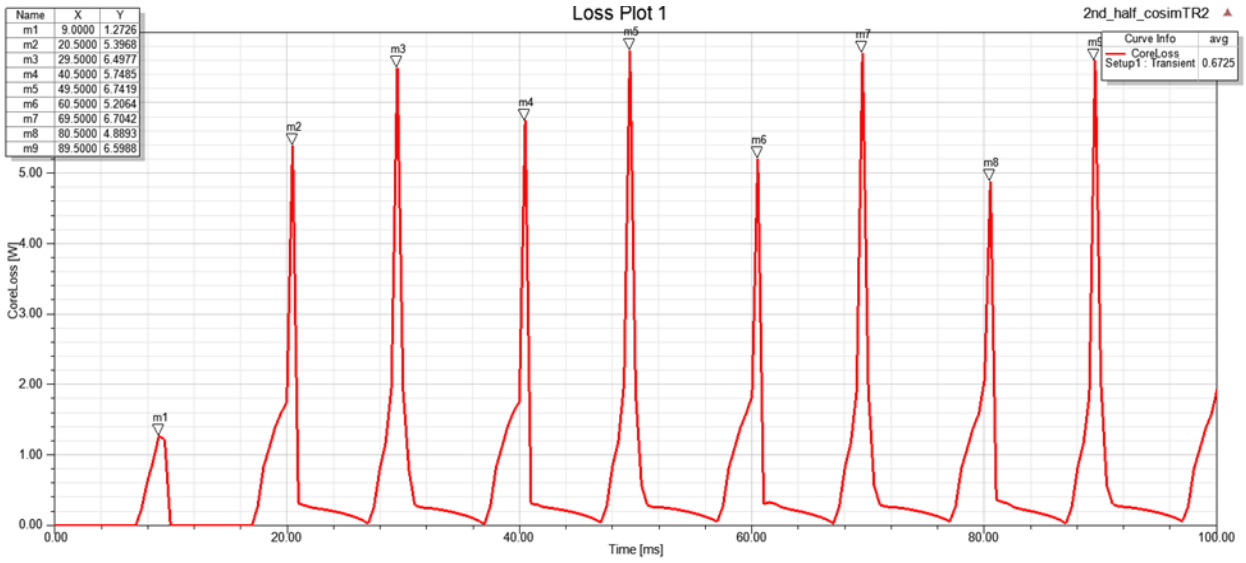

Figure 2.57. Time evaluation for peak core loss (2400 V).

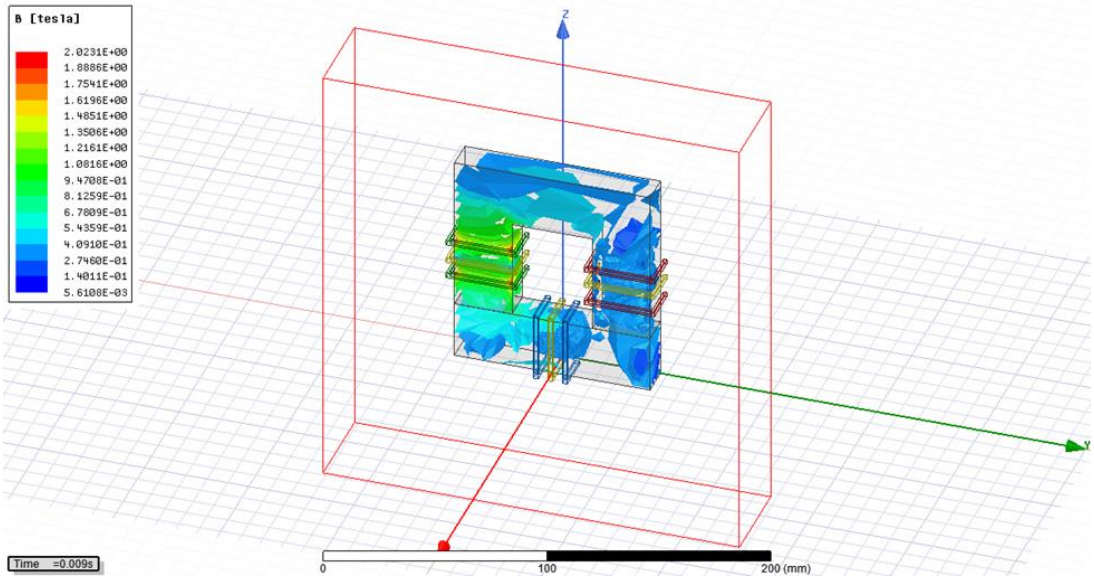

Figure 2.58. Flux density in 0.009 sec (2400V).

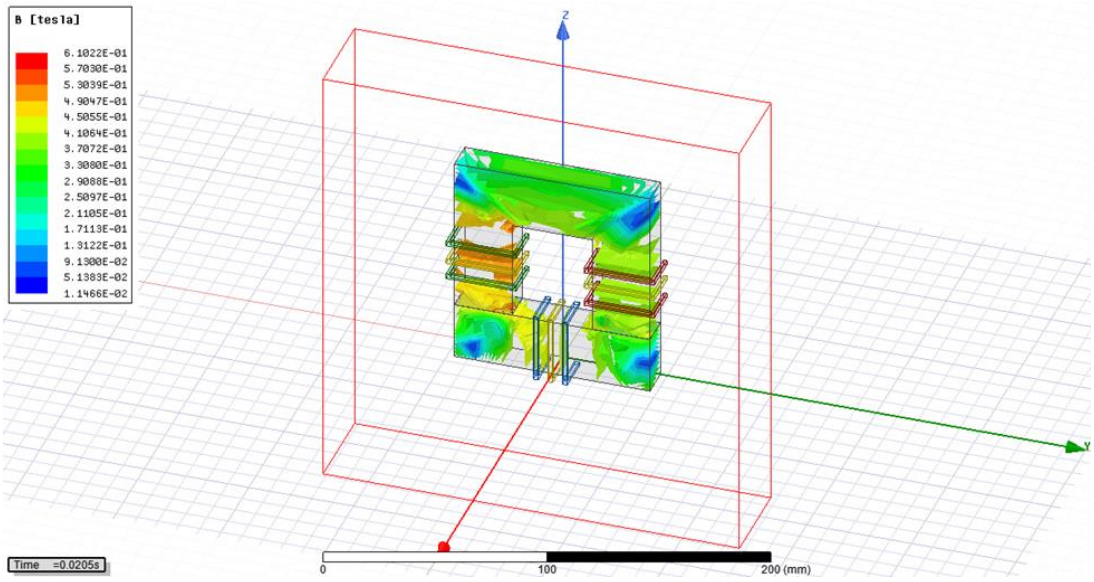

Figure 2.59. Flux density in 0.0205 sec (2400V).

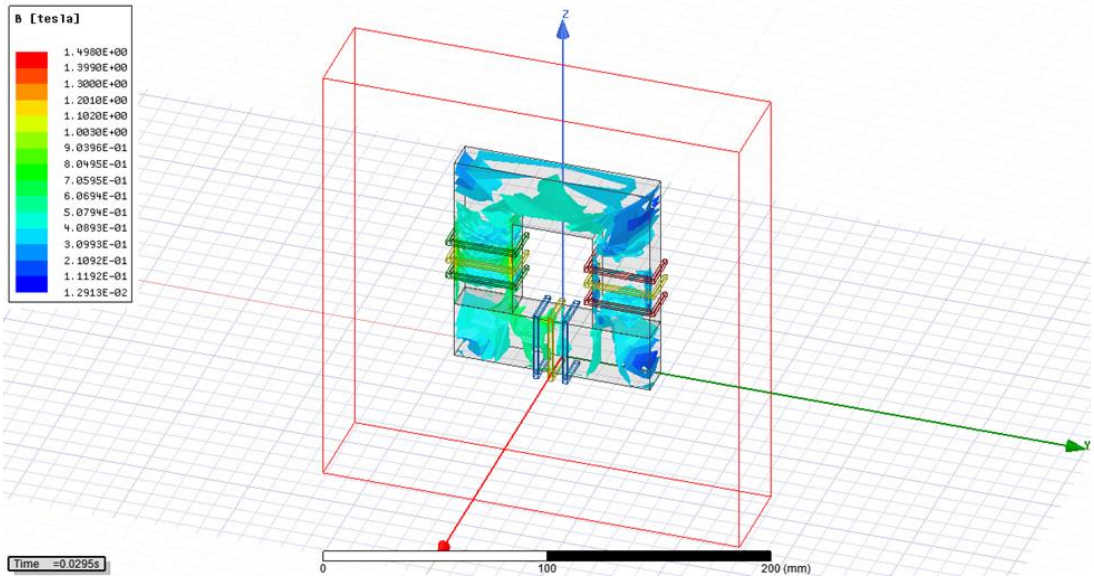

Figure 2.60. Flux density in 0.0295 sec (2400V).

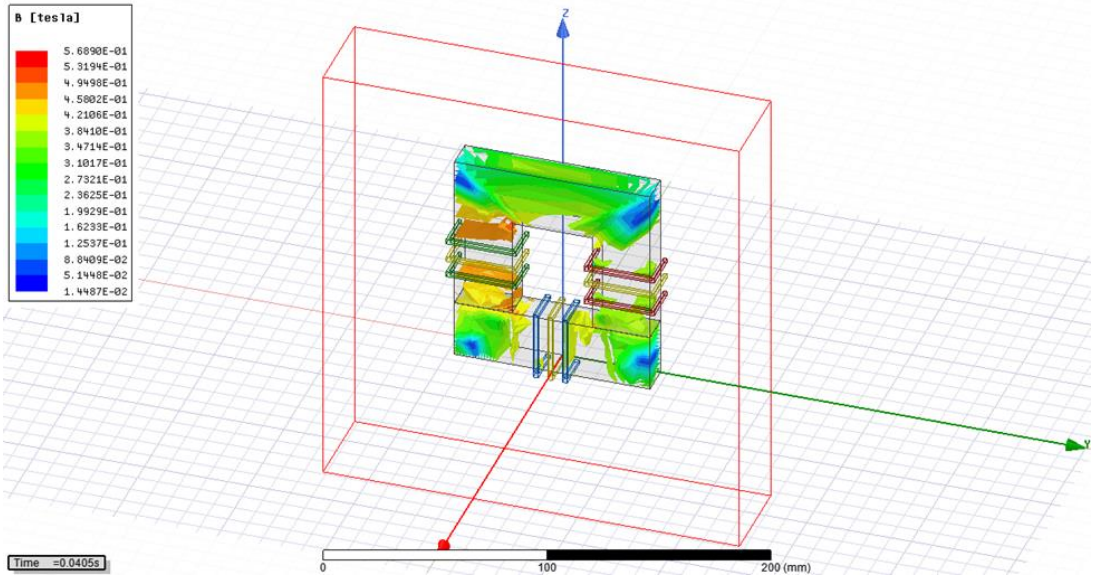

Figure 2.61. Flux density in 0.0405 sec (2400V).

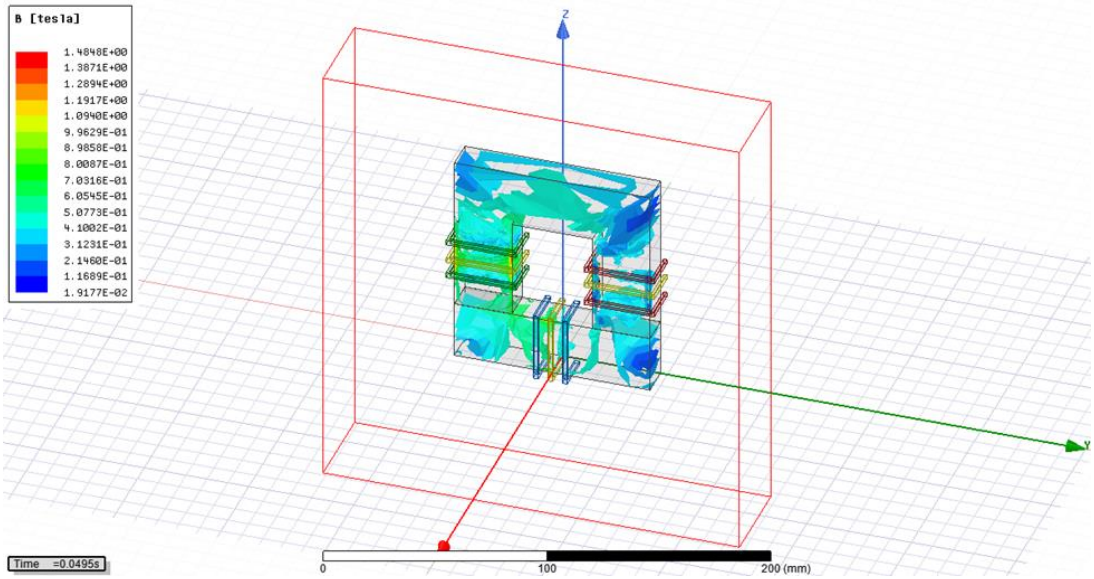

Figure 2.62. Flux density in 0.0495 sec (2400V).

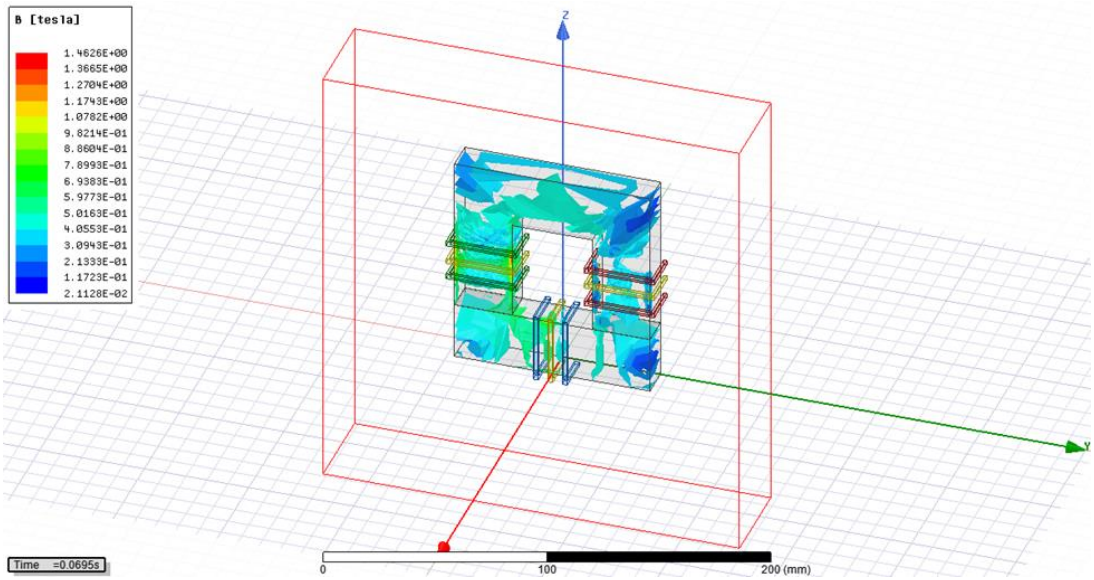

Figure 2.63. Flux density in 0.0695 sec (2400V).

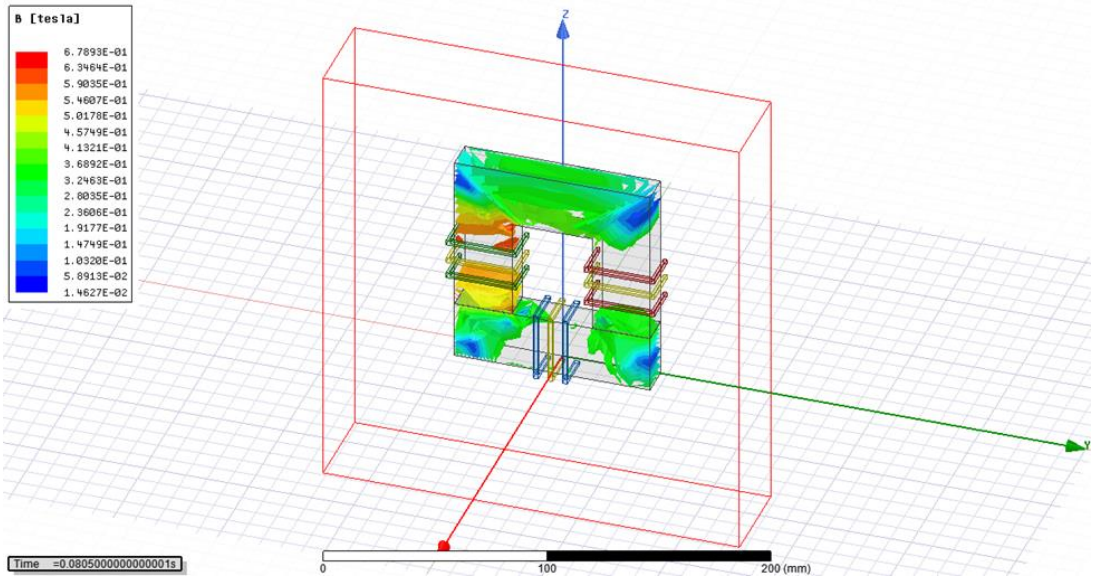

Figure 2.64. Flux density in 0.08 sec (2400V).

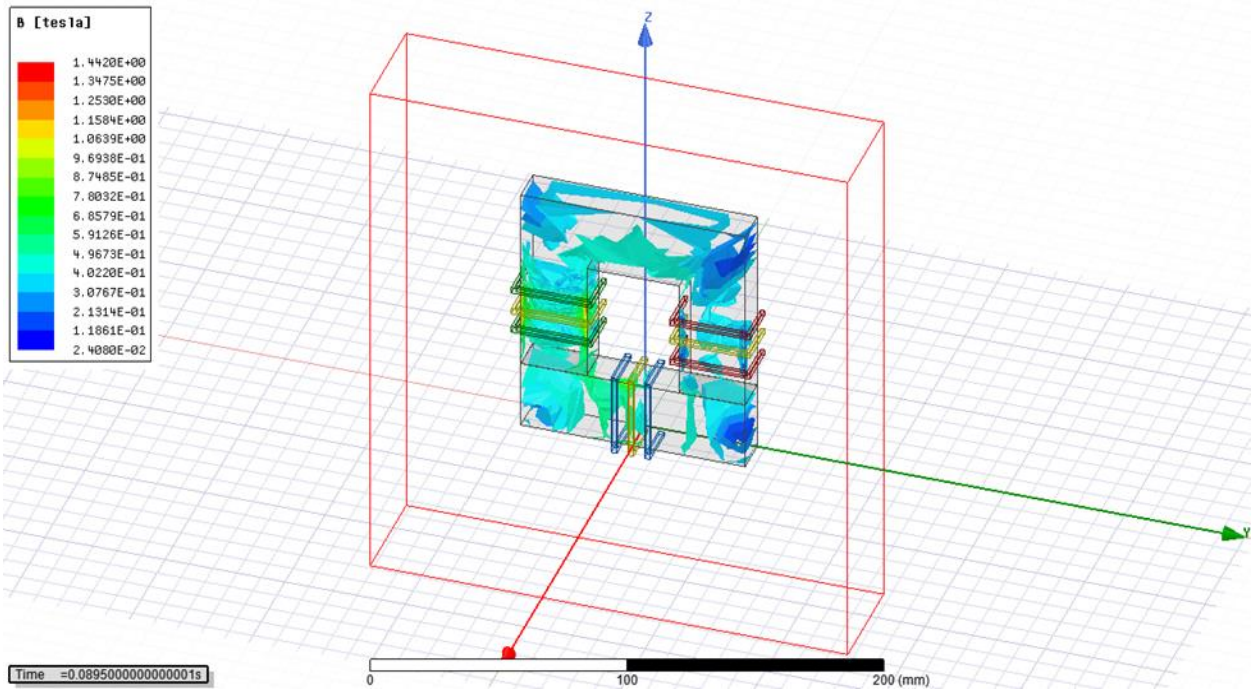

Figure 2.65. Flux density in 0.0895 sec (2400V).

From above simulation in Case#2 it was evaluated that the flux density was at the level of almost crossing B_{sat}. Average core loss was 0.06725 W which is within expected level.

4.3.4 Case#3: 13800 V applied to four ports

Here in Case#3 13800 V was applied in four ports to extract excitation current from Simplorer for transformer in Ansys Maxwell. In open loop control, again the phase shift for the converter were $\varphi_1 = 0°, \varphi_2 = 35°, \varphi_3 = 45°, \varphi_4 = 55°$, duty cycle of gate pulses was 50% and switching frequency 50000 Hz.

4.3.4.1 Excitation current for different windings (13800V)

Excitation current of four windings were extracted from Ansys Simplorer that are given below.

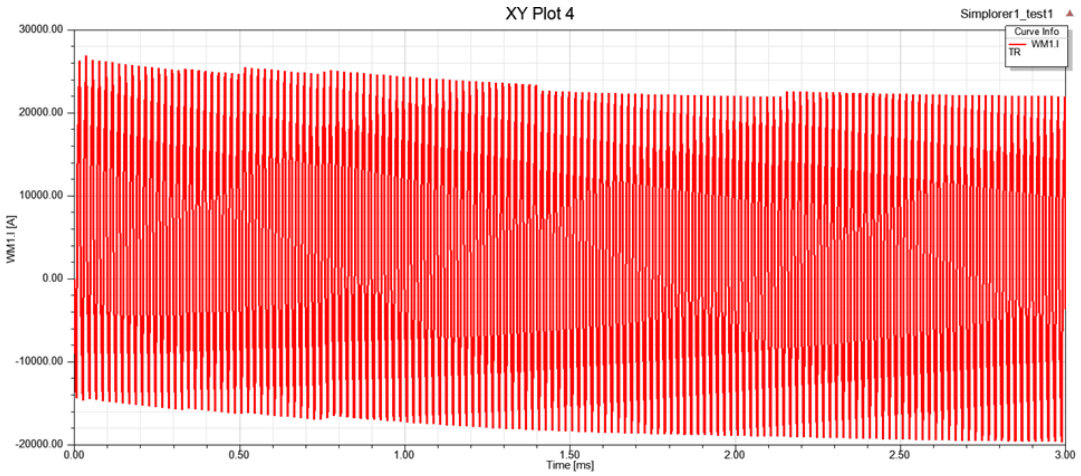

Figure 2.66. Excitation current extracted from winding 1 (13800V).

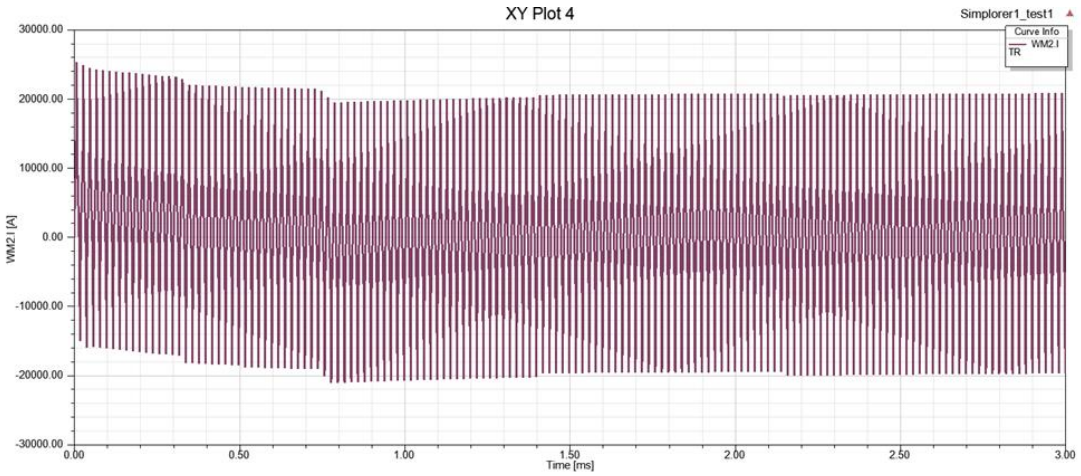

Figure 2.67. Excitation current extracted from winding 2 (13800V).

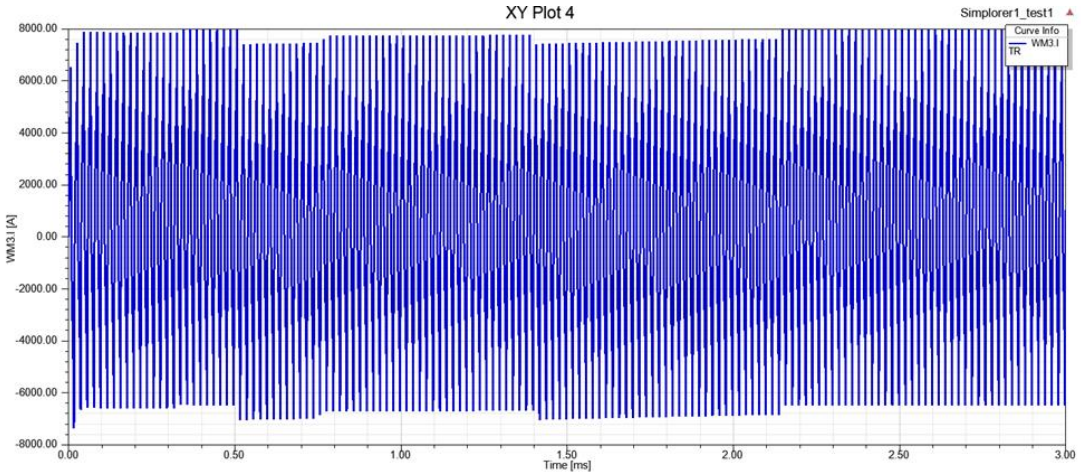

Figure 2.68. Excitation current extracted from winding 3 (13800V).

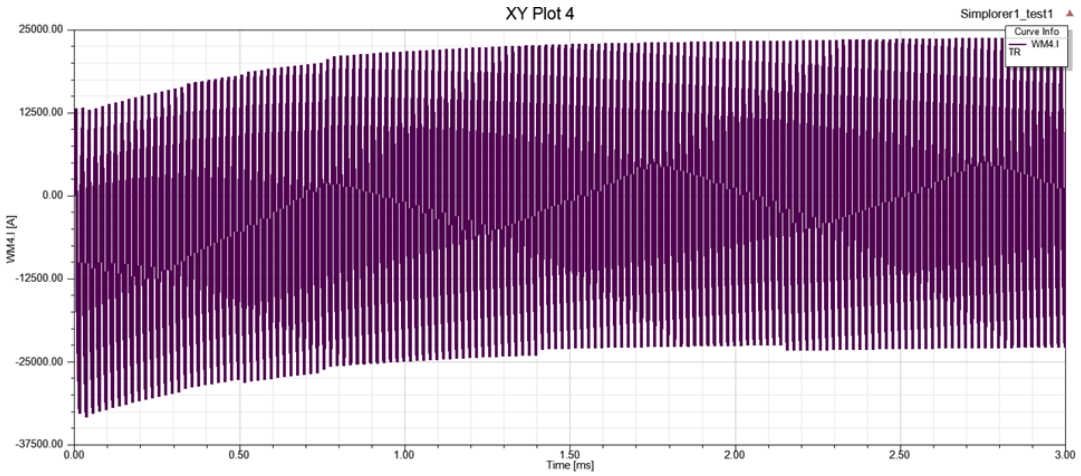

Figure 2.69. Excitation current extracted from winding 4 (13800V).

Core loss was evaluated for 13800V in Maxwell transient simulation which can be observed from figure below. Average core loss for whole operating period was 0.2399 kW.

Figure 2.70. Core loss for applied 13800V in four ports.

Here for applied 13800V, it can be observed from below figure that flux linkage Vs input current (excitation current) is taking the shape of B-H curve as we know flux linkage is associated with flux density and excitation current is associated with magnetic field strength.

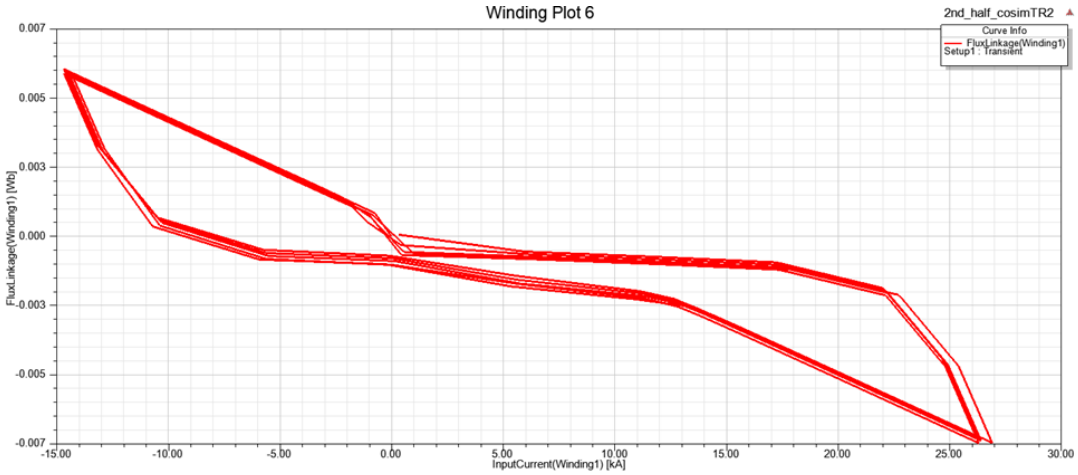

Figure 2.71. Flux linkage-input current for winding 1 (13800V).

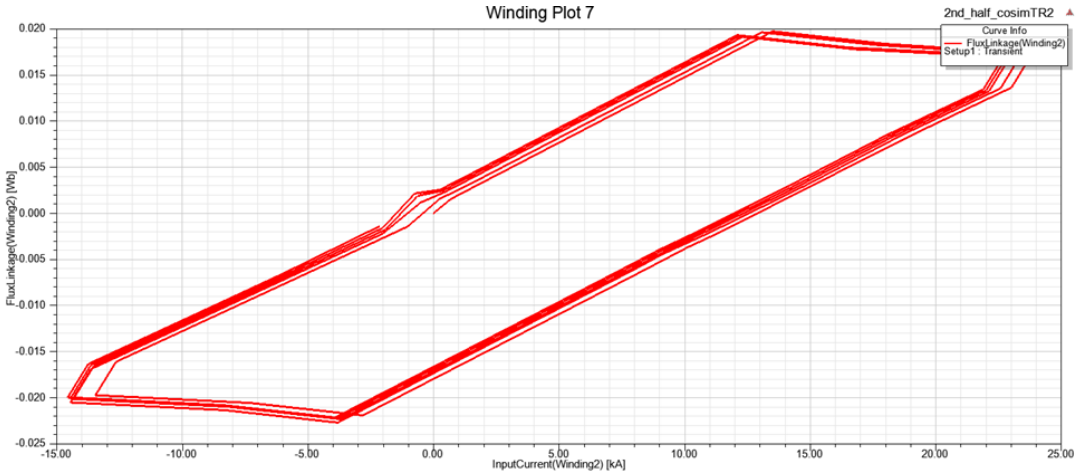

Figure 2.72. Flux linkage-input current for winding 2 (13800V).

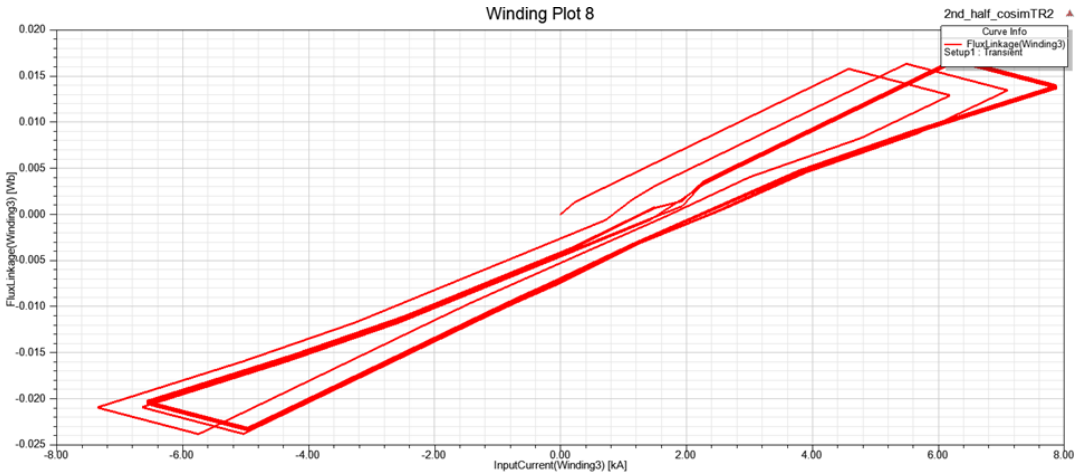

Figure 2.73. Flux linkage-input current for winding 3 (13800V).

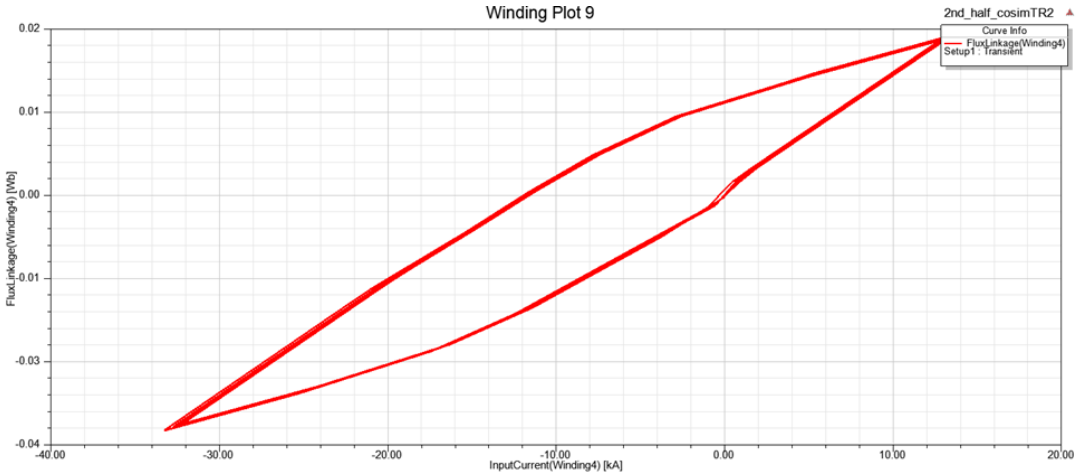

Figure 2.74. Flux linkage-input current for winding 4 (13800V).

Then flux density for this core was evaluated. As Maxwell was updated with average B-H curve from data sheet, B_{sat} was 0.38 Tesla for this case.

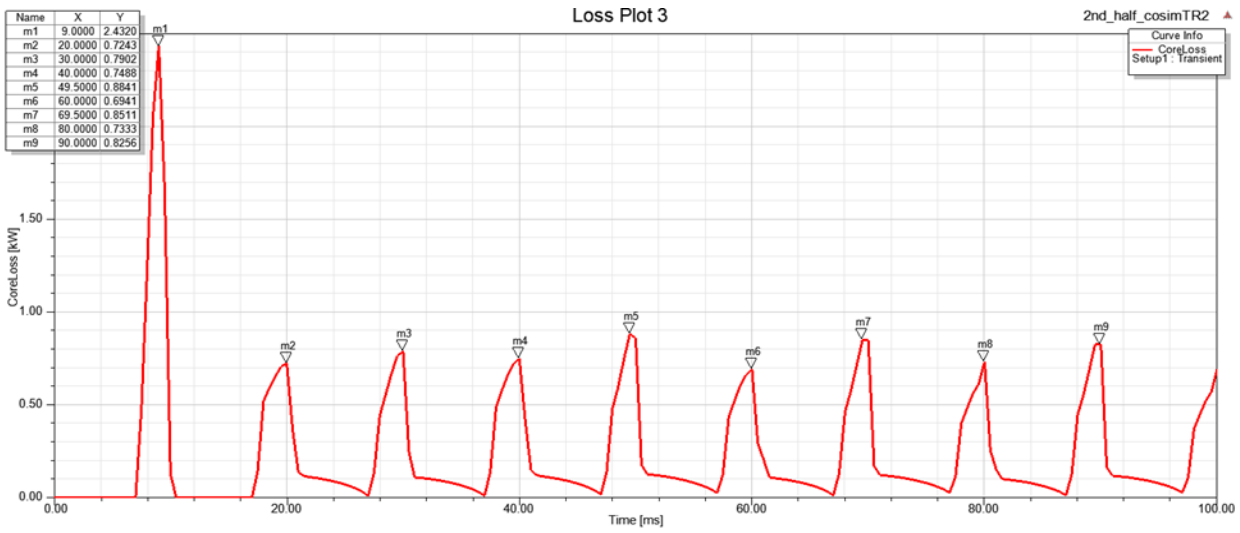

Figure 2.75. Time evaluation for peak core loss (13800V).

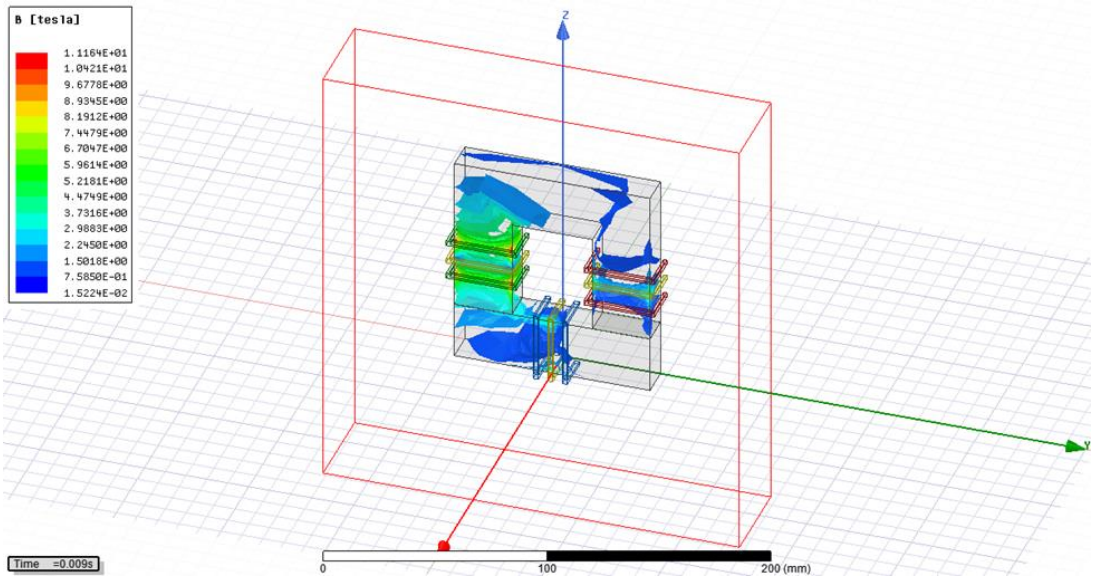

Figure 2.76. Flux density in 0.009 sec (13800V).

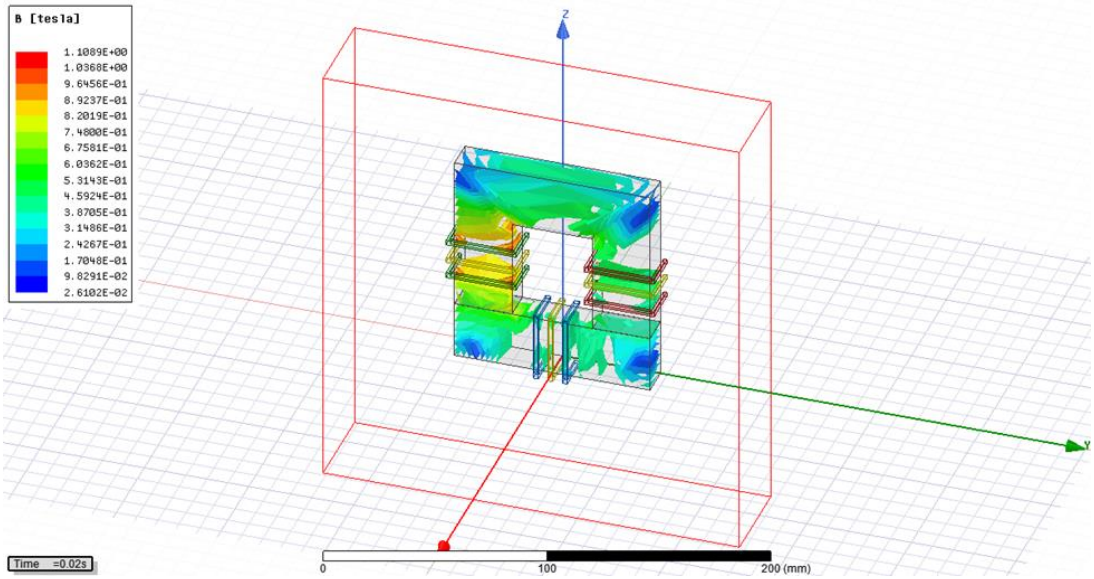

Figure 2.77. Flux density in 0.020 sec (13800V).

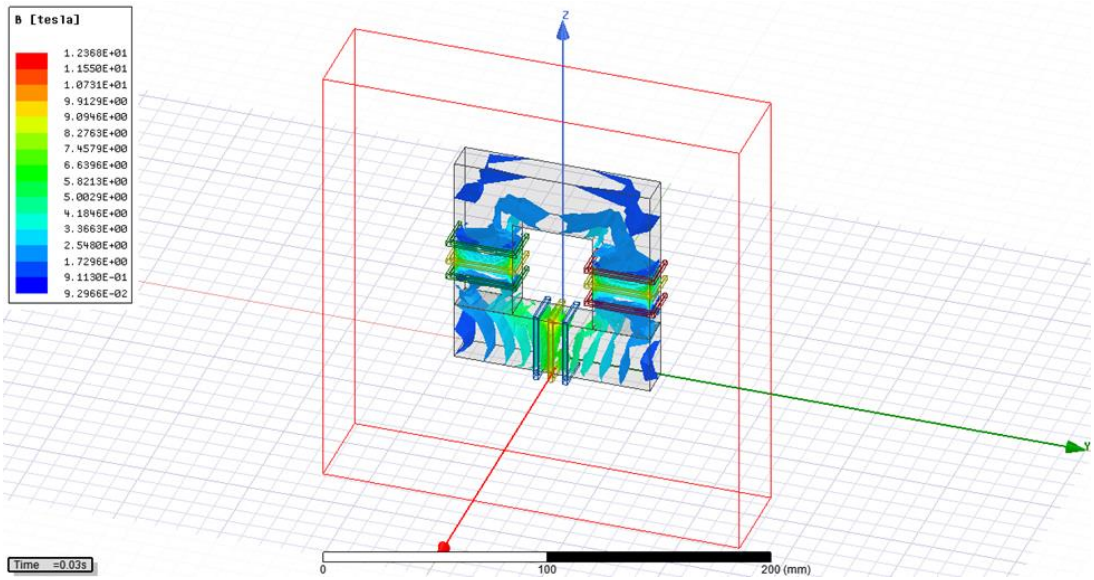

Figure 2.78. Flux density in 0.03 sec (13800 V).

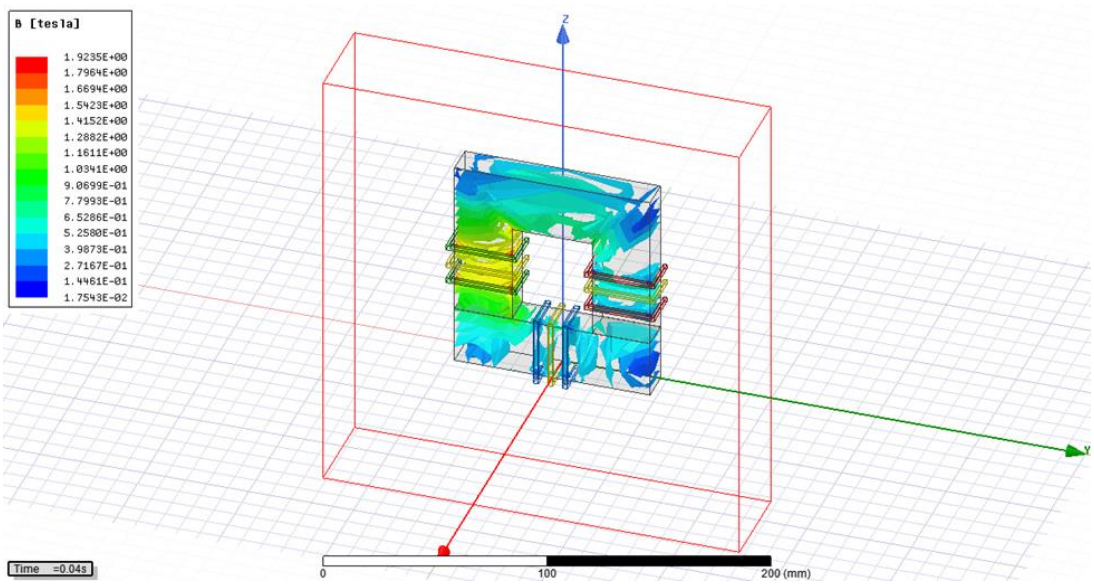

Figure 2.79. Flux density in 0.04 sec (13800V).

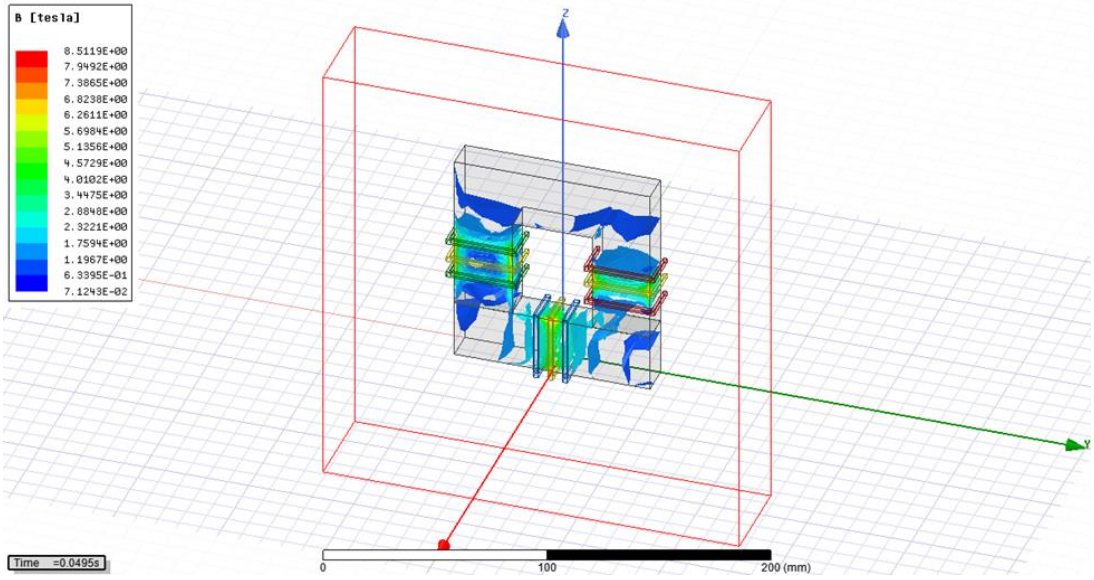

Figure 2.80. Flux density in 0.0495 sec (13800V).

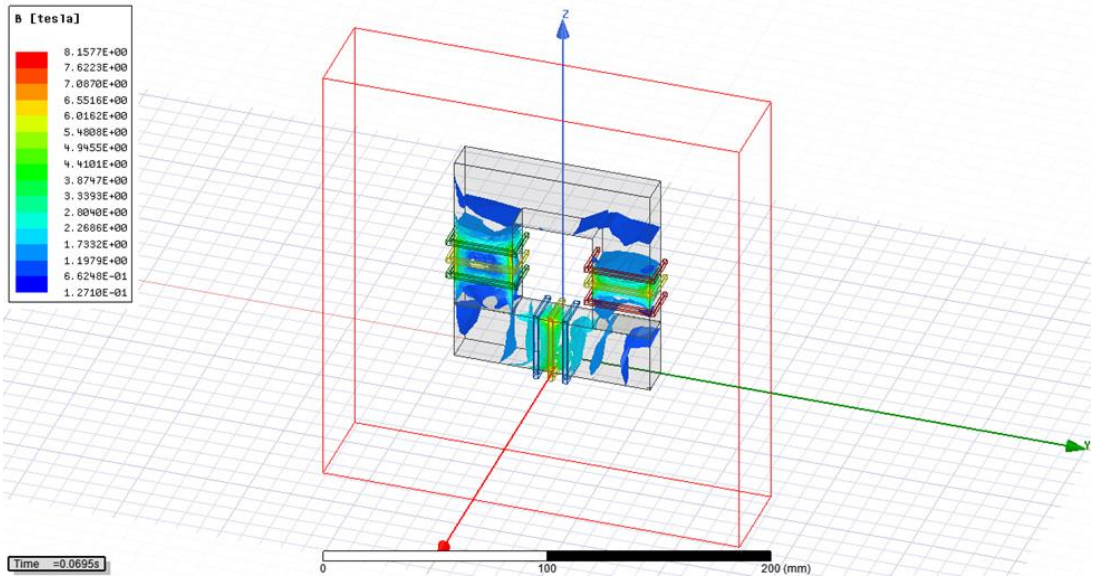

Figure 2.81. Flux density in 0.0695 sec (13800V).

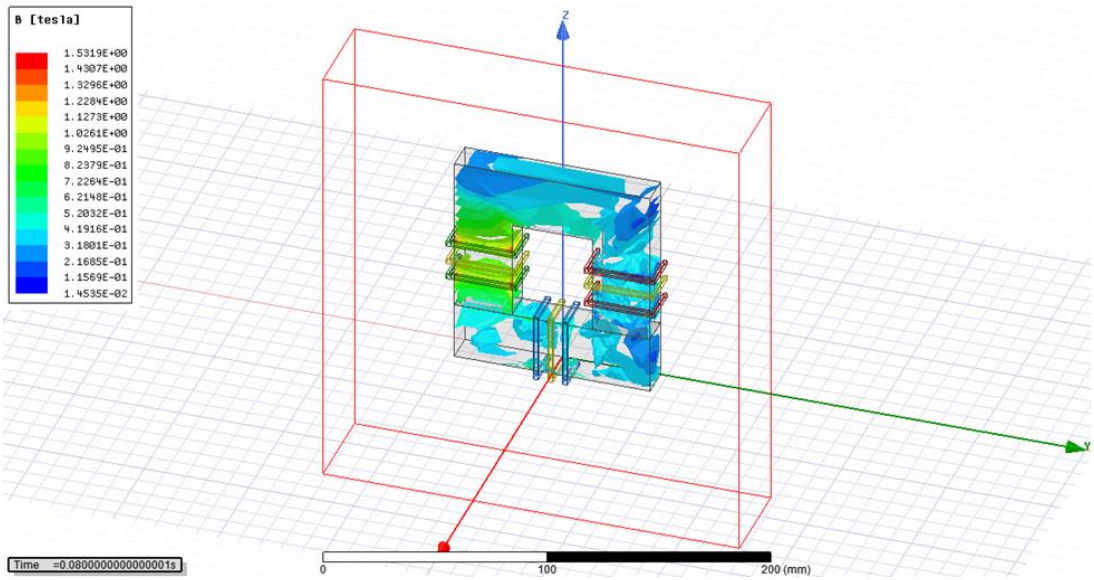

Figure 2.82. Flux density in 0.08 sec (13800V).

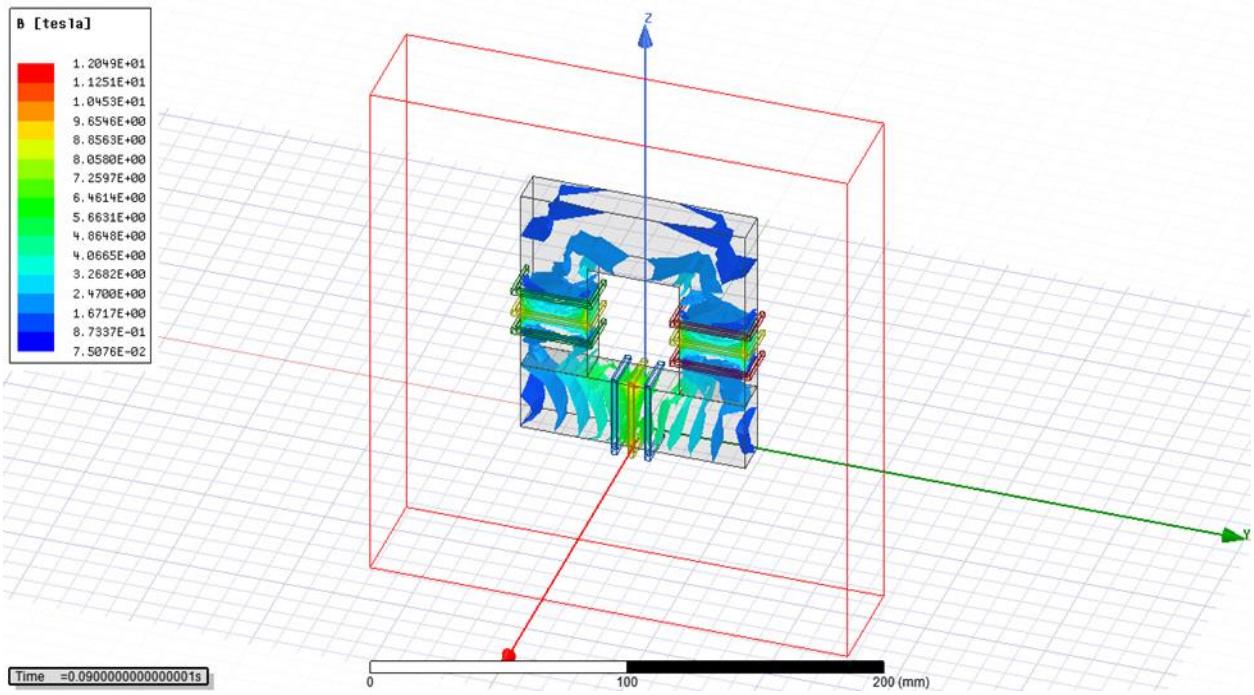

Figure 2.83. Flux density in 0.09 sec (13800V).

From above simulation in Case#3 it was evaluated that the desired level of flux density was more than expected level of B_{sat}. Average core loss is also very high 0.2399 kW.

4.3.5 Case#4: 750V applied to four ports

Here in Case#4, 750 V was applied in four ports to extract excitation current from Simplorer for transformer in Ansys Maxwell. In open loop control, the phase shift for the converter were $\varphi_1 = 0°, \varphi_2, \varphi_3 \varphi_4 = 2° - 5°$, duty cycle of gate pulses was 50% and switching frequency 50000 Hz to achieve 20 kW power transfer from port 1.

4.3.5.1 Excitation current for different windings (750V)

Excitation current of four windings were extracted from Ansys Simplorer that are given below.

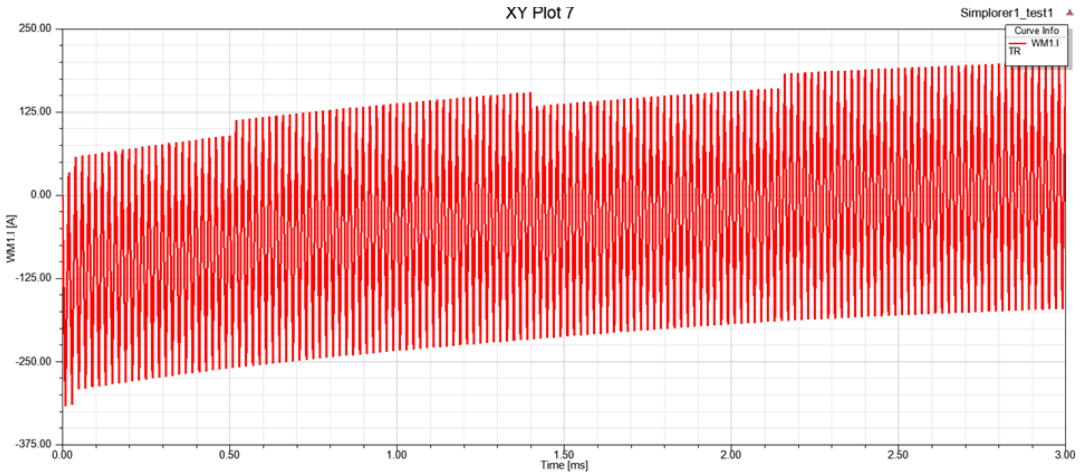

Figure 2.84. Excitation current extracted from winding 1 (750V).

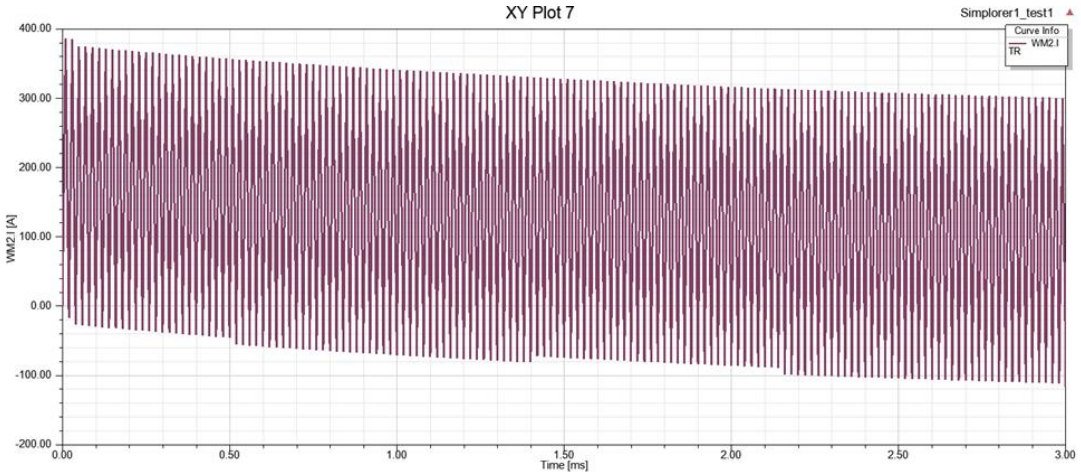

Figure 2.85. Excitation current extracted from winding 2 (750V).

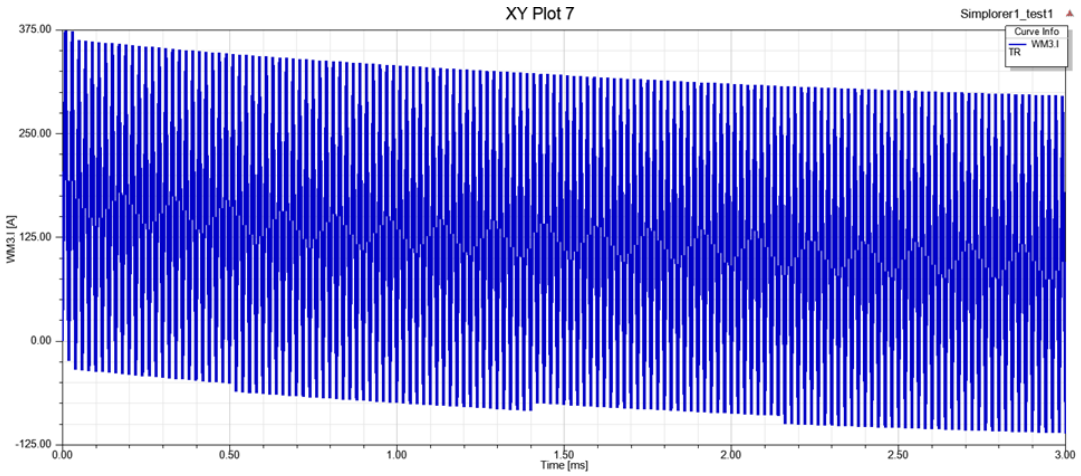

Figure 2.86. Excitation current extracted from winding 3 (750V).

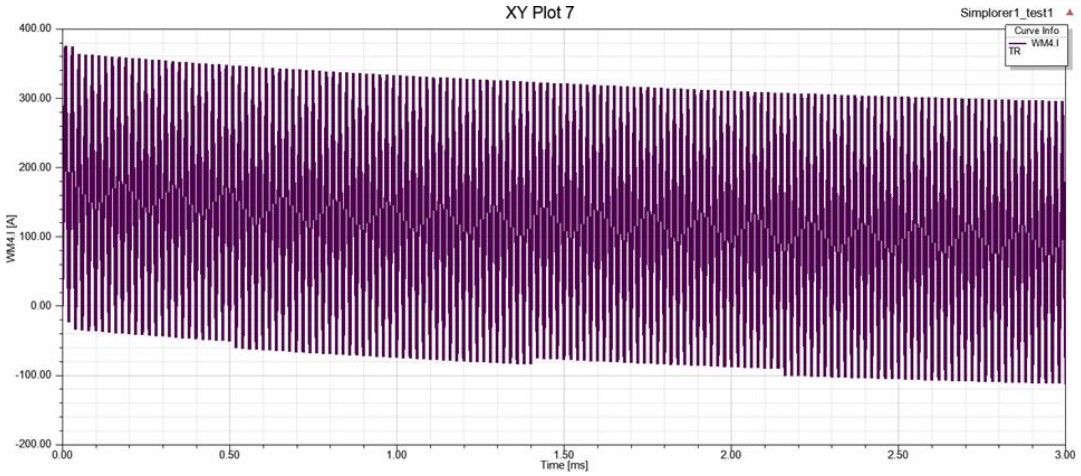

Figure 2.87. Excitation current extracted from winding 4 (750V).

Core loss was evaluated for 750V in Maxwell transient simulation which can be observed from figure below. Average core loss for whole operating period was 20.3619 mW.

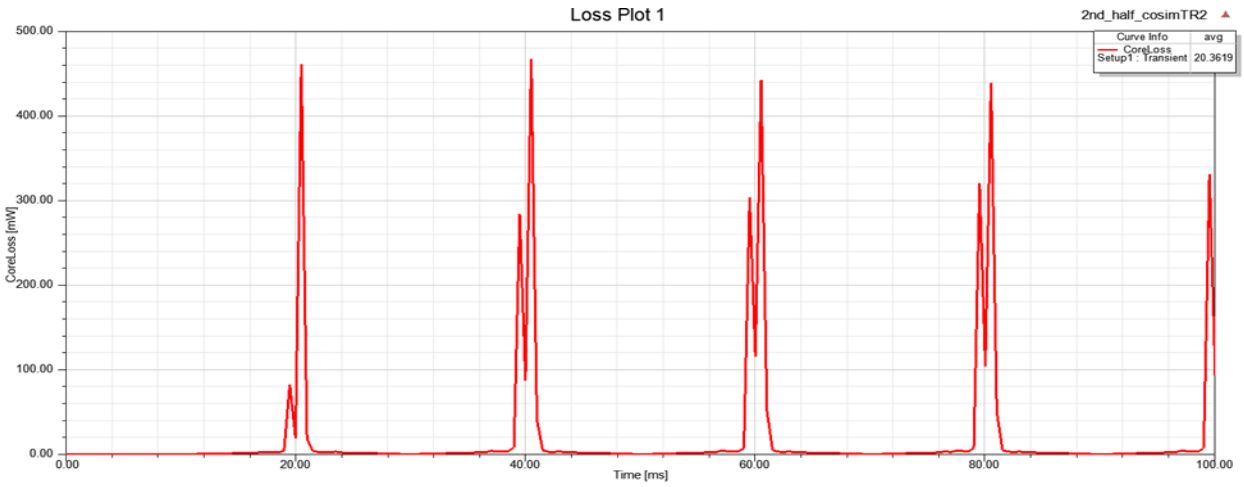

Figure 2.88. Core loss for applied 750V in four ports.

Here for applied 750V, it can be observed from below figure that flux linkage Vs input current (excitation current) is taking the shape of B-H curve as we know flux linkage is associated with flux density and excitation current is associated with magnetic field strength.

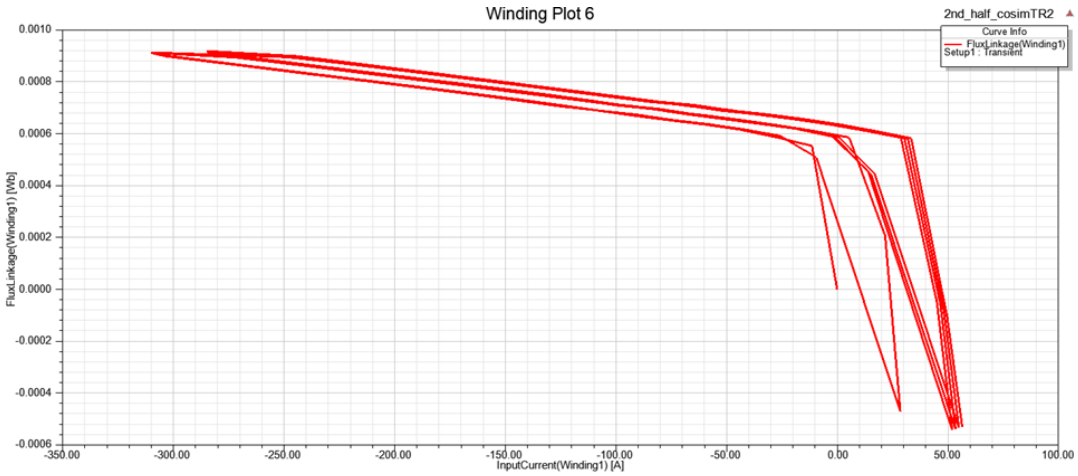

Figure 2.89. Flux linkage-input current for winding 1 (750V).

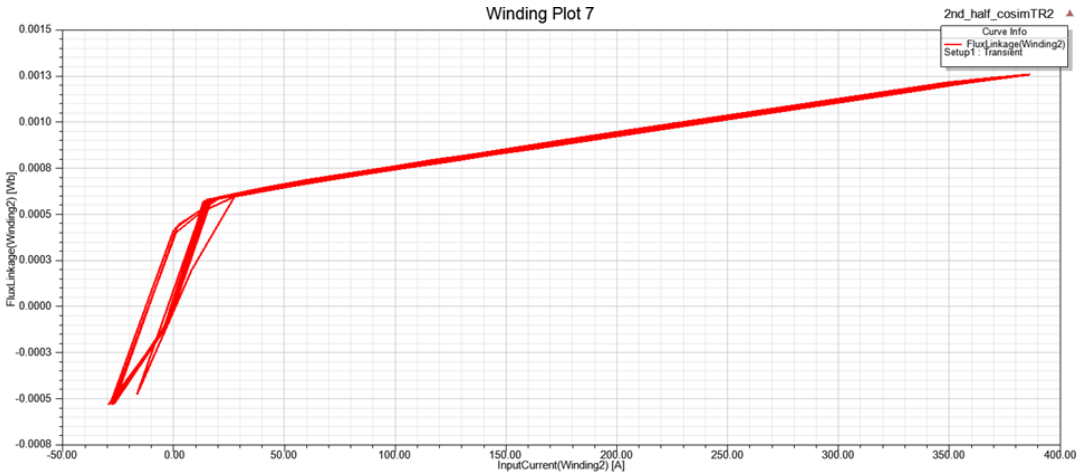

Figure 2.90. Flux linkage-input current for winding 2 (750V).

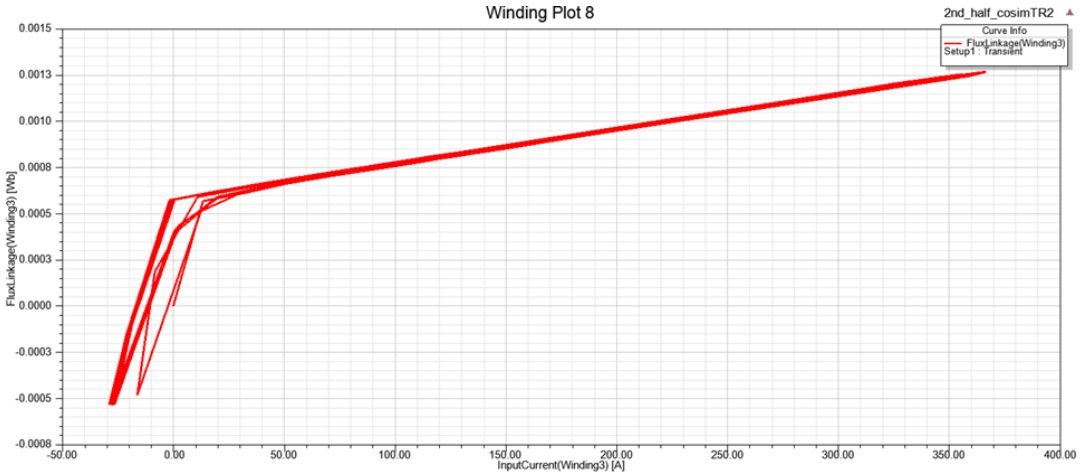

Figure 2.91. Flux linkage-input current for winding 3 (750V).

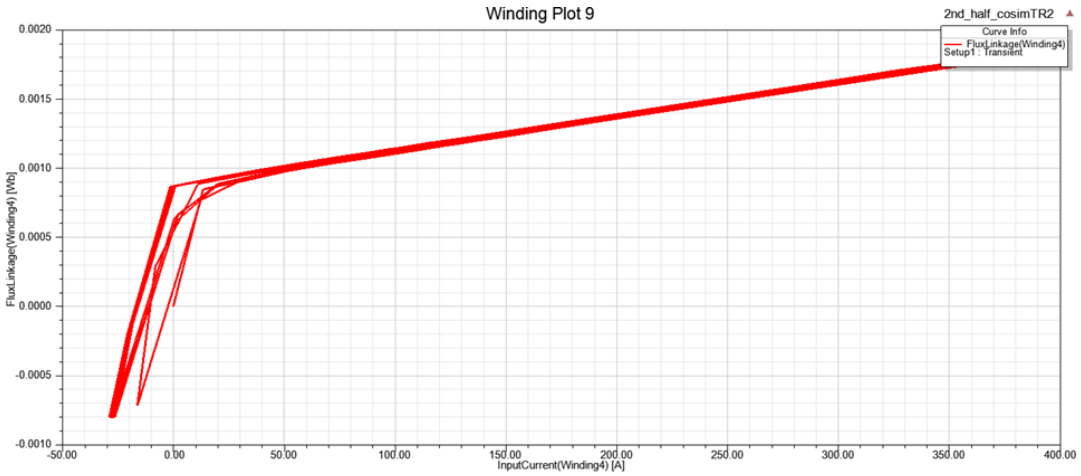

Figure 2.92. Flux linkage-input current for winding 4 (750V).

Then flux density for this core was evaluated. As Maxwell was updated with average B-H curve from data sheet, B_{sat} was 0.38 Tesla for this case.

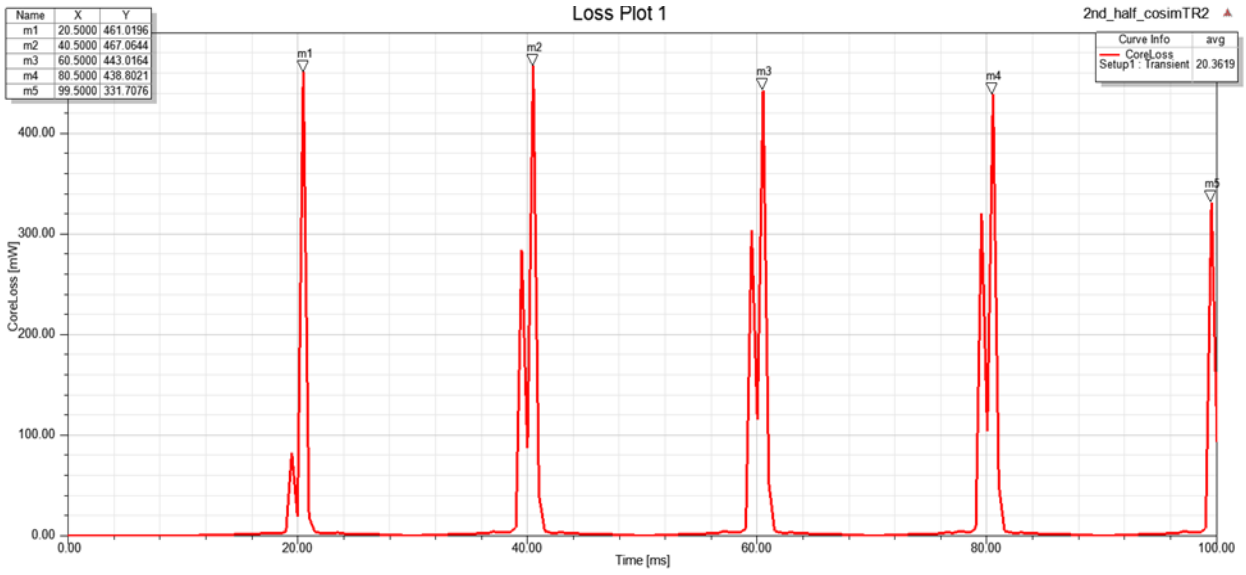

Figure 2.93. Time evaluation for peak core loss (750V).

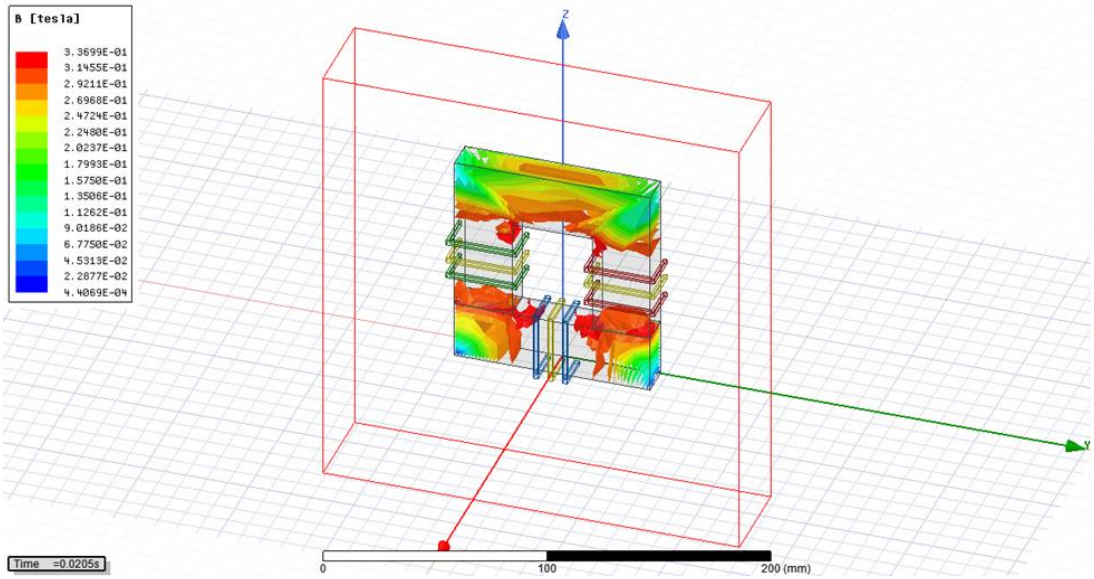

Figure 2.94. Flux density in 0.0205 sec (750V).

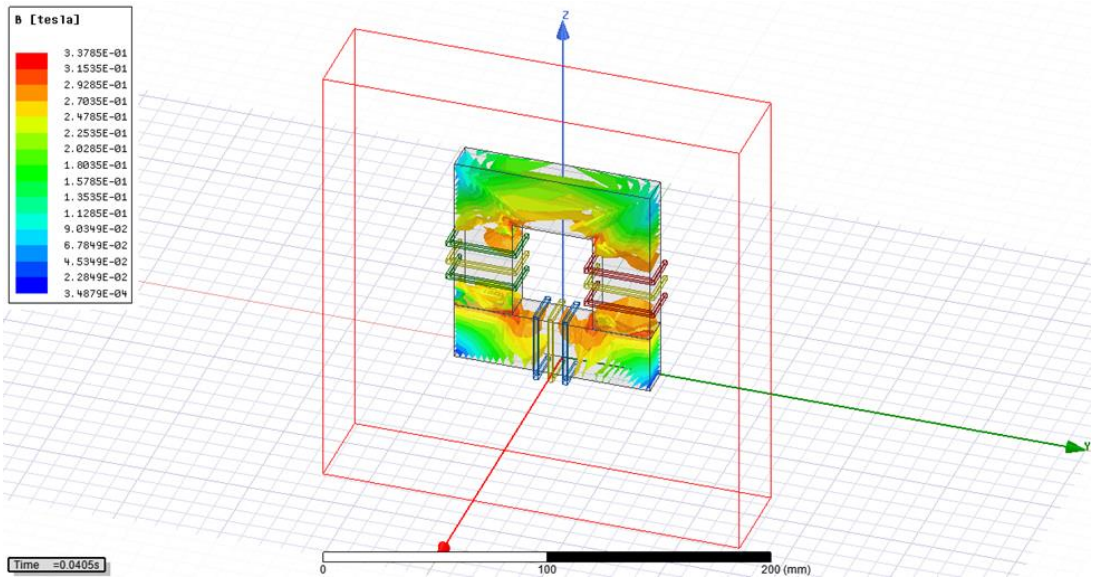

Figure 2.95. Flux density in 0.0405 sec (750V).

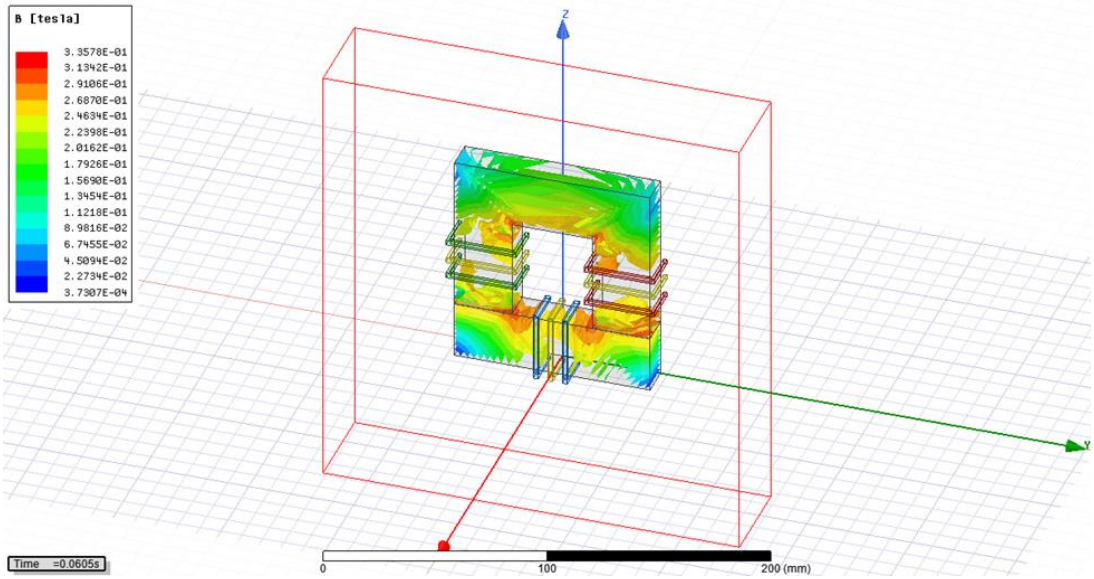

Figure 2.96. Flux density in 0.0605 sec (750 V).

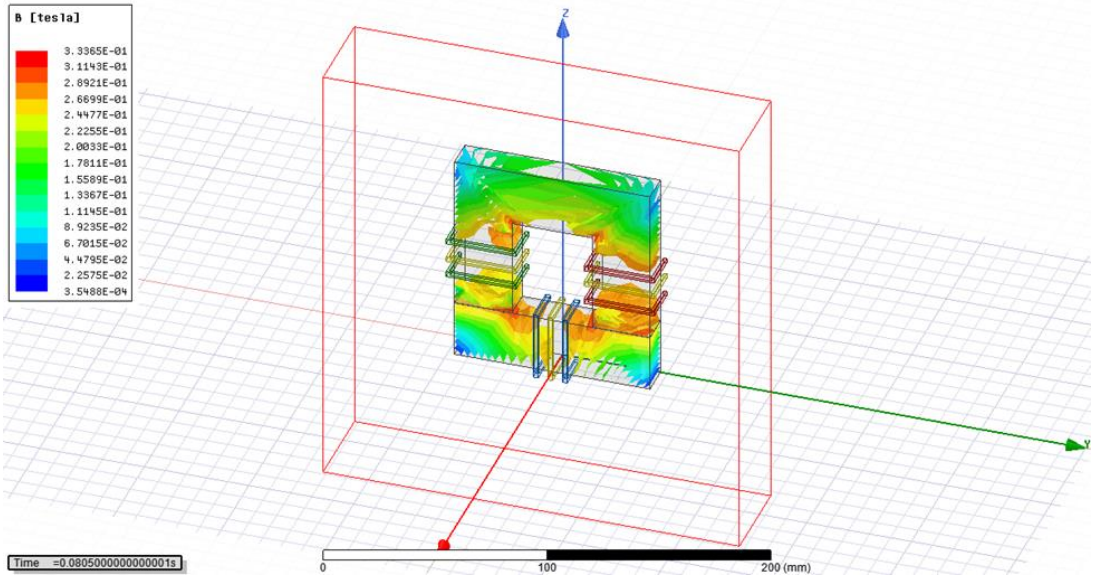

Figure 2.97. Flux density in 0.08 sec (750V).

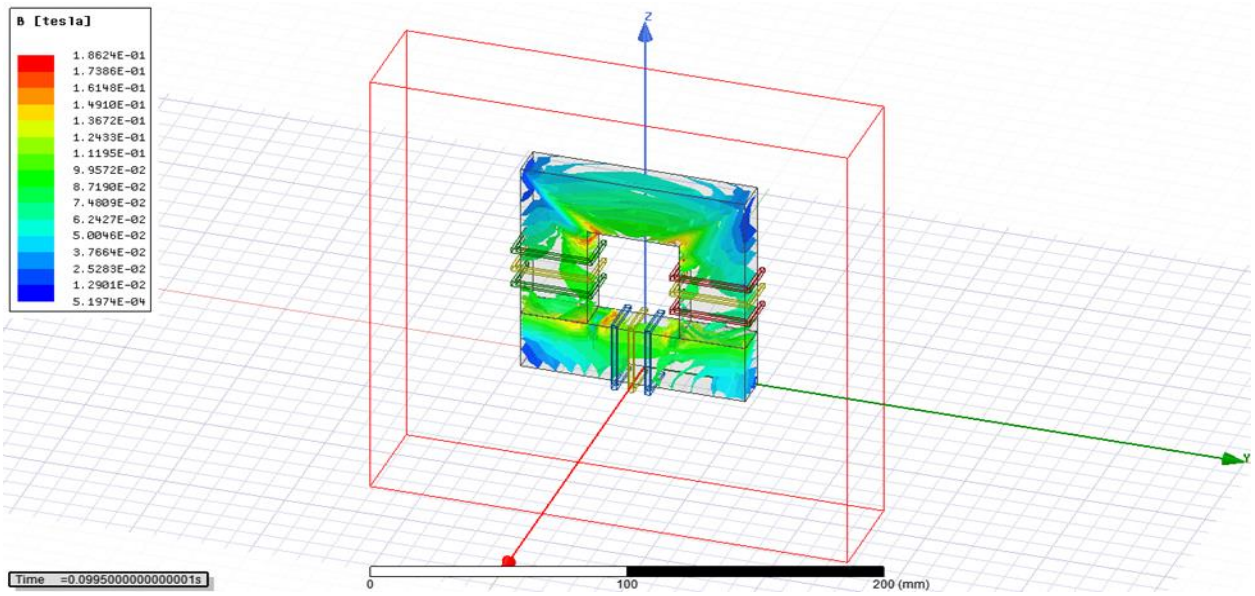

Figure 2.98. Flux density in 0.0995 sec (750V).

From above simulation for Case#4, to transfer 20 kW of power from port 1 the desired level of flux density was below B_{sat} . Average core loss is in acceptable range 20.3619 mW.

4.4 Winding loss analysis

To evaluate core loss and winding loss is one of the main design criteria for constructing high frequency transformer. For core loss we know that [12]

$$P_{core} = K_{fe}(\Delta B)^{\beta} A_c l_m$$

A_c is cross sectional area of the core, l_m is mean magnetic path length of the core. ΔB is peak flux density. The copper loss can be expressed

$$P_{cu} = \left(\frac{\rho \lambda_1^2 I_{tot}^2}{4K_u}\right)\left(\frac{MLT}{W_A A_c^2}\right)\left(\frac{1}{\Delta B}\right)^2$$

As peak flux density is inversely proportional to copper loss (winding loss) and proportional to core loss, it is important to find out optimum value of flux density for better performance of the transformer.

We know from Maxwell's equations-

$$\nabla \times E = -\frac{\partial B}{\partial t}$$

$$\nabla \times H = J + \frac{\partial D}{\partial t}$$

$$\nabla . D = \rho$$

$$\nabla . B = 0$$

B and D are magnetic and electric flux density, H and E are magnetic and electric field intensity, J is current density.

From Lorentz force we can have an expression for ohmic losses-

$$\frac{dP_{ohm-loss}}{dV} = J . E \ (^{watt}/_{m^3})$$

AC magnetic field intensity H has an impact on current density distribution J in wires. Eddy current appears in conductors because of induced H field. Eddy effect will push the current to flow near the surface of the conductor. As eddy current and applied current flow in same direction near the surface, it will increase current density near conductor surface.

At high frequency conductors tend to have more copper loss because of skin effect and proximity effect. The current density J exponentially reduces from surface to center of the conductor. Skin depth δ, where flux density stays during high frequency, can be expressed as [12] -

$$\delta = \frac{1}{\sqrt{\pi . \sigma . f . \mu}}$$

μ is magnetic permeability, σ is electrical permeability and f is frequency of current flowing.

Proximity effect is created by magnetic field flowing through surrounded conductors near a certain conductor. It will increase eddy current flow in conductors induced by external magnetic field. This will induce a copper loss in conductors because of increase current density.

4.5 Winding loss simulation for four-port transformer

4.5.1 Case#1: 100 V applied to four ports

Magnetic field intensity (H):

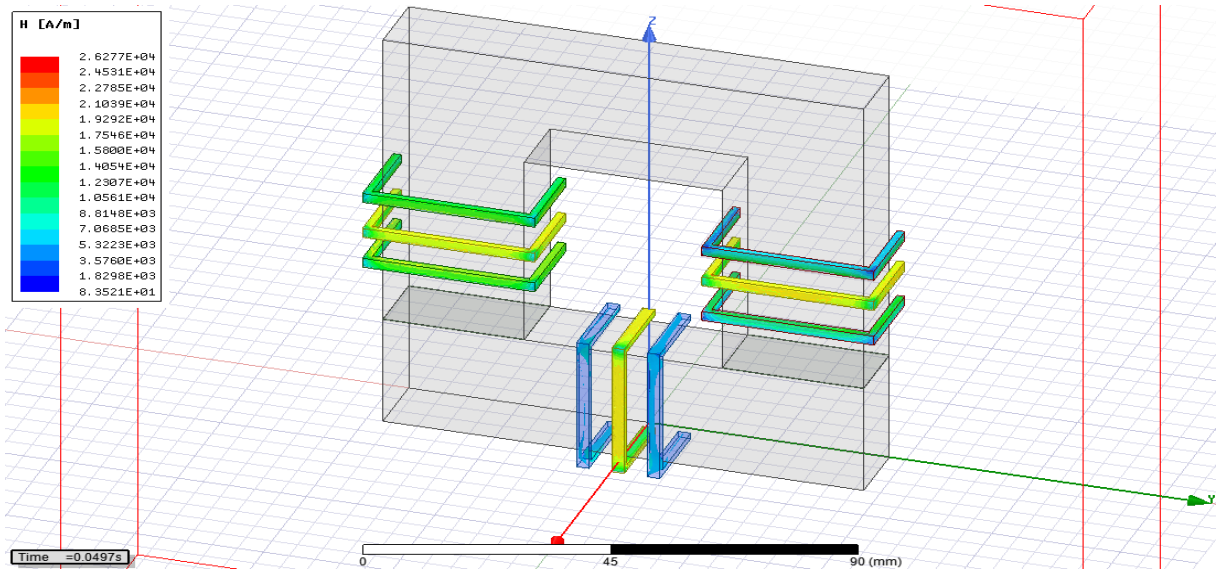

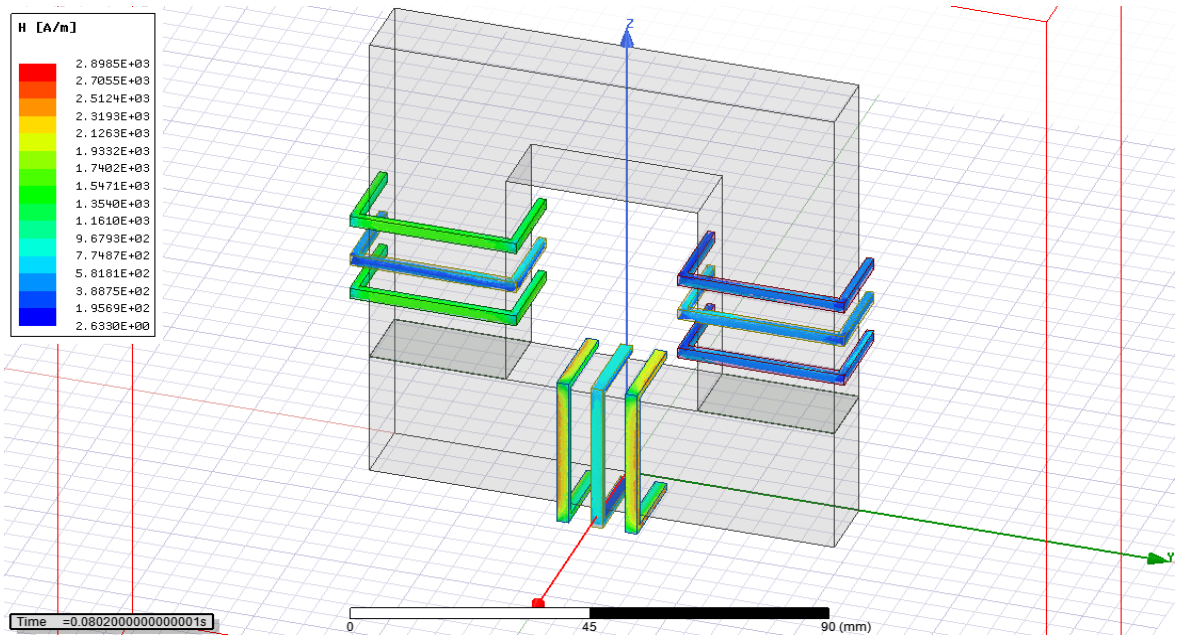

Figure 2.99. Magnetic field intensity (H) for 100 V.

Current density (J):

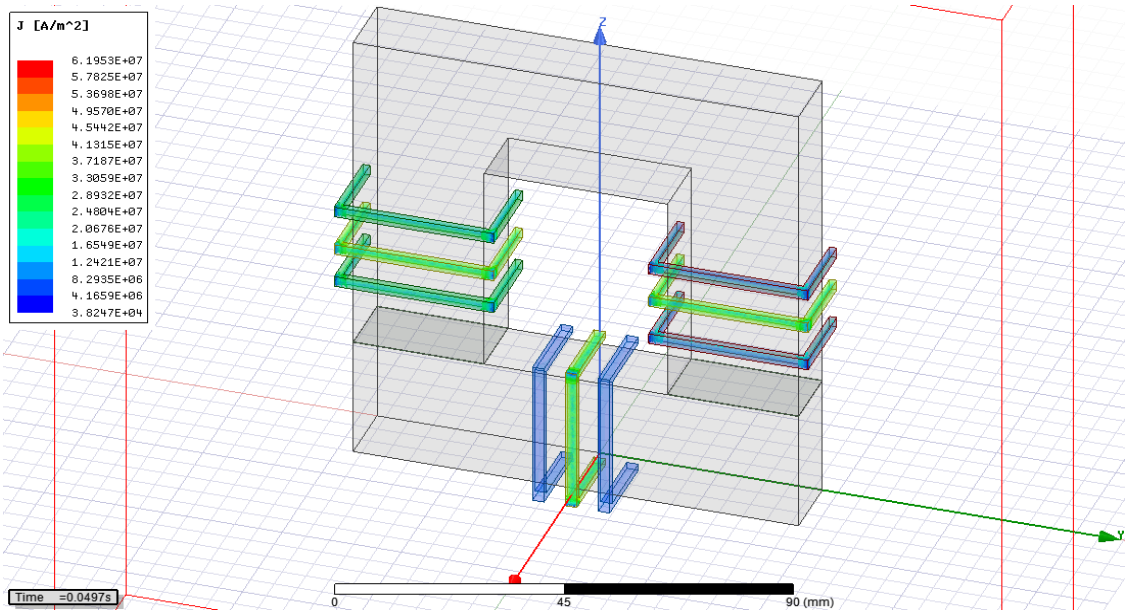

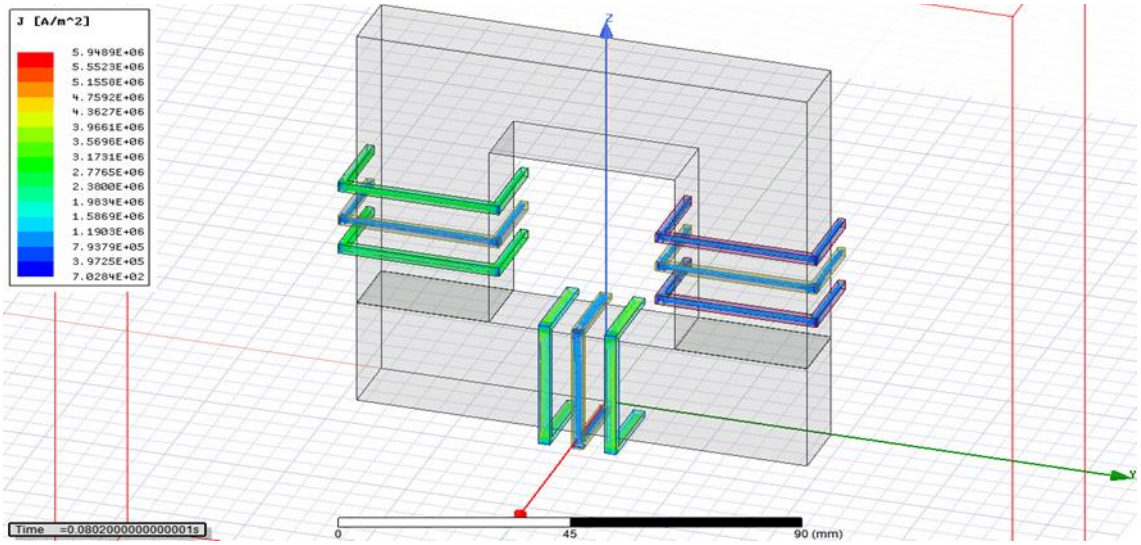

Figure 2.100. Current density (J) for 100 V.

Ohmic loss:

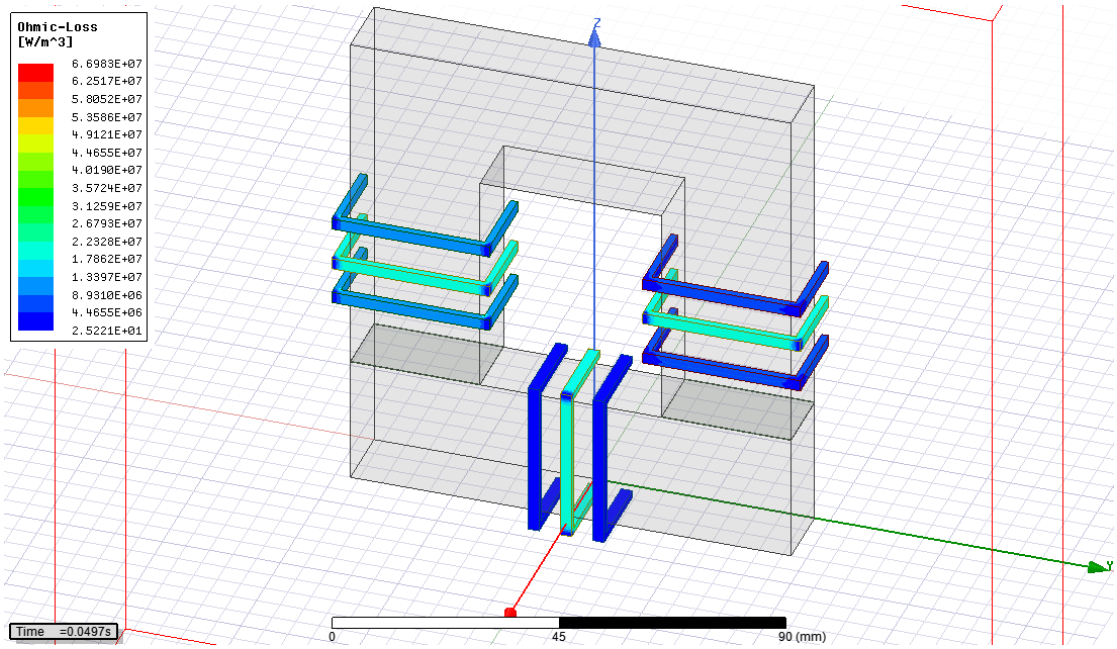

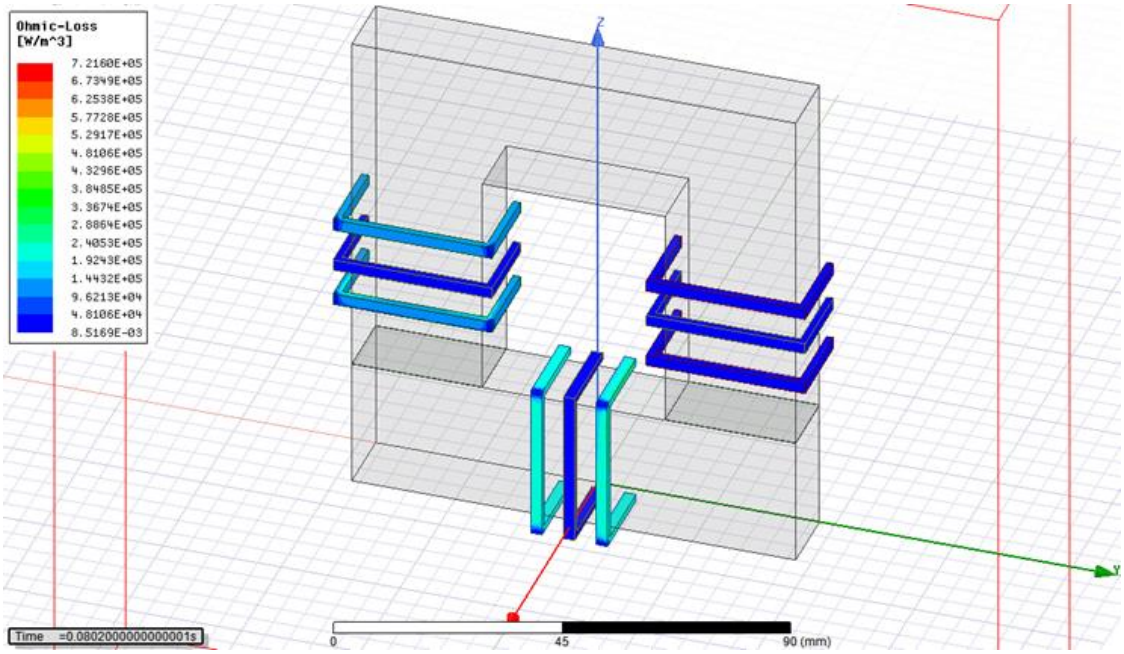

Figure 2.101. Ohmic loss for 100 V.

4.5.2 Case#2: 750 V applied to four ports

Magnetic field intensity (H):

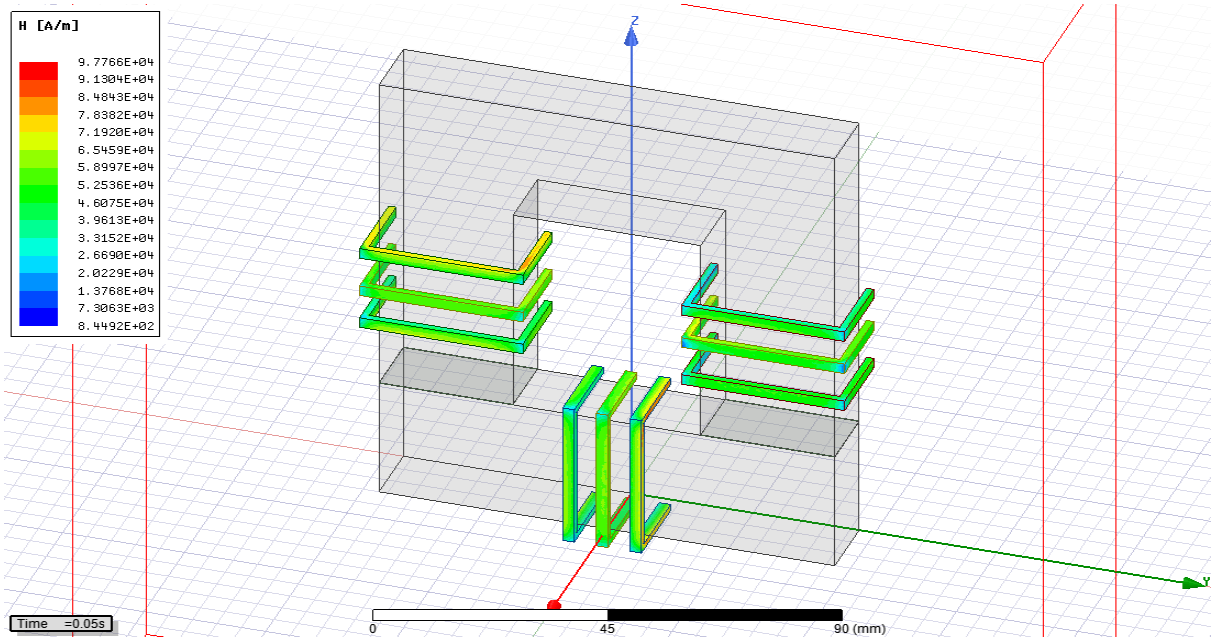

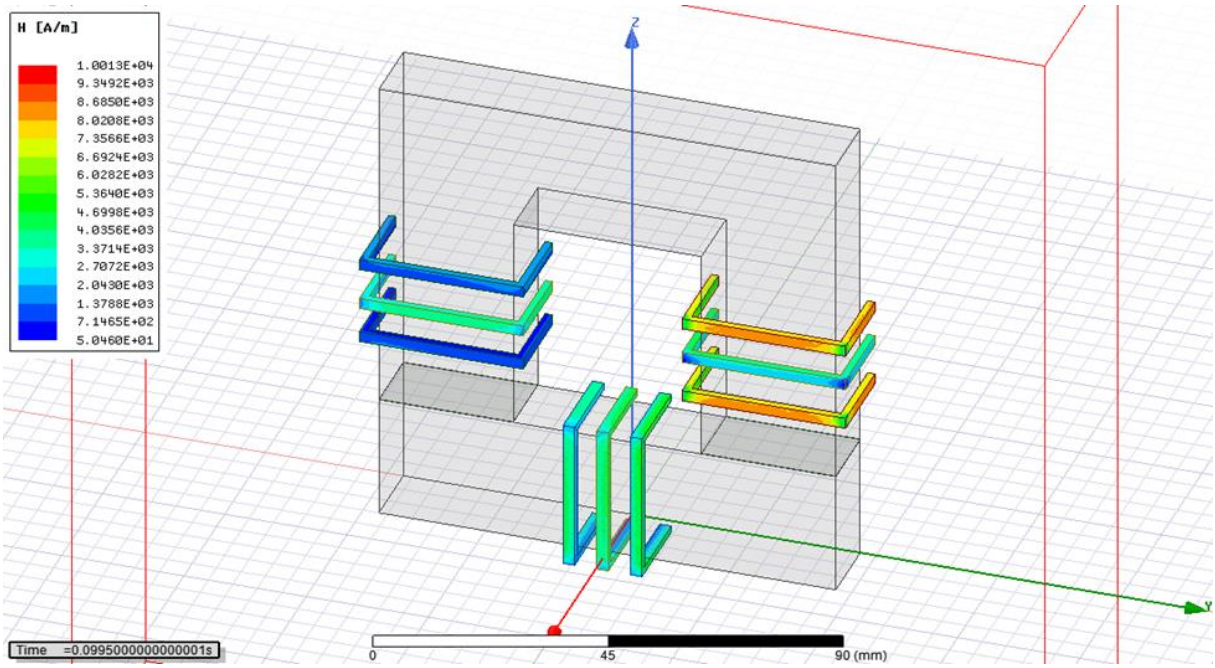

Figure 2.102. Magnetic field intensity (H) for 750 V.

Current density (J):

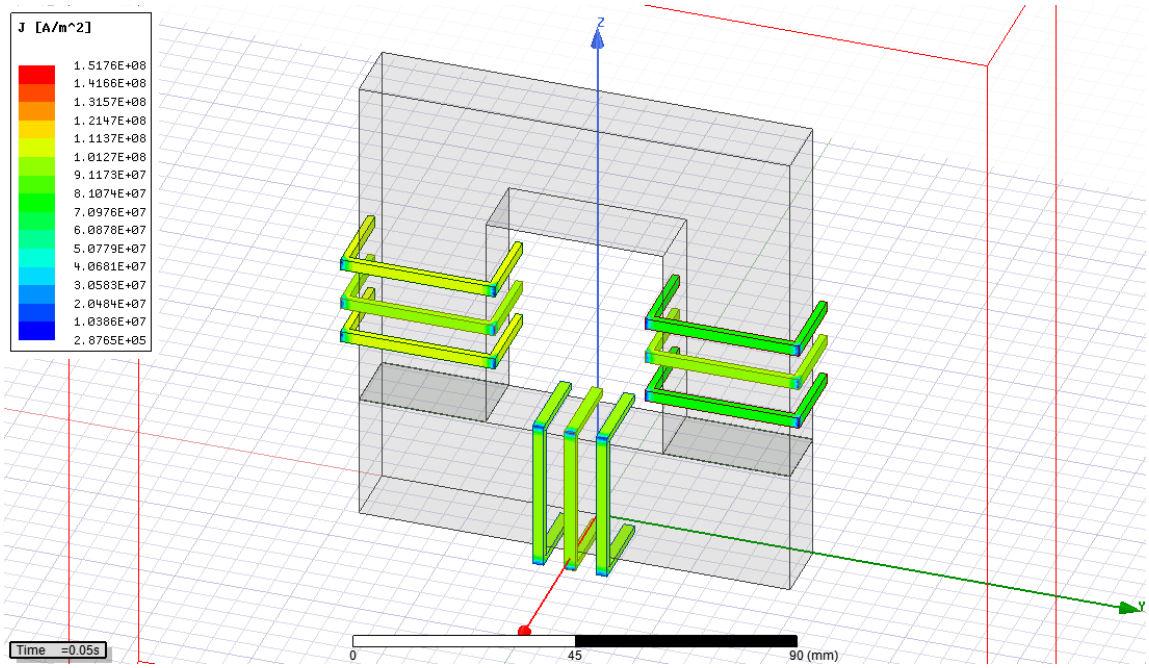

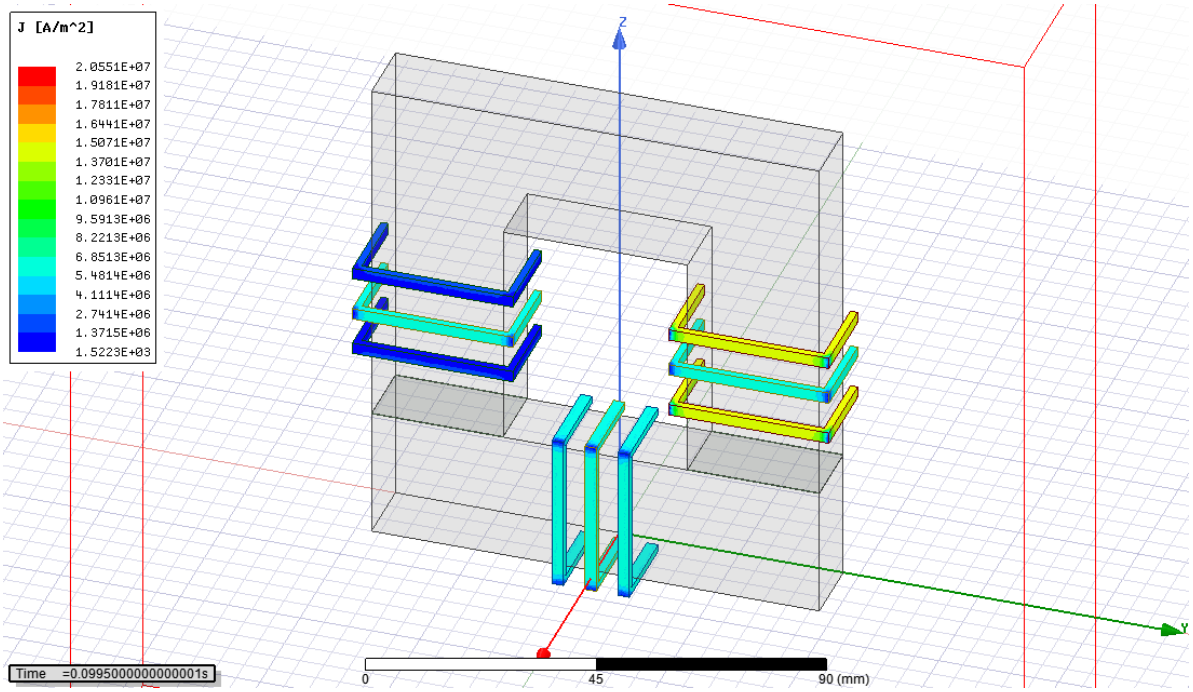

Figure 2.103. Current density (J) for 750 V.

Ohmic loss:

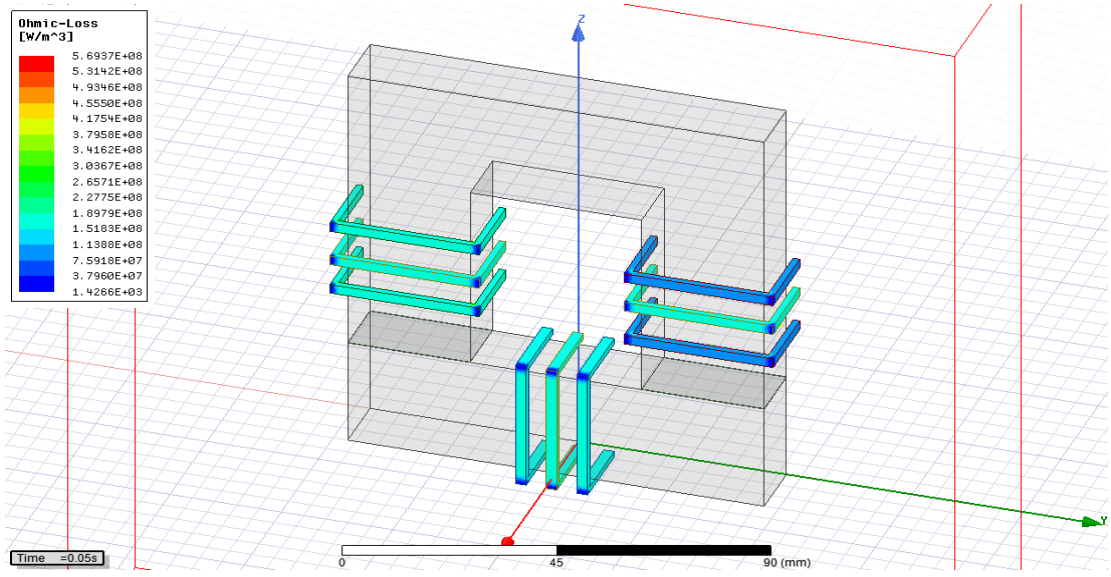

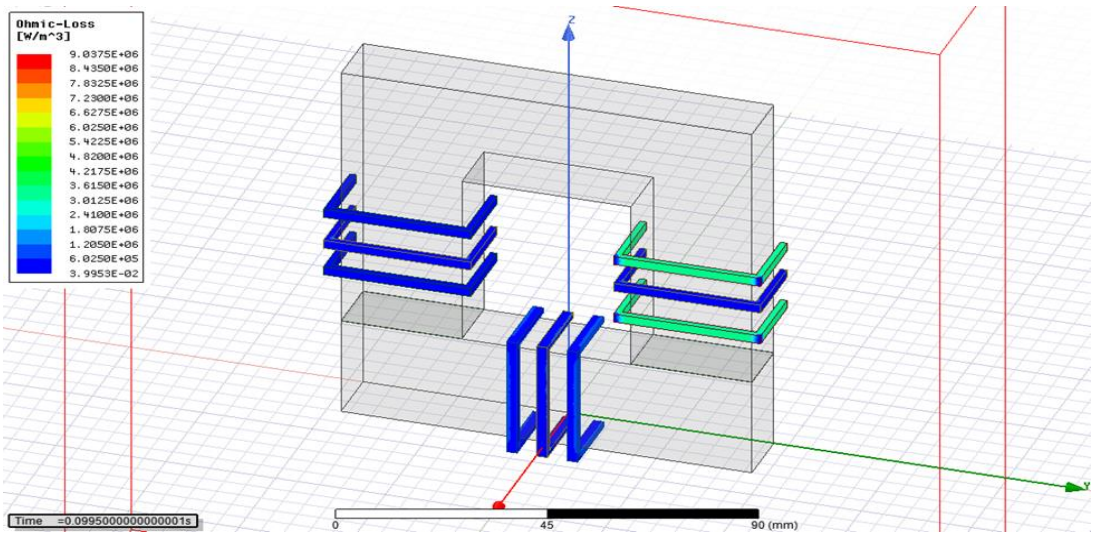

Figure 2.104. Ohmic loss for 750 V.

4.5.3 Case#3: 2400 V applied to four ports

Magnetic field intensity (H):

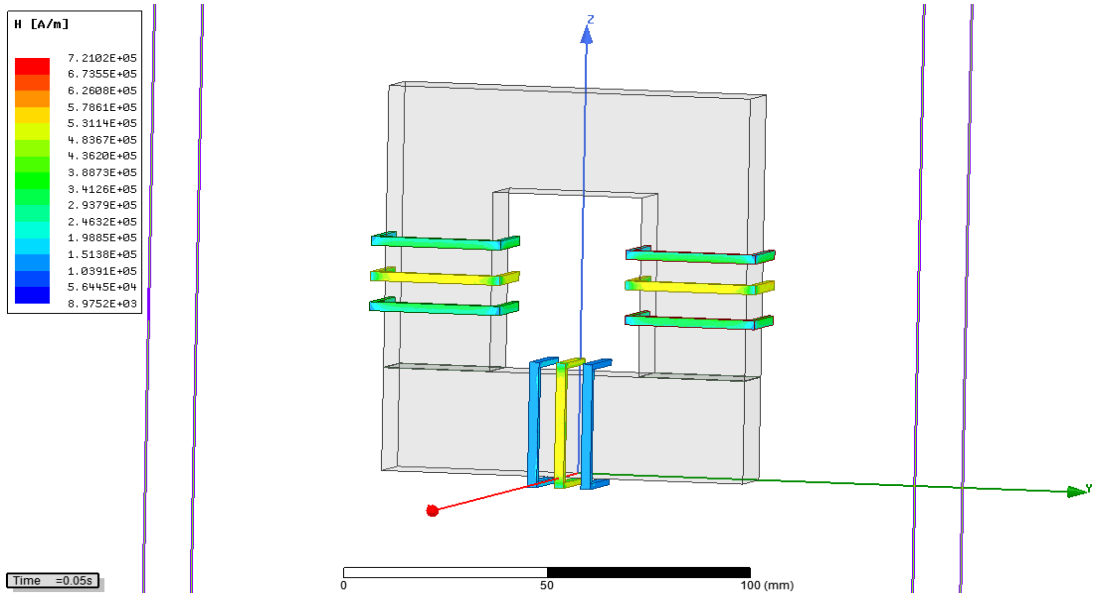

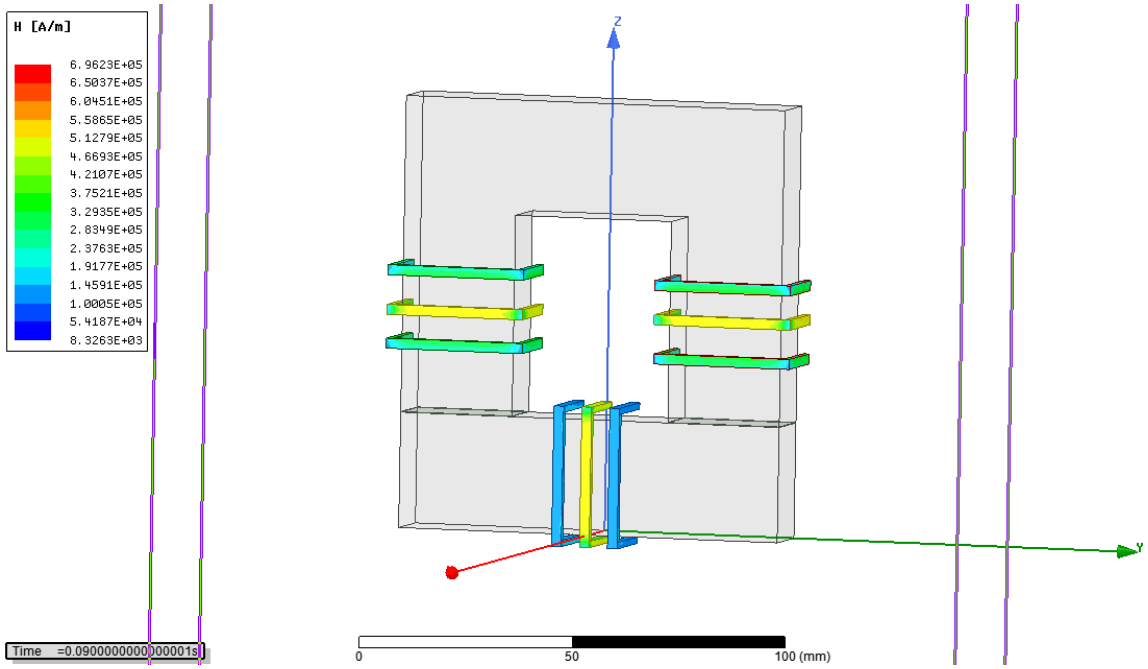

Figure 2.105. Magnetic field intensity (H) for 2400 V.

Current density (J):

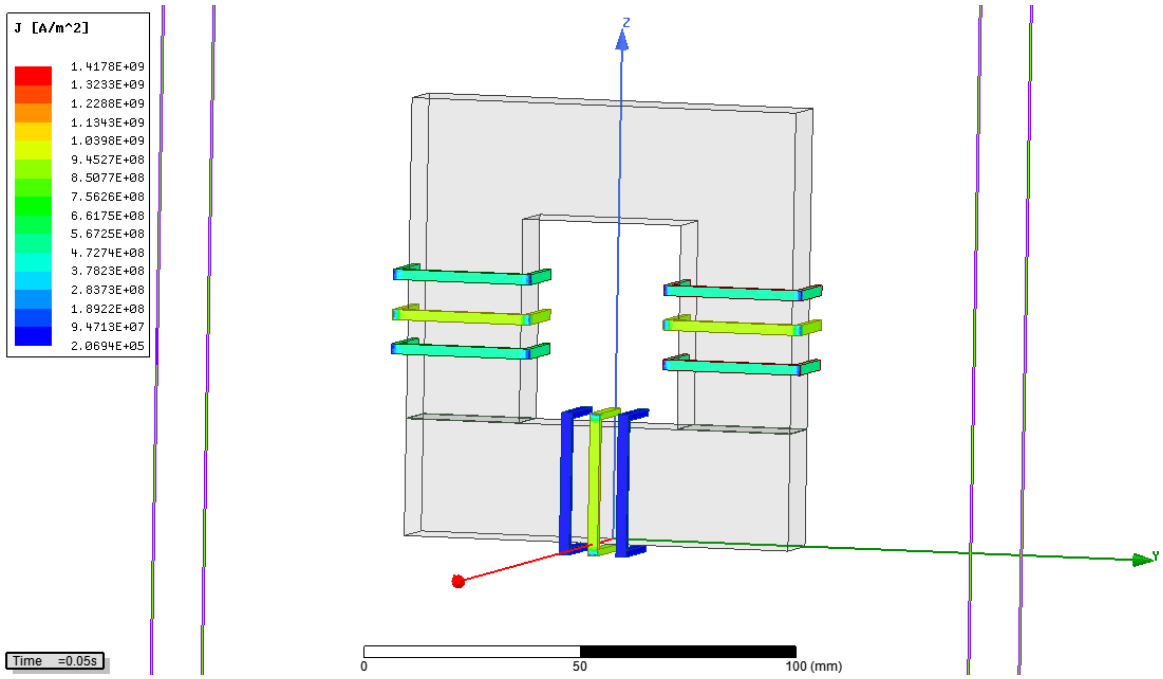

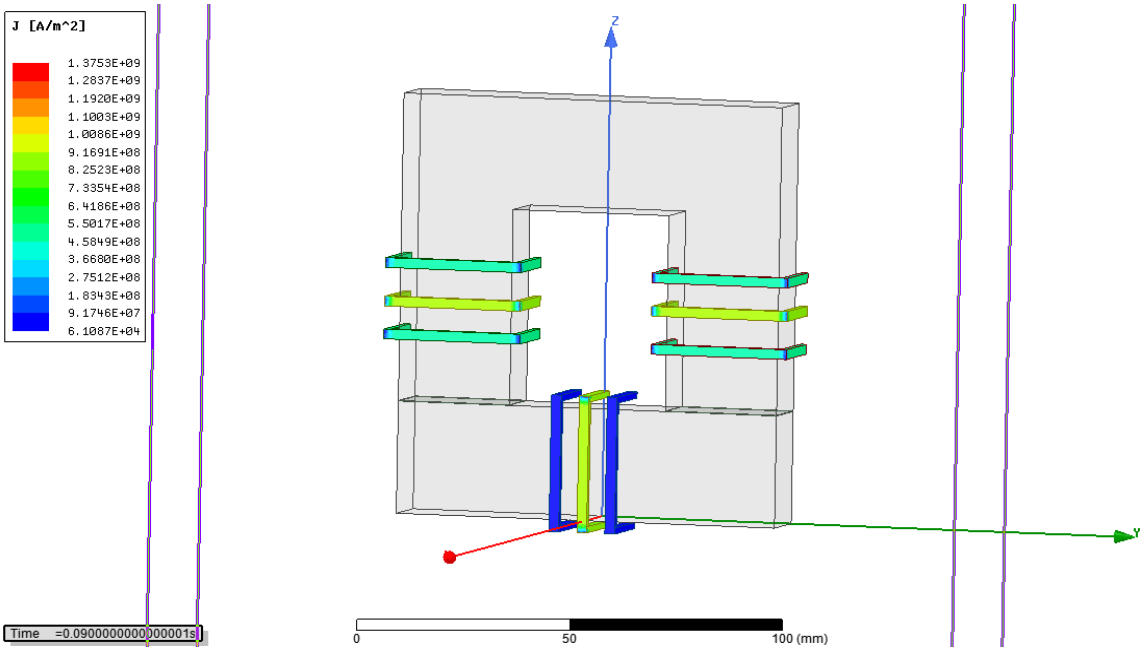

Figure 2.106. Current density (J) for 2400 V.

Ohmic loss:

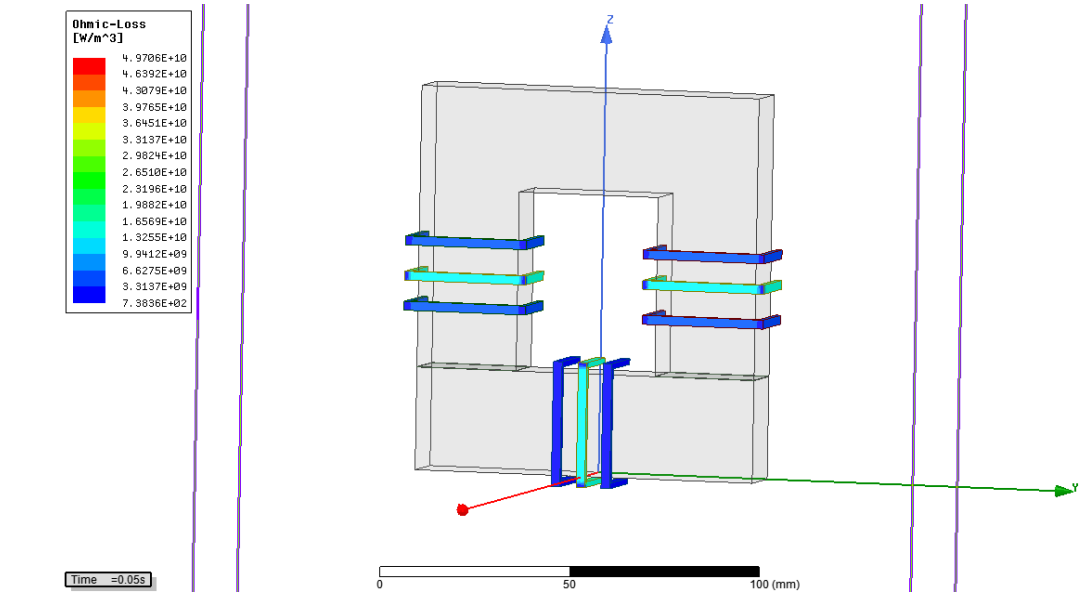

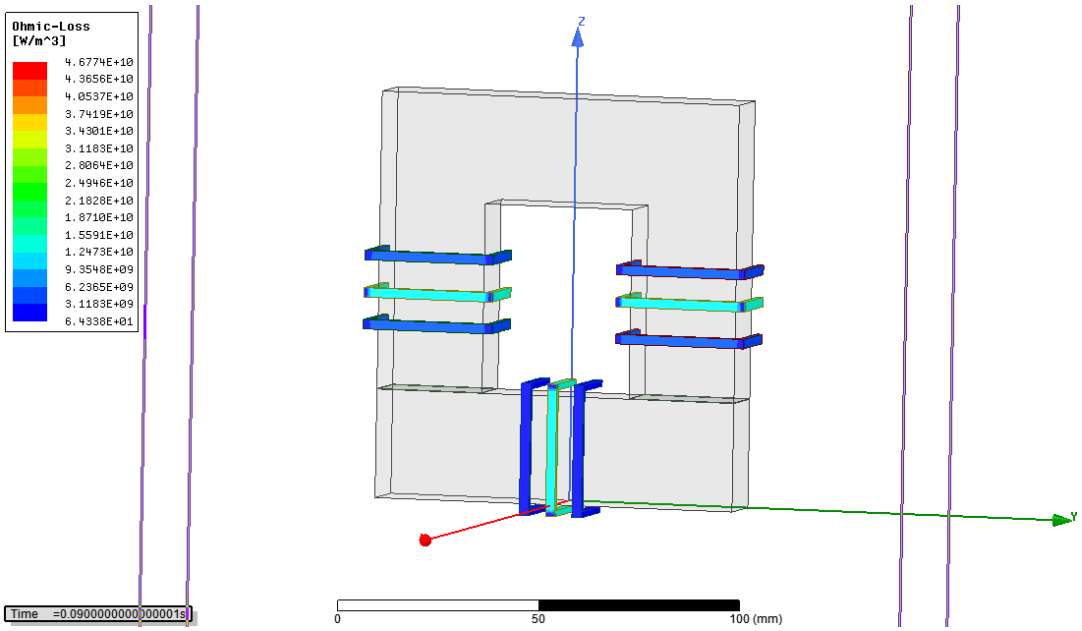

Figure 2.107. Ohmic loss for 2400 V.

4.5.4 Case#4: 13800 V applied to four ports

Magnetic field intensity (H):

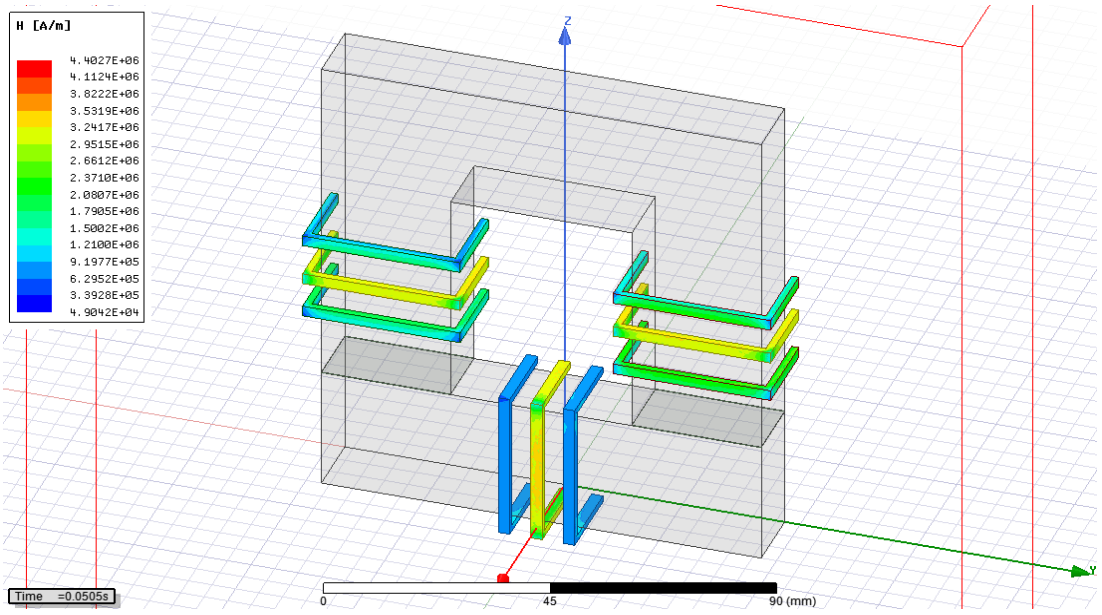

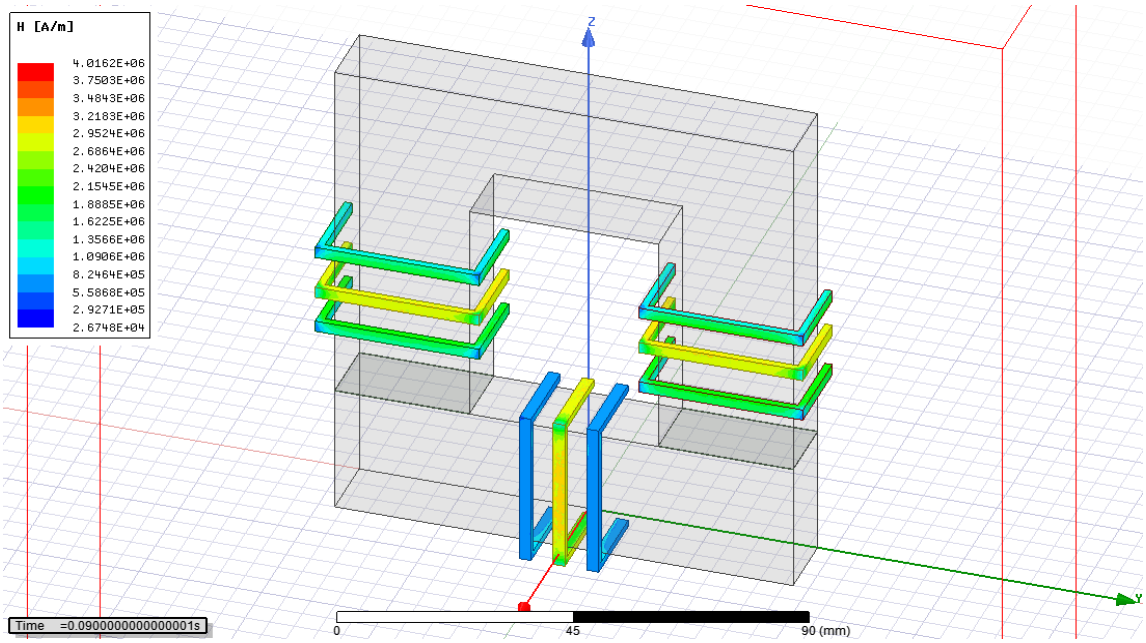

Figure 2.108. Magnetic field intensity (H) for 13800 V.

Current density (J):

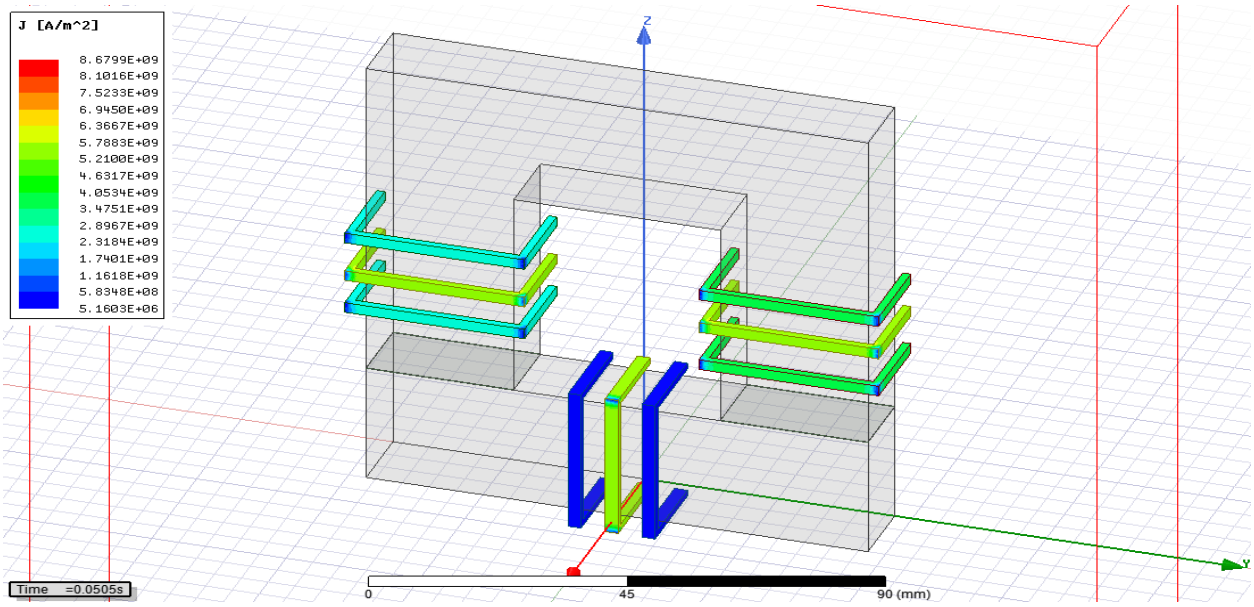

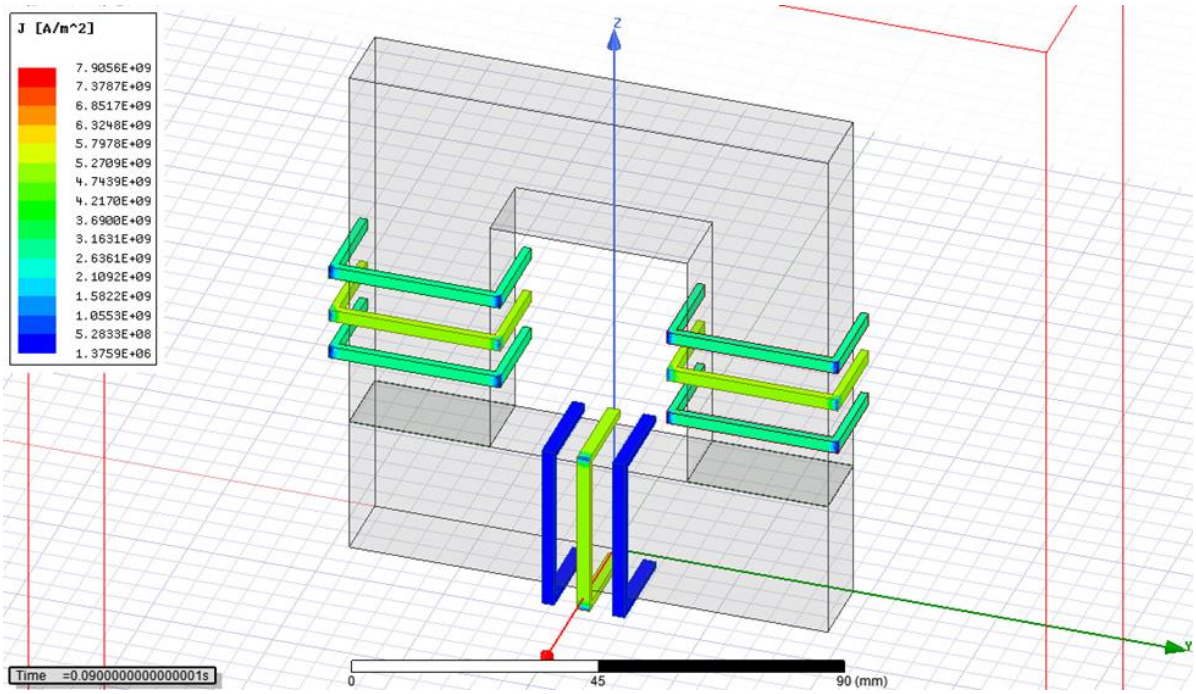

Figure 2.109. Current density (J) for 13800 V.

Ohmic loss:

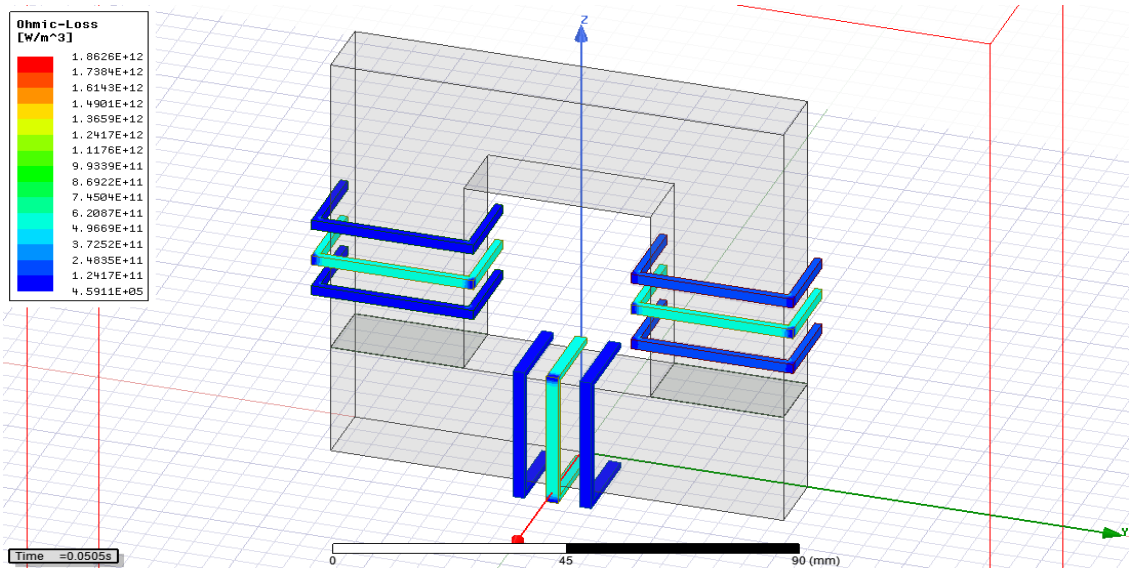

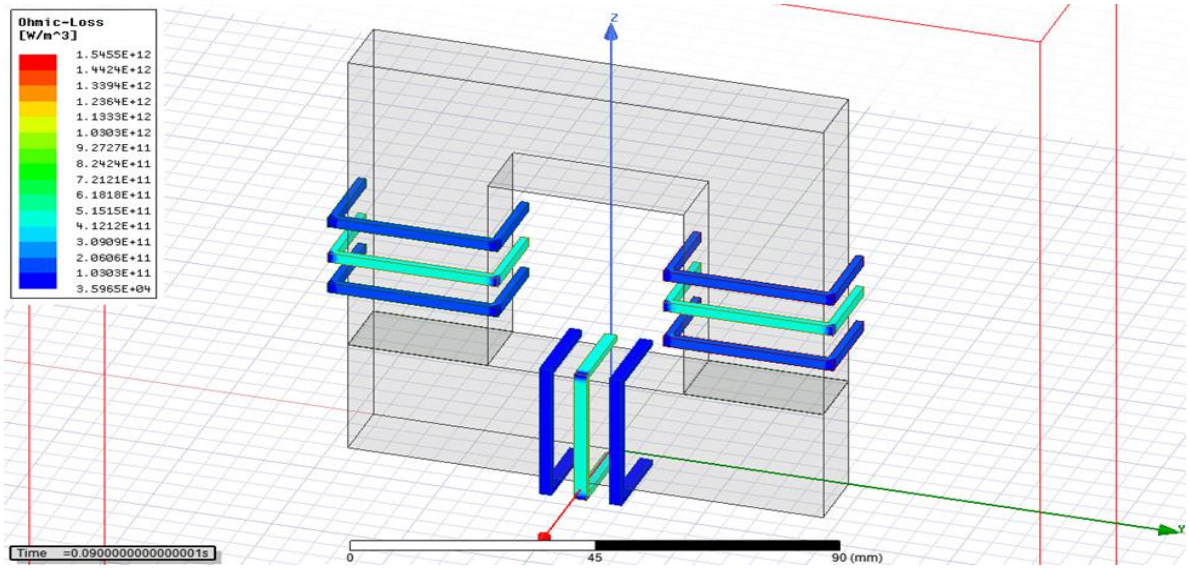

Figure 2.110. Ohmic loss for 13800 V.

Here four cases were observed in 3D FEA simulation in Ansys Maxwell platform. With Increasing voltage and induced current, magnetic field intensity (H), current density (J) and ohmic loss increases which was verified in this simulation.

Chapter 5: Conclusion and future work

Phase shift modulation was implemented to control power transfer in DABC and four-port DC-DC converter.

Ansys Maxwell based isolation transformer was built by updating core materials characteristics like B-H curve, B-Pv curve.

Flux density (B), current density (J), magnetic field intensity (H), core loss, winding loss was evaluated for different voltage level to investigate core and winding performance.

For future work some suggestion can be considered:

Transient-transient co-simulation between Ansys Maxwell and Simplorer can be done to observe flux density during transient and steady state in closed loop control.

Different set of high frequency could be tested to evaluate core loss for the whole operating region.

Several winding configurations need to be implemented to investigate winding loss.

Switching loss model in high frequency could also be established for accurate loss model of the converter.

References

[1] R. Petkov, "Optimum design of a high-power, high-frequency transformer," *IEEE Transactions on Power Electronics*, vol. 11, no. 1, pp. 33 - 42, 1996.

[2] M. A. Bahmani, T. Thiringer, A. Rabiei and T. Abdulahovic, "Comparative Study of a Multi-MW High-Power Density DC Transformer With an Optimized High-Frequency Magnetics in All-DC Offshore Wind Farm," *IEEE Transactions on Power Delivery*, vol. 31, no. 2, pp. 857 - 866, 2015.

[3] M. A. Bahmani, T. Thiringer and M. Kharezy, "Design Methodology and Optimization of a Medium-Frequency Transformer for High-Power DC–DC Applications," *IEEE Transactions on Industry Applications*, vol. 52, no. 5, pp. 4225 - 4233, 2016.

[4] G. Ortiz, J. Biela and J. W. Kolar, "Optimized design of medium frequency transformers with high isolation requirements," in *36th Annual Conference on IEEE Industrial Electronics Society-IECON 2010*, AZ, USA, Nov. 2010.

[5] P. Huang, C. Mao, D. Wang, L. Wang, Y. Duan, J. Qiu, G. Xu and H. Cai, "Optimal Design and Implementation of High-Voltage High-Power Silicon Steel Core Medium-Frequency Transformer," *IEEE Transactions on Industrial Electronics*, vol. 64, no. 6, pp. 4391 - 4401, 2017.

[6] D. S. Segaran, "Dynamic Modelling and Control of Dual Active Bridge Bi-directional DC-DC Converters for Smart Grid Applications," Ph.D Dissertation, Royal Melbourne Institute of Technology University, 2006.

[7] F. Krismer, "Modeling and Optimization of Bidirectional Dual Active Bridge DC–DC Converter Topologies," Ph.D. dissertation, ETH ZURICH, 2010.

[8] T. Zhao, G. Wang, S. Bhattacharya and A. Q. Huang, "Voltage and Power Balance Control for a Cascaded H-Bridge Converter-Based Solid-State Transformer," *IEEE Transactions on Power Electronics,* vol. 28, no. 4, pp. 1523 - 1532, 2013.

[9] P. Krause, O. Wasynczuk, S. Sudhoff and S. Pekarek, Analysis of Electric Machine and Drive Systems, Wiley-IEEE Press, 2013.

[10] J. Fu, "Multiport high frequency transformer coupled bidirectional DC-DC converter for hybrid renewable energy system," Ph.D Dissertation, Tennessee Technological University, 2012.

[11] S. Falcones, R. Ayyanar and X. Mao, "A DC–DC Multiport-Converter-Based Solid-State Transformer Integrating Distributed Generation and Storage," *IEEE Transactions on Power Electronics,* vol. 28, no. 5, pp. 2192 - 2203, 2013.

[12] R. W. Erickson and D. Maksimovic, Fundamentals of Power Electronics, Springer US, 2001.

[13] H. Chen and D. Divan, "High-frequency transformer design for the soft-switching solid state transformer (S4T)," in *2017 IEEE Applied Power Electronics Conference and Exposition (APEC)*, Tampa, USA, 2017.

[14] Y. Du, S. Baek, S. Bhattacharya and A. Q. Huang, "High-voltage high-frequency transformer design for a 7.2kV to 120V/240V 20kVA solid state transformer," in *36th Annual Conference on IEEE Industrial Electronics Society (IECON)*, Arizona, USA, 2010.

[15] W. Shen, "Design of High-density Transformers for High-frequency High-power Converters," Ph.D. Dissertation, Virginia Polytechnic Institute and, Blacksburg, Virginia. USA, 2006.

[16] D. Jiles, J. Thoelke and M. Devine, "Numerical determination of hysteresis parameters for the modeling of magnetic properties using the theory of ferromagnetic hysteresis," *IEEE Transactions on Magnetics*, vol. 28, no. 1, pp. 27 - 35, 1992.

[17] D. C. Jiles and D. L. Atherton, "Theory of ferromagnetic hysteresis," *Journal of Applied Physics*, vol. 55, no. 6, pp. 2115-2120, 1984.

[18] D. Lederer, H. Igarashi, A. Kost and T. Honma, "On the parameter identification and application of the Jiles-Atherton hysteresis model for numerical modelling of measured characteristics," *IEEE Transactions on Magnetics*, vol. 35, no. 3, pp. 1211 - 1214, 1999.

[19] W. A. Roshen, "A Practical, Accurate and Very General Core Loss Model for Nonsinusoidal Waveforms," *IEEE Transactions on Power Electronics*, vol. 22, no. 1, pp. 30 - 40, 2007.

[20] Y. Sakaki and T. Matsuoka, "Hysteresis losses in Mn-Zn ferrite cores," *IEEE Transactions on Magnetics,* vol. 22, no. 5, pp. 623 - 625, 1986.

[21] G. Bertotti, "General properties of power losses in soft ferromagnetic materials," *IEEE Transactions on Magnetics,* vol. 24, no. 1, pp. 621 - 630, 1988.

[22] C. Steinmetz, "On the law of hysteresis," *Proceedings of the IEEE ,* vol. 72, no. 2, pp. 197 - 221, 1984.

[23] J. Brittain, "A steinmetz contribution to the AC power revolution," *Proceedings of the IEEE,* vol. 72, no. 2, pp. 196 - 197, 1984.

[24] J. Reinert, A. Brockmeyer and R. D. Doncker, "Calculation of losses in ferro- and ferrimagnetic materials based on the modified Steinmetz equation," *IEEE Transactions on Industry Applications,* vol. 37, no. 4, pp. 1055 - 1061, 2001.

[25] J. Li, T. Abdallah and C. Sullivan, "Improved calculation of core loss with nonsinusoidal waveforms," in *Thirty-Sixth IAS Annual Meeting. Conference Record of the IEEE Industry Applications Conference (2001)*, Chicago, IL, USA, 2001.

[26] K. Venkatachalam, C. Sullivan, T. Abdallah and H. Tacca, "Accurate prediction of ferrite core loss with nonsinusoidal waveforms using only Steinmetz parameters," in *2002. Proceedings. 2002 IEEE Workshop on Computers in Power Electronics*, Puerto Rico, USA, 2002.

[27] J. Muhlethaler, J. Biela, J. W. Kolar and A. Ecklebe, "Improved Core-Loss Calculation for Magnetic Components Employed in Power Electronic Systems," *IEEE Transactions on Power Electronics,* vol. 27, no. 2, pp. 964 - 973, 2012.

[28] M. Rashidi, A. Nasiri and R. Cuzner, "Application of multi-port solid state transformers for microgrid-based distribution systems," in *IEEE International Conference on Renewable Energy Research and Applications (ICRERA),* Birmingham, UK, Nov. 2016.

[29] M. Rashidi, A. Bani-Ahmed, R. Nasiri, A. Mazaheri and A. Nasiri, "Design and implementation of a multi winding high frequency transformer for MPSST application," in *IEEE 6th International Conference on Renewable Energy Research and Applications (ICRERA),* San Diego, CA, USA, Nov. 2017.